



Contents lists available at ScienceDirect

# Progress in Materials Science

journal homepage: [www.elsevier.com/locate/pmatsci](http://www.elsevier.com/locate/pmatsci)



## Atomic-level structure and structure–property relationship in metallic glasses

Y.Q. Cheng, E. Ma \*

Department of Materials Science and Engineering, Johns Hopkins University, Baltimore, MD 21218, USA

### ARTICLE INFO

*Article history:*

Received 1 June 2010

Received in revised form 11 December 2010

Accepted 11 December 2010

Available online 14 December 2010

### ABSTRACT

The structure of metallic glasses (MGs) has been a long-standing mystery. On the one hand, MGs are amorphous materials with no long-range structural order; on the other hand, topological and chemical short-to-medium range order is expected to be pronounced in these alloys, due to their high atomic packing density and the varying chemical affinity between the constituent elements. The unique internal structure of MGs underlies their interesting properties, which render MGs potentially useful for various applications. While more and more glass-forming alloys have been developed in recent years, fundamental knowledge on the structural aspect of MGs remains seriously lacking. For example, how atoms pack on the short-to-medium range, how the structure differs in different MGs and changes with composition, temperature, and processing history, and more importantly, how the structure influences the properties of MGs, are still unresolved questions. In this paper, we review the tremendous efforts over the past 50 years devoted to unraveling the atomic-level structure of MGs and the structural origin of their unique behaviors. Emphasis will be placed on the progress made in recent years, including advances in structural characterization and analysis of prototypical MGs, general structural models and fundamental principles, and the correlations of thermodynamic, kinetic, and mechanical properties with the MG structures. Some widely observed property–property correlations in MGs are also examined from the structural perspective. The insights summarized are shown to shed light on many intriguing behaviors of the MG-forming alloys and expected to

\* Corresponding author. Tel.: +1 410 516 8601.

E-mail addresses: [cheng@jhu.edu](mailto:cheng@jhu.edu) (Y.Q. Cheng), [ema@jhu.edu](mailto:ema@jhu.edu) (E. Ma).

impact the development of MGs. Outstanding questions in this important research area will also be outlined.

© 2010 Elsevier Ltd. All rights reserved.

## Contents

1. Introduction . . . . .	381
1.1. Metallic glass: formation and classification. . . . .	382
1.2. Properties of metallic glasses . . . . .	383
1.2.1. Thermodynamic and kinetic properties . . . . .	383
1.2.2. Mechanical properties . . . . .	385
1.3. Outline of this review . . . . .	388
2. Structural characterization of metallic glasses. . . . .	389
2.1. Structure parameters for metallic glasses . . . . .	389
2.1.1. Pair distribution function. . . . .	389
2.1.2. Structure factor. . . . .	389
2.1.3. Coordination number . . . . .	390
2.1.4. Chemical short-range order . . . . .	390
2.1.5. Bond angle distribution . . . . .	391
2.1.6. Bond orientational order . . . . .	391
2.1.7. Common neighbor analysis . . . . .	392
2.1.8. Voronoi tessellation . . . . .	393
2.2. Experimental techniques . . . . .	393
2.2.1. X-ray/neutron diffraction . . . . .	393
2.2.2. X-ray absorption fine structure . . . . .	394
2.2.3. Fluctuation electron microscopy . . . . .	395
2.2.4. Transmission electron microscopy . . . . .	396
2.2.5. Nuclear magnetic resonance . . . . .	397
2.3. Computational methods . . . . .	397
2.3.1. Reverse Monte Carlo modeling . . . . .	397
2.3.2. Molecular dynamics simulation. . . . .	398
2.3.3. Quantum molecular dynamics. . . . .	398
2.3.4. Classical molecular dynamics . . . . .	399
3. Atomic-level structure of metallic glasses . . . . .	400
3.1. Structure of monatomic liquids . . . . .	400
3.1.1. Dense random packing of hard spheres . . . . .	400
3.1.2. Packing of soft spheres with pair potentials. . . . .	403
3.1.3. Supercooled pure metallic liquids . . . . .	404
3.2. Structure of LTM–NM metallic glasses. . . . .	404
3.2.1. Model based on dense random packing of hard spheres . . . . .	404
3.2.2. Stereochemical model . . . . .	405
3.2.3. Efficient packing of quasi-equivalent NM-centered clusters . . . . .	405
3.2.4. Multicomponent LTM–NM metallic glasses and chemical heterogeneity. . . . .	406
3.3. Structure of SM–RE metallic glasses . . . . .	408
3.3.1. Structure of Al-rich metallic glasses . . . . .	409
3.3.2. Origin of the prepeak . . . . .	410
3.3.3. Comparison with LTM–NM metallic glasses . . . . .	411
3.3.4. Structure of RE-rich metallic glasses and polyamorphism. . . . .	412
3.4. Structure of ETM–LTM metallic glasses . . . . .	413
3.4.1. Structure of Cu–Zr binary metallic glasses . . . . .	413
3.4.2. Structure of Cu–Zr–Al metallic glasses . . . . .	417
3.4.3. Structure of Cu–Zr–Ag metallic glasses . . . . .	418
3.4.4. Structure of (Ti,Zr,Nb,Hf,Ta)–(Ni,Cu,Pd,Ag)–(Al)–(Be) metallic glasses . . . . .	419
3.5. Structure of AM–LTM metallic glasses . . . . .	420
3.6. Icosahedral order: metallic glasses and quasicrystals . . . . .	421
3.7. General structural models for metallic glasses . . . . .	422

3.7.1.	Polytetrahedral packing model and the role of disclinations.....	423
3.7.2.	Efficient packing of solute-centered clusters .....	429
3.7.3.	Summary and comparison of the structural models .....	431
3.7.4.	MRO: a fractal packing proposition.....	433
4.	Structure–property relationship in metallic glasses.....	435
4.1.	Correlation between glass structure and thermodynamic/kinetic properties .....	436
4.1.1.	Potential energy surface description .....	436
4.1.2.	Role of icosahedra in the dynamical slowdown .....	437
4.1.3.	Non-icosahedral metallic glasses.....	442
4.1.4.	Physical basis for the classification of metallic glasses .....	443
4.2.	Correlation between structure and mechanical properties.....	444
4.2.1.	Structural fluctuation and mechanical heterogeneity .....	445
4.2.2.	Shear modulus and elasticity: percolation of rigidity .....	447
4.2.3.	Yielding: percolation of shear transformation zones .....	447
4.2.4.	Strain localization and intrinsic plasticity: degree of mechanical heterogeneity .....	449
4.2.5.	Effects of processing history: the structural differences .....	451
4.2.6.	Effects of chemical bonding: metallic versus covalent-like.....	453
4.3.	Indicators of structural state .....	453
4.3.1.	Free volume .....	453
4.3.2.	Atomic-level stresses .....	454
4.3.3.	Configurational potential energy.....	455
4.3.4.	Effective disorder temperature .....	455
4.3.5.	Interrelations and differences .....	455
5.	Structural perspective of the property–property correlations.....	456
5.1.	Thermodynamics/kinetics-GFA correlation .....	456
5.2.	T <sub>g</sub> –strength correlation .....	457
5.3.	Poisson's ratio-plasticity correlation .....	458
6.	Summary and outlook .....	460
	Acknowledgements .....	462
	References .....	462

---

## 1. Introduction

Both metals and glasses have been known to mankind for a long time. As early as 3000 BC, people were already making tools and weapons with bronze, an alloy composed primarily of copper. Even earlier in the Stone Age, a naturally forming glass based on silica (obsidian) was discovered and used as axes and knives. Over the thousands of years since then, these two categories of materials have been recognized to possess distinctly different properties, and explored and developed more or less independently. Metals are made of metallic elements via metallic bonding. Atoms in metals are known to reside on a crystalline lattice with long-range translational order. Glasses, in contrast, often involve covalent and ionic bonds, or van der Waals interactions, and are characterized by an amorphous structure without long-range structural correlation. The different atomic and electronic structures underlie the contrasting properties of metals and glasses. It is not until the 1960s that metallic glasses (MGs) [1] were successfully synthesized, overlapping these two categories of materials. MGs consist of predominantly metallic elements and metallic bonds, but at the same time have an amorphous internal structure. Such a combination of “metal” and “glass” leads to unique properties and unprecedented opportunities. Since the discovery of the first MG (Au<sub>75</sub>Si<sub>25</sub>) [1], there has been increasing interest in developing and understanding this new family of materials [2–12]. Among the many unresolved puzzles, the atomic-level structure and structure–property relationship are one of the central topics. In this review, we will focus on the structural aspect of MGs, as well as the structural basis for their physical and mechanical properties. Progress made in this area over the past 50 years will be summarized and discussed, and several challenging subjects will be proposed for future research.

### 1.1. Metallic glass: formation and classification

Glasses are essentially “frozen” liquids made by quenching of their high temperature melts. Since liquids tend to crystallize when temperature ( $T$ ) is below the melting temperature ( $T_m$ ) or liquidus temperature ( $T_l$ ), to retain the amorphous structure one needs to reduce the temperature sufficiently fast such that the liquid is frozen (by undergoing a glass transition at the glass transition temperature,  $T_g$ ) before the crystals have the time to nucleate and grow. Compared to the commonly known glass formers such as silicate or organic materials, metals easily crystallize upon solidification, rendering the formation of MGs rather difficult. This is why the first MG sample ( $\sim 10 \mu\text{m}$  in thickness) was only obtained at very high cooling rates ( $10^5$ – $10^6 \text{ K/s}$ ). By carefully selecting constituent elements and adjusting the composition, however, it is possible to develop alloys with much better glass forming ability (GFA), such that MGs can be obtained in larger size using slower cooling rates, and made more stable at room temperature. To achieve this, the key is to stabilize the metallic liquids in the temperature range between  $T_l$  and  $T_g$  (i.e., the supercooled regime) and to delay the crystallization into the intermetallic phases that are in competition with the supercooled liquids.

Over the past five decades, many MG-forming alloys have been discovered, involving virtually all metallic elements in the periodic table [13]. These MGs can be classified in different ways. For example, according to which metal is the dominant component of the alloy, MGs can be labeled as Zr-based, Al-based, Fe-based, etc. To emphasize the nature of the constituent elements, the MGs can be characterized as metal–metal type or metal–metalloid type. The various MG-forming alloys also have different GFA, and those good glass formers which can be cast into a fully glassy sample at least 1 mm in its thinnest dimension are conventionally called bulk metallic glasses (BMGs). A more sophisticated classification of BMGs has been proposed by Inoue [6] and further developed by Takeuchi and Inoue [14]. In the current review, we will employ a modified and simplified version of their classification. First of all, the typical constituent elements of the BMGs can be grouped as: alkali and alkaline earth metals (AM), semi- or simple metals (SM) in IIIA and IVA groups neighboring the semiconductors, transition metals (TM), including early transition metals (ETM) and late transition metals (LTM), rare earth metals (RE), and nonmetals (NM), see Table 1 for details. It appears that almost all MGs to date contain elements from at least two different groups, and there are certain prototype combination pairs upon which many closely related but more complex BMGs are based. We thus classify the commonly seen MGs according to these characteristic binary prototypes, see Table 2. Following this classification, the search for BMG formers is very much like cooking: one would first select a binary prototype (main ingredients), then add alloying elements (seasoning) and fine tune the composition (flavor) to enhance

**Table 1**  
Classification of common constituent elements of MGs.

Abbreviation	Description	Examples
AM	Metals in groups IA and IIA	Mg, Ca, (Be <sup>a</sup> )
SM	Metals in groups IIIA and IVA	Al, Ga
TM	ETM	Ti, Zr, Hf, Nb, Ta, Cr, Mo, Mn
	LTM	Fe, Co, Ni, Cu, Pd, Pt, Ag, Au, Zn
RE	Sc, Y, Lanthanides (Ln)	Sc, Y, La, Ce, Nd, Gd
NM	Nonmetals and metalloids	B, C, P, Si, Ge

<sup>a</sup> Although element Be is an AM per this classification, its role in MG formation is often unique. See discussion in Section 3.4.4.

**Table 2**  
Classification of typical MGs based on the binary prototypes.

Prototype	Base metal	Examples
LTM + NM	LTM	Ni–P, Pd–Si, Au–Si–Ge, Pd–Ni–Cu–P, Fe–Cr–Mo–P–C–B
ETM + LTM	ETM or LTM	Zr–Cu, Zr–Ni, Ti–Ni, Zr–Cu–Ni–Al, Zr–Ti–Cu–Ni–Be
SM + RE	SM or RE	Al–La, Ce–Al, Al–La–Ni–Co, La–(Al/Ga)–Cu–Ni
AM + LTM	AM	Mg–Cu, Ca–Mg–Zn, Ca–Mg–Cu

the GFA. A well-known recipe is Inoue's three empirical rules for BMG formation [6,15]: multicomponent system with more than three elements, atomic size mismatch above 12%, and negative heat of mixing between the components. The underlying mechanism of these rules, as noted by Inoue [6], may be related to the atomic-level structure, including local topological and chemical ordering, as well as the electronic structure and the nature of bonding. These structural features will be discussed in this review.

## 1.2. Properties of metallic glasses

The atomic configuration and chemical bonding together determine the intrinsic properties of materials. In this sense, the MGs connect the “amorphous” structure with “metallic” bonding; they are thus expected to possess unique properties that do not exist in other materials. Typical behaviors of MGs will be briefly introduced in this section, including the thermodynamic, kinetic, and mechanical properties (other properties will not be covered in this review, due to space limitations). It will become obvious that to explain/understand the intriguing properties of MGs, the underlying structural origins need to be unraveled. This introduction thus sets the stage for the detailed correlations with structures that will be presented in Sections 4 and 5.

### 1.2.1. Thermodynamic and kinetic properties

The thermodynamics and kinetics of supercooled liquids hold the key to understanding the GFA [16–22]. When the temperature is reduced to below  $T_l$ , the free energy of the supercooled liquid is higher than that of the competing crystal(s), and the difference,  $\Delta G$ , is the driving force towards crystallization. The driving force increases with supercooling (see Fig. 1 [22]), as the liquid increasingly deviates from thermodynamic equilibrium.

The kinetic properties can be studied by monitoring the viscosity ( $\eta$ ) and its evolution with temperature. The viscosity increases exponentially with decreasing temperature:  $\eta = \eta_0 \exp(W/kT)$ , where  $\eta_0$  is the high temperature limit of  $\eta$ ,  $k$  is the Boltzmann constant, and  $W$  is an effective activation energy characterizing the barrier against viscous flow. If  $W$  is a constant independent of temperature, as defined in the original Arrhenius equation,  $\log(\eta)$  and  $\log(1/T)$  should scale with each other linearly, leading to the Arrhenius behavior [19]. However, the linear scaling relation does not hold for

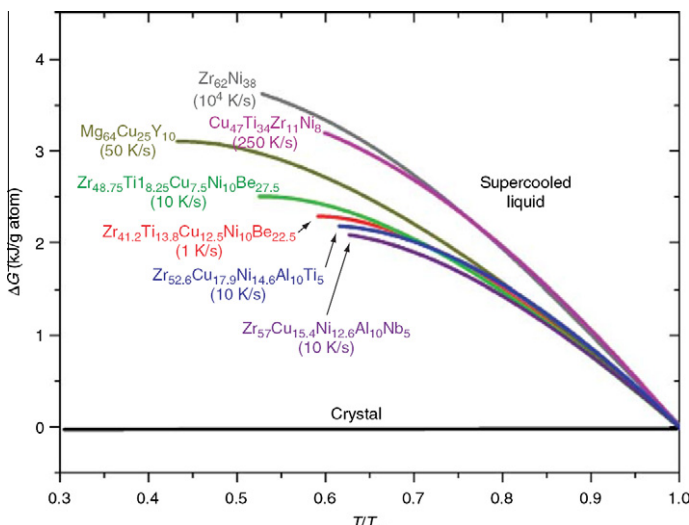


**Fig. 1.** Increase of  $\Delta G$  with supercooling in various BMGs having different GFA (critical cooling rate). (Reproduced from [22] with permission © 2007 by Materials Research Society.)

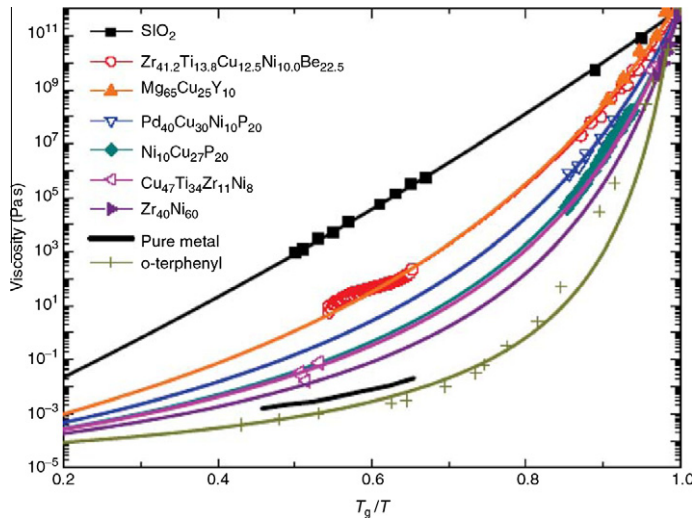


**Fig. 2.** Evolution of viscosity with temperature in various glasses. (Reproduced from [22] with permission © 2007 by Materials Research Society.)

MG-forming liquids, as shown in Fig. 2 [22] for several examples (the temperature scale is normalized against  $T_g$ , following Angell [17]). With supercooling, the viscosity increases dramatically, deviating from the linear extrapolation of the high temperature trend. The glass transition is often mapped to the temperature at which the viscosity reaches a critical value (e.g.,  $10^{12}$  Pa s), and the slope around glass transition in Angell's plot is defined as fragility [23],  $m = \left[ \frac{d\eta(T_g/T)}{dT_g/T} \right]_{T=T_g}$ . Liquids with lower fragility are termed “stronger”, whereas those with higher fragility are more “fragile”. The non-Arrhenius increase of viscosity in the supercooled regime cannot be explained by constant  $W$  and simple temperature effects. Instead, it suggests that the intrinsic material state (e.g., the inherent structure) must also evolve with supercooling.

According to Adam and Gibbs [24], the thermodynamics and kinetics are connected via  $\eta = A \exp \left[ \frac{B}{S_c(T)} \right]$ , where  $\eta$  also scales with the characteristic relaxation time of the quasi-equilibrium supercooled liquid. Here the supercooled liquid is described as “quasi-equilibrium” because thermodynamically it is not truly in equilibrium, but the liquid may appear to be in equilibrium within certain time-scale due to the nucleation barrier for crystallization and the slow kinetics at relatively low temperatures.  $A$  and  $B$  in the equation are temperature-independent constants, and  $S_c(T)$  is the temperature-dependent configurational entropy of the liquid.  $S_c(T)$  measures the number of available configurations of the system, which determines the minimum possible cluster size and energy barrier for relaxation. It is closely related to the degree of structural order in the liquid, and thus implies a structural origin underlying the thermodynamic and kinetic properties. Since  $(\frac{\partial S_c}{\partial T})_p = \frac{\Delta c_p}{T}$ ,  $S_c(T)$  can be examined by measuring the excess specific heat  $\Delta c_p$  in experiments, where  $\Delta c_p$  is the difference in constant-pressure specific heat between the quasi-equilibrium supercooled liquid and the frozen glass, and thus corresponds to the *configurational* entropy only. Experimentally, the measured  $\Delta c_p$  may have different temperature-dependence for different materials, and an example for a Zr-based MG is shown in Fig. 3 [25]. This example shows an increase of  $\Delta c_p$  when entering the supercooled regime, which suggests that the configurational entropy is being extracted from the liquid at a faster rate. This observation may be further connected with the structural ordering process; that is, how and how fast the atoms are ordered to reduce the configurational entropy is the key to understanding the non-Arrhenius viscosity rise, as will be illustrated later in this review.

As mentioned previously, when the temperature is reduced, the crystallization rate of a supercooled liquid is determined by both the increasing driving force (free energy) and increasing resistance to relaxation (viscosity). The two have opposite effects and their competition leads to the typical

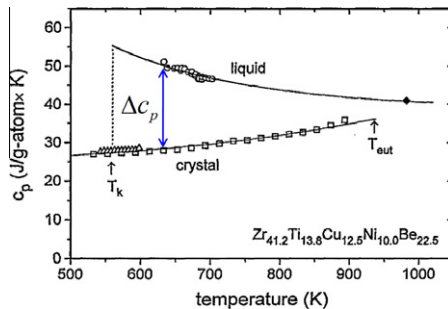


**Fig. 3.** Measured specific heat of Zr<sub>41.2</sub>Ti<sub>13.8</sub>Cu<sub>12.5</sub>Ni<sub>10.0</sub>Be<sub>22.5</sub> in the state of supercooled liquid (○◆), MG (△), and crystal (□). (Adapted from [25] with permission © 1995 by American Institute of Physics.)

time–temperature–transformation (TTT) diagram, Fig. 4, in which the boundary separating the amorphous and crystallized states takes a nose-like shape. For good GFA, the nose should be pushed to the right side (i.e., longer time-scale). A narrow supercooled region (or a high reduced glass transition temperature,  $T_{rg} = T_g/T_i$ ) would also facilitate glass formation [26].

Due to the non-equilibrium nature of the MGs, annealing or aging would result in structural relaxation. The cooling rate also determines how well the glass is relaxed and what configuration (i.e., at what characteristic temperature and viscosity) of the supercooled liquid is finally retained. Therefore, the structure and properties of MGs can be very sensitive to the processing history, and when comparing two MGs, how they were prepared/processed is an essential factor that needs to be taken into consideration.

The thermodynamic and kinetic processes discussed in this section are closely related to the amorphous structure and its evolution. For example, during supercooling, the decreasing configurational enthalpy and entropy, and the non-Arrhenius rise of viscosity and relaxation time, are both associated with internal structural changes in the metallic liquids. The annealing effects on MGs also have their origin in the structural relaxation. Such a correlation will be discussed in detail in Section 4.

### 1.2.2. Mechanical properties

MGs have intriguing mechanical properties and are promising structural materials [27–31]. The elastic moduli of MGs are in general comparable to the corresponding crystalline compounds [32–34]. The difference in the bulk modulus is often within a few percent, while the difference of shear modulus can be more significant, with the shear modulus of MG being typically 10–30% lower [35–37]. The similar bulk modulus can be explained by the similar bonding nature and average electron

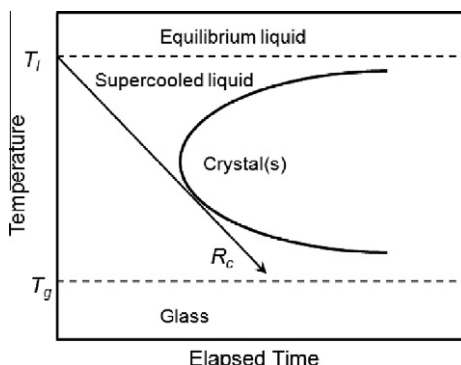


**Fig. 4.** A schematic TTT diagram illustrating glass formation. The slope  $R_c$  represents the critical cooling rate for glass formation.

density in MGs and crystals of the same composition [38], whereas the almost systematically lower shear modulus of the MGs originates from the shear softening due to structural disorder. Specifically, the intrinsic non-affine elastic field [39] and the local anelastic deformation (relaxation) [40] have been demonstrated to be the microscopic characteristics of MGs under macroscopic elastic shear, in both experiments [41–44] and computer simulations [45–52], and proposed to be responsible for their reduced shear modulus [36,39,45,46]. These behaviors arise from the amorphous nature of the structure and its inherent fluctuation, as well as the resulting mechanical heterogeneity [53]. The local relaxation is essentially inelastic rearrangement of atom clusters. They can happen at very small global strain, and are reversible upon unloading, leaving virtually no macroscopic plastic deformation. However, such anelastic behavior manifests itself by the internal friction [54–57] and the softened transverse phonons [58].

At room temperature, MGs yield via the formation of shear bands, and usually fail catastrophically with limited compressive plasticity and little or no tensile ductility. The strength and the elastic limit of MGs are much higher than conventional metals. For example, the yield strength of a Cu–Zr MG can be as high as 2 GPa with a uniaxial elastic strain limit of ~2%. It is interesting to note that this magnitude of the elastic strain limit measured in experiments for various MGs appears to be universal, as shown in Fig. 5 [59]. Another important aspect about the yield strength of MGs is its universal scaling with the  $T_g$ , as seen in Fig. 6 [60]. This correlation may have its origin in the yielding mechanism of MGs and its relationship with the glass transition, i.e., the equivalence of thermal activation and mechanical activation to cause flow in MGs [51,60–62] (see Section 4 for more discussions).

The mechanical properties of MGs are sensitively dependent on the composition, often more so than in the case of crystals, and cannot be explained by the simple rule of mixtures. For example, Fig. 7 [63] displays the stress–strain curves for Cu–Zr MGs at different compositions. The modulus, strength and plasticity all systematically change with composition. For MGs of a given composition, the mechanical properties are also affected by the processing history, such as the behavior of shear modulus in Fig. 8 [37], and toughness in Fig. 9 [64]. In addition, the sample size may also matter, especially at extremely small length-scales (e.g., sub-micrometer samples) [65–69]. The property trend and correlations shown in Figs. 5–9 will be re-visited in later sections, where connections with structural features will be established and discussed.

These mechanical behaviors of MGs originate from their unique deformation mechanism. In a crystalline alloy, it is known that the well-defined flow defects such as dislocations play a key role. Existing

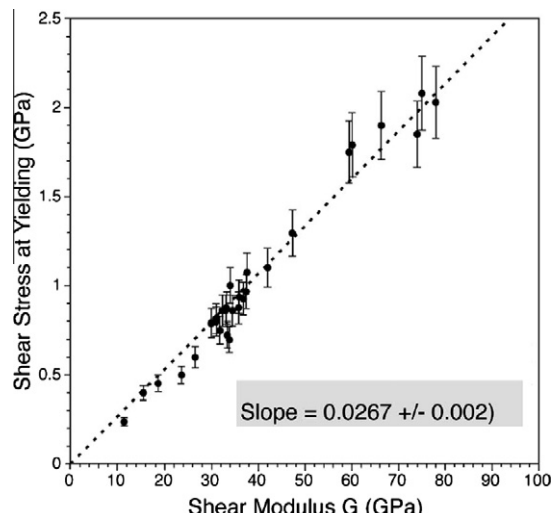


**Fig. 5.** Linear scaling between shear modulus and shear strength of various BMGs, suggesting universal yield strain. (Reproduced from [59] with permission © 2005 by American Physical Society.)

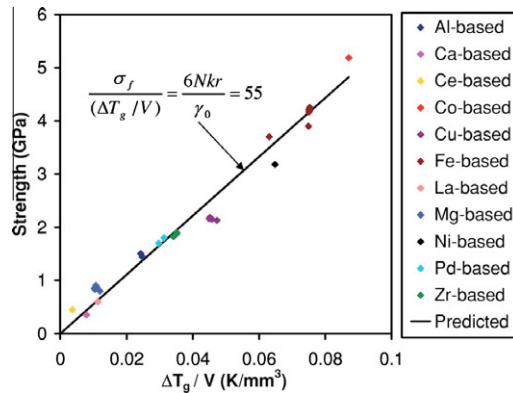


**Fig. 6.** Scaling relation between strength and  $T_g$  for various BMGs. (Reproduced from [60] with permission © 2006 by American Institute of Physics.)

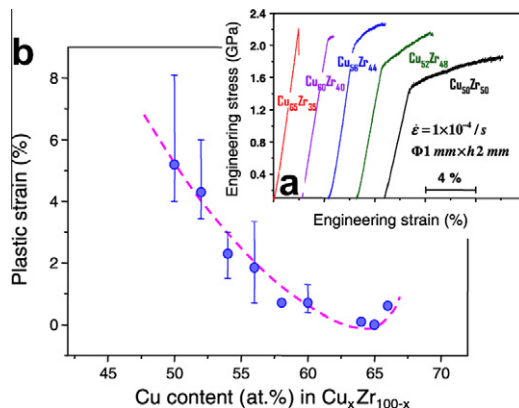


**Fig. 7.** Composition dependence of mechanical properties of Cu-Zr MGs. (Reproduced from [63] with permission © 2007 by Elsevier.)

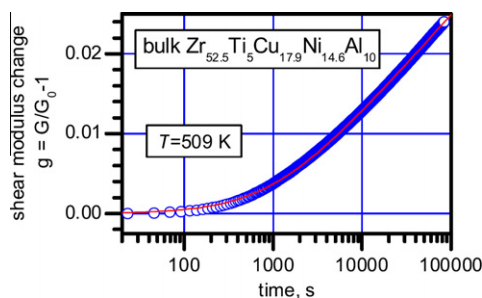


**Fig. 8.** Processing history (annealing time) dependence of shear modulus in a Zr-based BMG. (Reproduced from [37] with permission © 2008 by American Physical Society.)

dislocations are mobile and can be activated to migrate under external stress, initiating plastic deformation and yielding. Strain hardening, which leads to stable and uniform elongation and tensile

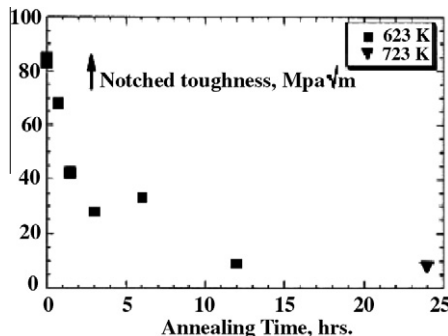


**Fig. 9.** Processing history (annealing temperature and time) dependence of notched toughness of  $Zr_{41.25}Ti_{13.75}Cu_{12.5}Ni_{10}Be_{22.5}$  (Vitreloy 1). (Reproduced from [64] with permission © 2005 by Taylor & Francis.)

ductility, is rendered possible by mechanisms such as dislocation multiplication and interactions. In MGs, however, the scenario is completely different. The carrier of plasticity is presumably the shear transformations proposed by Argon [70], localized in shear transformation zones (STZs), each involving a few hundred of atoms [71]. Different from dislocations in crystals, prior to loading STZs usually do not exist as obvious defects distinctly different from the matrix; they are simply local groups of atoms responding to the given level of applied load to produce shear strains. On average, the activation energy and activation volume of shear transformations are usually much larger than that for a mobile dislocation in crystals [59,71]. Moreover, a dislocation leaves a recovered lattice behind, while the STZ is often excited to a more energetic state (i.e., softened) upon shear transformation, via local volume dilatation together with topological transitions and/or chemical alienation [72]. As a result, the vicinity of an activated STZ is more prone to subsequent shear transformations, as directly shown by Schall et al. [73] in a deformation experiment on colloidal glasses. Finally, when a dislocation runs into a grain boundary or other dislocations, it encounters an elevated activation barrier; this mechanism is absent in MGs considering that the STZs are not mobile defects. Due to the above characteristics of STZ, although MGs need higher stress for yielding, once plastic deformation starts, it quickly localizes via linked STZs, in an autocatalytic manner resulting in a narrow shear band. This plastic instability in turn triggers catastrophic fracture. As such, the key to understand the strain localization and the instability is the work softening and the diminishing strain rate hardening of MGs at room temperature [74], and their micromechanisms rooted in the amorphous structure and its evolution with local deformation. Several constitutive models have been proposed and developed to describe the above deformation process of MGs, such as the model based on two-state STZs (by Falk and co-workers [75,76]), free volume (by Spaepen [77], Johnson and Lu [74], and others), fictive temperature (by Langer and co-workers [78,79]), cooperative shear (by Johnson and co-workers [80,81]), and finite element method analysis (e.g., by Anand and Su [82]). Although different assumptions and concepts have been used, one thing is indispensable for such models: a parameter indicating the structural state of the material, and a formula describing how it evolves with strain and depends on strain rate. This parameter serves as the link between structure and properties.

### 1.3. Outline of this review

The main body of this review focuses on two closely related topics: glass structure and structure–property relationship in MGs. The structural underpinnings of the many MG properties discussed above will be explored. We will begin with Section 2, in which the commonly used structural parameters, as well as experimental and computational techniques that are often employed (and recently improved) to characterize the MG structures, will be introduced. In Section 3, the history of, and recent progress on, solving the atomic-level structure of MGs will be reviewed, including not only the structural information about specific prototypes (categories) of MGs, but also general structure models and

theories. Section 4 examines the structure–property relationship in MGs, including correlations between thermodynamics, kinetics, and mechanical properties and the internal glass structures. In Section 5, several property–property correlations observed in MGs will be discussed, from the perspective of the common structural origin. Section 6 presents the summary and an outlook of future research directions in this area.

## 2. Structural characterization of metallic glasses

There are two major challenges in the study of MG structures: (1) how to construct a realistic three-dimensional (3-D) amorphous structure, using experimental and/or computational tools and (2) how to effectively characterize a given amorphous structure and extract the key structural features relevant to the fundamentals of glass formation and properties, using appropriate structural parameters. These two aspects will be addressed in this section. Unlike crystals, the glass structure has no definite form; each and every glass is literally different, in terms of the exact positions of the constituent atoms. Therefore, solving the exact structure of every MG is neither feasible nor necessary. The goal of the structural study of MGs should be to extract statistical information about the glass structure, to discover the key features of the short-to-medium range order, and to identify the underlying physical principles that constitute the structural basis of glass formation and glass properties.

### 2.1. Structure parameters for metallic glasses

One cannot identify MGs by assigning lattice parameters as we usually do for crystals. The following structural parameters are often used to describe and distinguish amorphous structures.

#### 2.1.1. Pair distribution function

Pair distribution function (PDF) is a pair correlation representing the probability of finding atoms as a function of distance  $r$  from an average center atom. The distribution of interatomic distances, the shell-like structure in the radial direction, and its fading out with increasing distance, can be clearly seen in the PDF of a liquid/glass. The  $\alpha - \beta$  partial PDF (i.e., the element-specific PDF) is defined as:

$$g_{\alpha\beta}(r) = \frac{N}{4\pi r^2 \rho N_\alpha N_\beta} \sum_{i=1}^{N_\alpha} \sum_{j=1}^{N_\beta} \delta(r - |\vec{r}_{ij}|) \quad (1)$$

where  $\rho$  is the number density of atoms in the system of  $N$  atoms,  $N_\alpha$  and  $N_\beta$  are the number of atoms of type  $\alpha$  and type  $\beta$ , respectively.  $|\vec{r}_{ij}|$  is the interatomic distance between two atom  $i$  (of type  $\alpha$ ) and atom  $j$  (of type  $\beta$ ). If the species are not differentiated, or in a monatomic system, we have [83]:

$$g(r) = \frac{1}{4\pi r^2 \rho N} \sum_{i=1}^N \sum_{j=1, j \neq i}^N \delta(r - |\vec{r}_{ij}|) \quad (2)$$

For amorphous materials, the short-to-medium range order is manifested by the peaks at small  $r$ . The structure information is embedded in the peak position, peak width, and relative intensity, etc. Conventionally, the atomic make-up and configuration of the nearest-neighbor shell, contributing to the first peak in the PDF, constitute the short-range order (SRO), whereas the structural features beyond the first peak to a distance up to 1–2 nm are called medium-range order (MRO). At larger  $r$ , the PDF gradually converges to unity, which means that no long-range order/correlation exists. The PDF for liquid Cu is given in Fig. 10a as an example. If the material is homogeneous and uniform, the partial PDFs would be very helpful in reconstructing the 3-D structure.

#### 2.1.2. Structure factor

The partial PDFs are directly related to partial structure factors in reciprocal space via Fourier transformation [83],

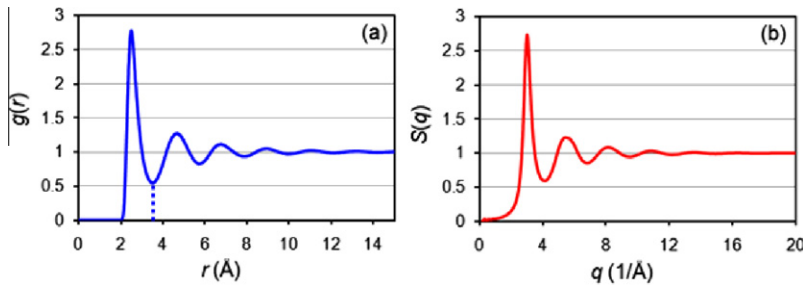


**Fig. 10.** (a) PDF and (b) structure factor of liquid Cu at 1500 K, obtained in computer (molecular dynamics) simulation.

$$S_{\alpha\beta}(q) - 1 = \frac{4\pi\rho}{q} \int_0^\infty r[g_{\alpha\beta}(r) - 1] \sin(qr) dr \quad (3)$$

where  $q$  is the variable in the reciprocal space, which corresponds to, in an X-ray scattering experiment, the magnitude of the diffraction vector ( $4\pi \sin \theta / \lambda$ ). The total structure factor is defined as the weighted summation of all partials:

$$S(q) = \sum_{\alpha} \sum_{\beta} \frac{c_{\alpha} c_{\beta} f_{\alpha} f_{\beta}}{\left(\sum_{\alpha} c_{\alpha} f_{\alpha}\right)^2} S_{\alpha\beta}(q) \quad (4)$$

where  $c_{\alpha}$  and  $c_{\beta}$  are the compositions (molar fractions) of the components, and  $f_{\alpha}$  and  $f_{\beta}$  are the atomic scattering factors. The structure factor of the Cu liquid is shown in Fig. 10b, corresponding to the PDF in Fig. 10a. With the total (and in some cases the partial) structure factor measured in an X-ray or neutron experiment, one can perform Fourier transformation to obtain the PDF in real space (see Section 2.2.1).

### 2.1.3. Coordination number

Coordination number (CN) is the number of atoms that are in the nearest-neighbor shell of a given center atom. For network glass with covalent bonding, a low CN value (e.g., CN = 4) is common (open environment), while for MGs with metallic bonding and dense packing, a high CN (e.g., CN = 12) is expected. For crystalline solids, the “nearest neighbors” are generally well-defined, whereas for amorphous materials, the determination of nearest neighbors is more or less arbitrary. There are several different ways to identify the nearest neighbors, such as the distance cutoff method and Voronoi tessellation method (see Section 2.1.7). For example, by setting a cutoff in the PDF (usually at the minimum after the first peak, dashed line in Fig. 10a), all atoms contributing to the first peak (up to the cutoff distance) are considered nearest neighbors. A specific cutoff can be assigned for each partial PDF to obtain the partial CN. The nearest neighbors contributing to the CN are often regarded as “bonded” with the center atom, while other atoms are not. A “bond” drawn between two atoms has clear physical meaning for covalent glasses, but not so for MGs, because metallic bonds are not localized in nature, and the bonding electrons are itinerant rather than shared by the atom pair only. The “bonds” drawn in some of the figures in this review, such as the straight lines connecting the atoms, are meant to label the nearest neighbors and only used for the convenience of visualization when analyzing the local motifs.

### 2.1.4. Chemical short-range order

For a structure with more than one species, it is useful to analyze the chemical make-up of the nearest-neighbor atoms, and compare with the composition of the alloy. This reflects how far the local chemistry deviates from the expectation of a random solution, i.e., the degree of chemical SRO. The

Warren–Cowley parameter [84,85] and the Cargill–Spaepen parameter [86] are often used to quantify the chemical SRO. Specifically, the Warren–Cowley parameter is defined as

$$\alpha_{AB} = 1 - \frac{Z_{AB}}{x_B Z_A} \quad (5)$$

where  $Z_{AB}$  is the partial CN ( $B$  atoms) around  $A$ ,  $Z_A$  is the total CN around  $A$ , and  $x_B$  is the nominal composition of  $B$ . A negative  $\alpha_{AB}$  means that unlike bonds are favored, whereas a positive  $\alpha_{AB}$  means like bonds are favored;  $\alpha_{AB} \sim 0$  indicates random solution. The Cargill–Spaepen parameter is similar, with the formula

$$\eta_{AB} = \frac{Z_{AB}}{Z_{AB}^*} - 1 \quad \text{and} \quad Z_{AB}^* = x_B Z_A Z_B / Z \quad (6)$$

where  $Z$  is the average CN of all atoms ( $Z = x_A Z_A + x_B Z_B$ ). The parameter can be normalized against the maximum possible value  $\eta_{AB}^{\max}$ , i.e.,

$$\eta_{AB}^0 = \eta_{AB} / \eta_{AB}^{\max} \quad (7)$$

The normalized  $\eta_{AB}^0$  is between 0 and 1.  $\eta_{AB}^0 = 0$  means complete chemical disorder or random solution, while  $\eta_{AB}^0 = 1$  means  $A$  atoms are bonded with  $B$  only.

### 2.1.5. Bond angle distribution

Bond angle distribution is a three-body correlation describing the spatial relations of three neighboring atoms. One first determines the nearest-neighbor atoms that are “bonded” with the center atom. Then the angles between each and every two bonds are calculated. The same is repeated for all atoms in the system to obtain the distribution. Specifically, for atom  $i$  with  $N_i$  nearest neighbors, neighbor  $j$  has bond length of  $r_{ij}$  with atom  $i$ , and neighbor  $k$  has bond length of  $r_{ik}$  with atom  $i$ . The distance between  $j$  and  $k$  is  $r_{jk}$ . Therefore, the bond angle formed between  $r_{ij}$  and  $r_{ik}$  is:

$$\theta_{ijk} = \cos^{-1} \left( \frac{r_{ij}^2 + r_{ik}^2 - r_{jk}^2}{2r_{ij}r_{ik}} \right) \quad (8)$$

and the bond angle distribution is:

$$g(\theta) = \frac{1}{\sum_{i=1}^N N_i(N_i - 1)} \sum_{i=1}^N \sum_{j=1}^{N_i} \sum_{k=j+1}^{N_i} \delta(\theta - \theta_{ijk}) \quad (9)$$

Such a distribution shows, statistically, the spatial arrangement of bonded atoms in the nearest-neighbor shell. For example, the characteristic bond angle is 109° in a diamond structure, and 90° in a simple cubic structure. In an amorphous material, there would be a distribution spectrum of bond angles.

### 2.1.6. Bond orientational order

The bond orientational order was analyzed by Steinhardt et al. [87,88] employing spherical harmonics. Different from the bond angle distribution, which is a three-body correlation, the bond orientational order is a many-body correlation. It is a quantitative description of the bond orientational symmetry around the center atom, which concerns multiple bond angles and their spatial relationship. To solve the bond orientational order, one first finds a center atom and its neighbors, as well as a reference coordination system with the origin at the center atom. For each bond connecting the center and a neighbor, the midpoint is located at  $\vec{r}$ . Following Steinhardt et al. [88], a set of numbers can then be associated with this bond

$$Q_{lm}(\vec{r}) \equiv Y_{lm}(\theta(\vec{r}), \phi(\vec{r})) \quad (10)$$

where  $\{Y_{lm}(\theta(\vec{r}), \phi(\vec{r}))\}$  are spherical harmonics, and  $\theta(\vec{r})$  and  $\phi(\vec{r})$  are the polar angles of the bond. We can then take the average over a suitable set of bonds, such as all nearest neighbors, to evaluate the bond orientational order in this set, i.e.,

$$\bar{Q}_{lm} \equiv \langle Q_{lm}(\vec{r}) \rangle \quad \text{and} \quad W_l \equiv \sum_{\substack{m_1, m_2, m_3 \\ m_1 + m_2 + m_3 = 0}} \begin{bmatrix} l & l & l \\ m_1 & m_2 & m_3 \end{bmatrix} \bar{Q}_{lm_1} \bar{Q}_{lm_2} \bar{Q}_{lm_3} \quad (11)$$

$$\widehat{W}_l \equiv W_l \left/ \left[ \sum_{m=-l}^l |\bar{Q}_{lm}|^2 \right]^{3/2} \right. \quad (12)$$

where  $\begin{bmatrix} l & l & l \\ m_1 & m_2 & m_3 \end{bmatrix}$  is the Wigner 3j symbol. The normalized parameter  $\widehat{W}_l$  evaluates the bond orientational order, and differentiates the various local environments [88]. For example, consider the 12 nearest neighbors around a center atom. An fcc-like packing would correspond to a non-zero  $\widehat{W}_4$  (larger value means more regular fcc order), while icosahedral packing would correspond to non-zero  $\widehat{W}_6$  and  $\widehat{W}_{10}$ . Similarly, one can also distinguish hcp, bcc, simple cubic, and many other order types using a subset of  $\widehat{W}_l$  [87,88].

### 2.1.7. Common neighbor analysis

Common neighbor analysis (CNA) proposed by Clarke and Jónsson [89] is a multi-body correlation between neighboring atoms. In CNA, each pair of nearest-neighbor atoms is given in a three-number index,  $ijkl$ .  $j$  is the number of nearest neighbors common to both atoms in the pair.  $k$  is the number of bonds between the  $j$  atoms themselves.  $l$  is the number of bonds in the longest continuous chain formed by the  $k$  bonds. CNA can effectively detect various local atomic arrangements. For example, a CNA index of 555 corresponds to a pentagonal bipyramid, which is the building block of an icosahedron, while 421 and 422 are the characteristics of fcc and hcp structures, respectively. A schematic showing how CNA works is depicted in Fig. 11. It is worth noting that the prevalence of 555 bonds alone, while demonstrating the preference for fivefold local environment, does not necessarily mean icosahedral order. For example, the cluster in Fig. 11c has six (out of nine) pairs with 555 index, but it has a CN = 9 and is certainly not an icosahedron (CN of icosahedra is 12).

A similar index with four integers  $ijkl$  was employed by Honeycutt and Andersen (H-A) [90]. The first number  $i$  in the H-A index is used to identify the bonding of two given atoms ( $i = 1$  for bonded pairs and  $i = 2$  for non-bonding atoms);  $j$  is the number of nearest neighbors shared in common by the two atoms; and  $k$  is the number of bonds among the shared neighbors. The fourth digit  $l$  is needed in case the first three numbers are the same but the bond geometries are different.

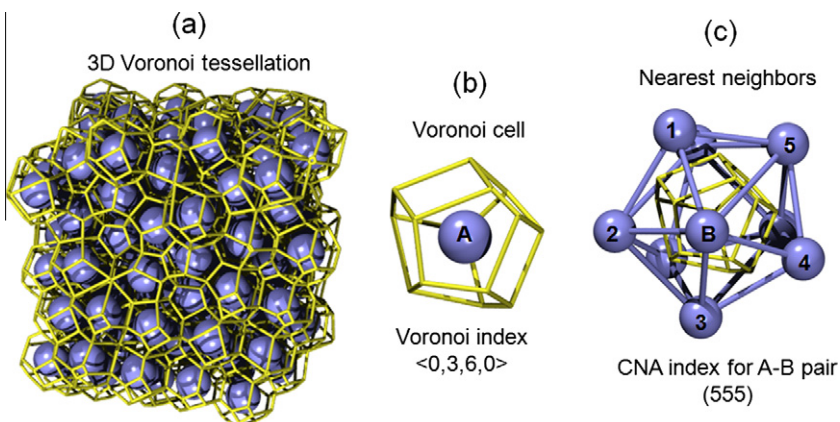


**Fig. 11.** (a) Voronoi tessellation, (b) Voronoi cell of center atom A, and (c) the nearest neighbors of A. The 3-D configuration of an amorphous structure can be represented by space tiling of Voronoi cells, while the motif of each cell (of the center atom) is determined by the spatial arrangement of the nearest neighbors. The example Voronoi cell in (b) has three quadrangular faces and five pentagonal faces, and thus has a Voronoi index of (0,3,6,0). The A-B pair forms a fivefold bond, and the example in (c) has five common neighbors (1–5) forming a loop, with a CNA index of 555.

The CNA and H-A indices are essentially the same, and when only nearest neighbors are considered, the CNA index provides extra information regarding the connectivity of the bonds among common neighbors.

### 2.1.8. Voronoi tessellation

The Voronoi tessellation [91] is a scheme to divide the 3-D space into cells centered by each atom. A plane is drawn to bisect each line connecting the center atom and one of the neighboring atoms, and the cell enclosed by all the inner planes is called a Voronoi cell, or Dirichlet cell, or Wigner–Seitz primitive cell, see Fig. 11 for an example. The Voronoi cell encloses the part of space that is closer to the center atom than any other atoms. This method can be used to unambiguously determine the CN without the need of a cutoff: those and only those atoms sharing a common cell surface are considered nearest neighbors. For MGs with more than one species, the bisection can be weighted by the atomic size, but it should be noted that such a weighted approach is not mathematically rigorous: the space may not be completely and uniquely divided into Voronoi cells if the bisecting points are not at the center [92]. The Voronoi cell can be labeled by the Voronoi index (e.g., a four-number vector  $\langle i_3, i_4, i_5, i_6 \rangle$  [93]) to describe the arrangement and symmetry of the nearest-neighbor atoms around the center atom. Specifically,  $i_3$  represents the number of triangles on the Voronoi polyhedron,  $i_4$  the number of quadrangles,  $i_5$  the number of pentagons, etc. The Voronoi index is closely related to the CNA index and the H-A index. In MGs, the  $n$ -edged polygon between the bonding atoms is usually associated with  $n$  common neighbors surrounding the pair, and such a configuration would constitute an “ $n$ -fold bond” local environment, as also indicated by the  $j$  in the CNA or H-A index.

## 2.2. Experimental techniques

The structures of simple crystals are highly degenerate so that solving the crystal structure can be eventually simplified to identifying the unit cell and the limited types of Bravais lattice. In other words, for crystals, much of the structure puzzle is solved *a priori*. For MGs, however, direct reconstruction of the 3-D structure, even locally, is a very difficult proposition. Many experimental techniques can be used to extract statistical information about the average glass structure, but the data usually cannot provide a complete picture. Nevertheless, the experimental results still serve as a yardstick against which any hypothetical structural model should be verified.

### 2.2.1. X-ray/neutron diffraction

X-ray diffraction (XRD), or neutron diffraction, is a widely used technique for structural analysis. The integrated diffraction pattern for amorphous materials is often diffuse, with a wide first diffraction maximum (halo), and several others that damp and diminish quickly. Experimentally, the measured scattering intensity can be related to the total structure factor (Eq. (4)) via [83]:

$$S(q) = \frac{I_C(q) - \langle f^2 \rangle + \langle f \rangle^2}{\langle f \rangle^2} \quad (13)$$

where  $I_C$  is the coherent scattering obtained after processing the original data (e.g., removal of background, multiple and incoherent scattering, etc.),  $\langle f \rangle$  is the average atomic scattering factor  $\langle f \rangle = \sum_x c_x f_x$ . The difference between XRD and neutron diffraction is the  $q$ -dependence of  $f$ : the scattering factor is a function of  $q$  for X-ray, but independent of  $q$  in the case of neutron. This is due to the difference in the basic scatterer (and its spatial distribution), i.e., electron cloud for X-rays, and atomic nucleus for neutrons [83].

The total structure factor can be converted into real space atomic/electron density distribution via Fourier transformation to obtain the total PDF, as mentioned in Section 2.1.2. For multicomponent BMGs, such a total pair correlation is insufficient to reconstruct the 3-D structure, due to the degenerate nature of the 2-D scattering data in mapping the 3-D configuration. It is thus desirable to obtain all the partial PDFs. To this end, one needs multiple element-specific measurements. The anomalous XRD and isotope substitution techniques are often used in this effort.

The atomic scattering factor  $f$  is not sensitive to the X-ray energy except near the absorption edge. This suggests that if one intentionally tune the X-ray energy to the absorption edge of a specific element, noticeable difference on the XRD spectrum would be observed, due to the change of scattering factor of the corresponding element (anomalous scattering) [83,94]. Since such a change is element-specific, the degeneracy is partially broken. One can then take advantage of this to solve the partial PDFs. If the anomalous scattering is measured for only one element  $\alpha$ , then only the differential PDF with respect to this element can be obtained:

$$g_\alpha(r) = \sum_\beta \frac{c_\alpha c_\beta f_\alpha f_\beta}{(f)^2} g_{\alpha\beta}(r) \quad (14)$$

To obtain all the partials, anomalous scattering for all elements should be measured.

Similarly, since the neutron scattering length of an element is usually different for different isotopes, an isotope substitution can be used to “label” a specific element without affecting the structure and chemistry. As a result, the associated structure factors (and the differential PDFs) involving this element can be measured using neutron diffraction [83]. Again, substitution for an element leads to one differential PDF, and substitution for every element would be needed in order to solve all the partials PDFs. This procedure is valid in principle, but often difficult in practice, especially for BMGs containing more than two elements.

Very recently, new XRD techniques have been proposed and developed to uncover more details regarding the local packing symmetry and 3-D structure of amorphous materials, such as the X-ray cross correlation analysis (XCCA) [95], and ankylography [96]. The applicability of these methods in MGs is still to be tested.

### 2.2.2. X-ray absorption fine structure

X-ray absorption fine structure (XAFS), including the extended X-ray absorption fine structure (EXAFS) and X-ray absorption near edge structure (XANES), is a commonly used method for structural characterization [97,98]. XAFS measures the element-specific and energy-resolved absorption coefficient of a material. When the X-ray travels inside a material, its intensity decays following [98]:

$$I = I_0 e^{-\mu x} \quad (15)$$

where  $I_0$  is the intensity of the incident X-ray,  $x$  is the depth into the material,  $\mu$  is the absorption coefficient, and  $I$  is the measured X-ray intensity after absorption.

Every element has its featured absorption edges (such as  $K$  and  $L$ ) corresponding to the different energies to activate its (e.g.,  $K$  shell,  $L$  shell) electrons. For a particular element in the MG, one can measure the absorption spectrum around the absorption edge, and the measured XAFS can be written as

$$\chi(E) = [\mu(E) - \mu_0(E)]/\Delta\mu_0 \quad (16)$$

where  $E$  is the X-ray energy,  $\mu_0(E)$  is the atomic-like background absorption, and  $\Delta\mu_0$  is the normalization factor which is the step height at the absorption edge.

The post-edge line on the XAFS usually exhibits undulation (see Fig. 12), which is due to the interaction of the photoelectron from the excited core atom with the neighboring non-excited atoms: the backscattered electron waves interfere with the forward propagating waves, modulating the absorption coefficient. Consequently, XAFS is capable of describing the average local environment around a specified element [98].

Within the first 30 eV of the edge position (i.e., XANES), the scattering and local atomic resonances are strong, and various physical effects have significant contributions to the observed spectra. Moreover, when the photoelectron energy is low (in this near-edge region), the multiple scattering, which is sensitive to the spatial arrangement (i.e., multi-body correlation) between the nearest-neighbor atoms, becomes important. All these make the interpretation of the XANES results difficult. Fortunately, with the help of *ab initio* calculation, the local electronic environment of various atomic clusters can be described to yield approximate predictions of the XANES. Comparison with the experimentally measured XANES would suggest what local structure is likely to exist in the sample material [98–100].

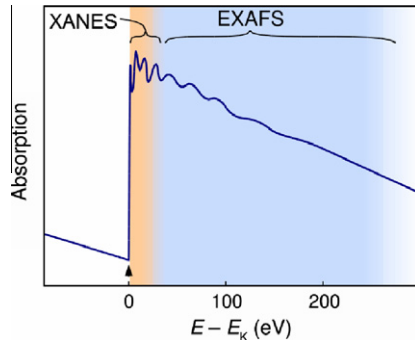


**Fig. 12.** Schematic of X-ray absorption spectrum including XANES and EXAFS (courtesy of Dr. H.W. Sheng).

Beyond  $\sim 30$  eV above the absorption edge (i.e., the EXAFS regime), the undulation is related to the local structure in a relatively simple way, as the multi-body effect is not as significant as in XANES. The widely used formulation of EXAFS is

$$\chi(k) = \sum_R S_0^2 N_R \frac{|f(k)|}{kR^2} \sin(2kR + 2\delta_c + \Phi) e^{-2R/\lambda(k)} e^{-2\sigma^2 k^2} \quad (17)$$

where  $R$  is the interatomic distance,  $N_R$  is the CN,  $\sigma$  accounts for the uncertainty due to thermal fluctuation and structural disorder (assuming Gaussian distribution),  $f(k) = |f(k)|e^{i\Phi(k)}$  is the backscattering amplitude,  $\delta_c$  is central-atom partial-wave phase shift of the final state,  $\lambda(k)$  is the energy-dependent EXAFS mean free path, and  $S_0$  is the overall amplitude factor. Some parameters in the above equation can be estimated using *ab initio* calculations [98,99].

For amorphous materials with multiple components, at the absorption edge of element  $\alpha$ , the EXAFS can be calculated via:

$$\chi_\alpha(k) = \sum_\beta S_{0\beta}^2 \frac{|f(k)|}{k} 4\pi\rho \frac{N_\beta}{N} \int g_{\alpha\beta}(r) \sin(2kr + 2\delta_c + \Phi) e^{-2r/\lambda(k)} dr \quad (18)$$

Similar to the diffraction experiments, XAFS for one element solves the corresponding differential PDF. To resolve all the partial PDFs, one needs to do XAFS measurements for each and every element. Also note that reliable information provided by XAFS is often limited to the nearest-neighbor shell.

### 2.2.3. Fluctuation electron microscopy

Fluctuation electron microscopy (FEM) is an electron microscopy technique that is especially sensitive to medium-range (of the order of 1 nm) structural features [101,102]. By sweeping across the sample using nanometer-sized X-ray beam and measuring the fluctuation of the scattering intensity, one can assess the degree of ordering over medium range in the material. If the glass is completely featureless and isotropic at the length-scale of the beam size, the FEM should yield no obvious fluctuation. However, if certain medium-range structural correlation does exist, which makes the structure anisotropic at the corresponding length-scale, the FEM may measure significant fluctuations due to the different orientations of the medium-range-sized clusters across the sample, see Fig. 13. This method has been demonstrated to be very effective for detecting structural inhomogeneity in amorphous germanium and silicon, where the medium-range structure resembles the crystalline order, forming entities that are called paracrystals [103,104]. However, FEM is recently found to be not sensitive to the MRO in monolithic MGs, and requires nanocrystals at 1 nm scale or pseudo-planar arrangement of atoms to produce significant FEM signal [105,106]. Therefore, how to interpret the previously measured FEM results in some Al-based and Zr-based MG samples [107,108] is still unclear: the medium-range structures detected may be due to pre-existing (quenched-in) crystalline nuclei in the sample and not indicative of intrinsic MRO in fully amorphous MGs.

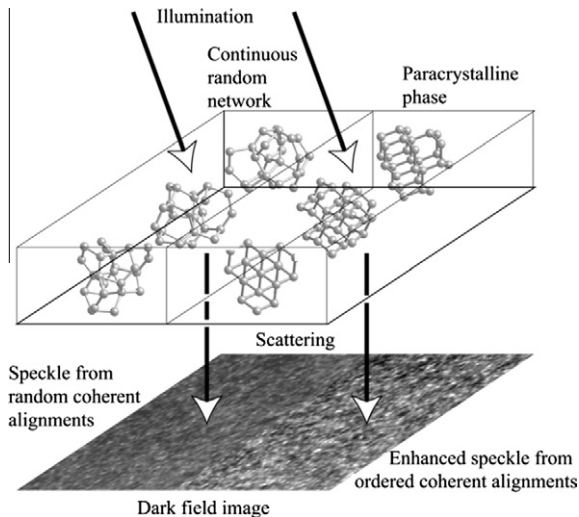


**Fig. 13.** A sketch showing how FEM works in detecting medium-range structural correlation. (Reproduced from [101] with permission © 2005 by Institute of Physics.)

#### 2.2.4. Transmission electron microscopy

Transmission electron microscopy (TEM), and high-resolution TEM (HRTEM), enable direct observation of atomic-level structure, but only as a projected 2-D image [109]. For crystals, this is not a major drawback as the 3-D structure can usually be derived from the 2-D image. This is, however, not possible for most glasses. As shown in Fig. 14, a typical HRTEM image of an MG exhibits a maze-like pattern with no discernable structure. In addition, due to the metastable nature of the MG, any energy-intensive process during the processing of the MG sample may introduce artifacts (e.g., deformation or ion-milling caused phase or structure changes). Oxidation, crystallization, and surface-mediated fluctuation can be induced during the TEM sample preparation as well (e.g., [110–114]). Therefore, although HRTEM imaging has been widely used to confirm the amorphous nature of the sample (locally), or to study heterogeneities such as voids or nanocrystals [115–117], it has rarely been used to quantitatively study the MG structures.

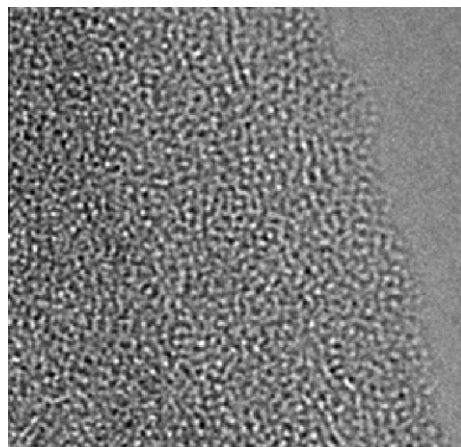


**Fig. 14.** HRTEM image of an Al<sub>89</sub>La<sub>6</sub>Ni<sub>5</sub> MG (courtesy of Dr. G.Q. Li).

Besides direct imaging, the TEM can be used to provide structural information in a different way, via electron diffraction. Similar to X-ray, the high energy electrons are also diffracted by the atoms when traveling through the material, and the diffraction spectrum conveys information about the atomic-level structure and can be converted to structure factor and PDF. Different from XRD, this approach using the high energy electron beam in TEM probes structure in the very small local region of a very thin TEM sample (the typical thickness is tens of nanometers, much smaller than the coverage of conventional X-ray beam). Taking advantage of this feature, electron diffraction analysis has been used to detect nanoscale structural fluctuations in a seemingly homogeneous MG sample [118]. Recently, by using the state-of-the-art spherical aberration-corrected (Cs-corrected) TEM, Hirata et al. [119] successfully aligned and focused the coherent electron beam to a diameter as small as ~0.3 nm. This has allowed the first measurement of electron diffraction patterns from individual atomic packing clusters, enabling direct experimental study of the local order (SRO) in MGs [120].

### 2.2.5. Nuclear magnetic resonance

The nuclear magnetic resonance (NMR) technique [121] has been applied to study the local symmetry around certain atoms in MGs [122–128]. The NMR measures the electric field gradient around the quadrupole nuclei, which is indicative of the local symmetry because it vanishes under cubic and higher local symmetries such as perfect icosahedral order. The advantage of NMR method is its high sensitivity to element-specific local symmetry. The disadvantage, however, is that it only detects the degree of high-order symmetry, but cannot determine the exact type of the symmetry. Also, NMR alone would not be able to resolve the structural details such as the CN and bond angle.

## 2.3. Computational methods

Computer simulation provides an alternative and also effective approach in solving and studying the MG structures. It not only helps to construct and visualize the 3-D structure, but also allows in-depth analysis of atomic-scale details that may lead to insights into the underlying mechanisms. For example, computer simulation is especially powerful in providing information otherwise not possible in experiments regarding the microscopic processes of supercooled liquid and glass formation, as well as in revealing the structure–property relationships (e.g., [79]). However, the computer models may also have serious limitations, as will be discussed below. One must constantly keep in mind the large disparity between the computer world and the real world, in terms of the time and spatial scales involved, when extending the simulation results to explain experimental observations.

### 2.3.1. Reverse Monte Carlo modeling

The goal of reverse Monte Carlo (RMC) method [129] is to search and find an atomic configuration that can reproduce (within a designated tolerance) certain structural parameters (e.g., the structure factor) extracted from a target material with unknown structure (e.g., measured in experiments on a realistic sample). The RMC-generated configuration is thus a candidate that may possibly have similar structure as the target.

To achieve this, the following iteration is often used: (1) randomly move the atoms to sample the configurational space, (2) calculate the normalized difference between the structure parameters from the trial configuration and the target configuration ( $\delta^2 = \frac{|\Omega_{\text{trial}} - \Omega_{\text{target}}|^2}{|\Omega_{\text{target}}|^2}$ ), which is the “energy” term, (3) determine a “temperature” term ( $\sigma^2$ ) and then calculate the fit residue ( $\chi^2 = \frac{\delta^2}{\sigma^2}$ ) and (4) compare the current fit residue with the one in the previous cycle ( $\chi_0^2$ ). If  $\chi^2 < \chi_0^2$ , the move is accepted; if  $\chi^2 > \chi_0^2$ , it is accepted with probability  $\exp [(\chi_0^2 - \chi^2)/2]$  (Metropolis algorithm) [129].

While repeating the above iteration, the “temperature” term ( $\sigma^2$ ) can be reduced gradually in a “simulated annealing” procedure to mimic the quenching process, such that the “energy” term ( $\delta^2$ ) is also decreasing, until it reaches a designated tolerance ( $\delta_0^2$ ). The tolerance could be a pre-determined value, or the error bar of the experiment. There are several experimental data sets that can be used with RMC, such as the measured structure factor, EXAFS, XANES, and FEM signals. In this sense, RMC is not a stand-alone computational method, but relies on external input as constraints.

In recent years, RMC has been widely used to construct the structure of MGs. However, it should be used with caution, because this “trial and error” technique does not yield unique results and sufficient constraints must be applied to ensure a physically stable and meaningful configuration. Specifically, since the RMC samples the configurational space in a random manner, the final configuration is essentially the most random structure that can reproduce the target structural parameters within the given tolerance. If the constraints are not strong enough, the system may conceivably end up in a state with unrealistically high energy, because there is no consideration of interatomic interactions in the RMC fitting. In light of this, for systems containing more than one element, one may need to at least include the partial PDFs or equivalent information in RMC fitting, as suggested by previous studies on the uniqueness of RMC-generated configurations [130,131], and a recent example for MG [132]. For multicomponent or complex BMGs, simply fitting the total structure factor or the total PDF is insufficient; often it is easy to fit the total structure factor, but the latter can be produced by various combinations of partial structure factors. Multiple independent constraints should be considered, such as the XRD (anomaly and/or isotope), neutron diffraction, EXAFS, and FEM, as well as theoretical constraints involving the interatomic interactions [106,133–137].

### 2.3.2. Molecular dynamics simulation

The principle of molecular dynamics (MD) simulation is to predict the motion (trajectory) of classical objects following Newton's equations [138–140]. At any moment  $t$  when all ion positions and velocities are given, if the force on the ions can be calculated, one may predict the acceleration of each ion and the position of ions at  $t + \Delta t$ . This can be repeated to generate the particle trajectories. During this process, the physical quantities (e.g., pressure, temperature) at any time are calculated using the instantaneous position and velocity of the atoms, and the equilibrium physical state of the material is described by the ensemble average of these instantaneous values. In addition to the NVE (constant number of particles, volume, and energy) ensemble as realized by the original Newton's equations in isolated systems, various other ensembles have been implemented in MD simulations, such as the NVT (constant number of particles, volume, and temperature) and NPT (constant number of particles, pressure, and temperature) ensembles [141,142].

Besides MD, the ensemble in phase space can also be sampled by the Monte Carlo (MC) method [138–140], where the atoms are not moved as predicted by the Newton's equations, but randomly followed by an algorithm to determine whether or not the motion is to be accepted. By designing the condition of acceptance, one can achieve the same probability distribution in the phase space (i.e., the same ensemble).

The key step in both MD and MC simulations is the determination of the force (or potential energy) associated with each atom. There are different ways to calculate the force, with different accuracy and different computational efficiency. Due to the limitations of current computational power, the accuracy and efficiency may not be achieved simultaneously. One thus needs to find a balance, so that the specific problem can be solved with meaningful output and also within acceptable computing time.

### 2.3.3. Quantum molecular dynamics

Often called *ab initio* MD or first-principles MD, the quantum mechanics approach has been used recently to study the structure of liquids and MGs. This approach solves the electronic structure and interatomic interactions based on the density functional theory (DFT) [143–150]. The description of energy, force and dynamic process using *ab initio* MD has been demonstrated to be very accurate when the calculation is conducted properly. An important issue is, however, what is a “proper” calculation. First of all, not all materials can be modeled using current *ab initio* MD algorithms. The multi-body problem of the interacting electrons is significantly simplified by the Kohn–Sham ansatz to an independent-particle system, with the exchange-correlation term accounting for all many-body effects. The simplification makes the computation of complex electron systems feasible, and constitutes the basis of most *ab initio* MD used today. Unfortunately, so far there is no systematic way to determine the exchange-correlation functional. The commonly used methods include local density approximation (LDA) and generalized gradient approximation (GGA), both of which assume that the exchange-correlation energy can be fully determined by the local profile of the electron density

distribution. It turns out many systems can be well described using LDA or GGA, but there are also many cases for which LDA and GGA alone cannot produce satisfactory results (e.g., some rare earth metals with localized *f* electrons). Second, not all properties can be directly characterized using *ab initio* MD. The calculation is only expected to be accurate for the ground state energy and electron density (if the Kohn–Sham ansatz and the exchange-correlation functional are correct). Processes in which excitations are important require separate considerations, often in the frame of perturbation theory. Third, not all material states can be simulated using a single set of parameters. For example, ferromagnetic materials such as Fe could be paramagnetic at high temperatures (above Curie temperature). Therefore, when simulating high temperature Fe liquid, one may use non-spin-polarized setup for the electrons, while for Fe-based MGs at low temperatures, spin-polarized assumption is more appropriate [151]. This has to be an input parameter because the *ab initio* MD only solves the ground state of electrons for a given atomic configuration, and thus cannot reproduce the ferromagnetic–paramagnetic transition due to thermal agitation.

Although *ab initio* MD has advantage in accuracy, and has been recently used successfully to study the structure of binary, solute-lean MGs [152], it alone is often inadequate in reproducing the structure of multicomponent BMGs. First of all, the simulation time-scale of *ab initio* MD is on the order of ~ps, and the average displacement of atoms within such a short time, even in the equilibrium liquid, is no more than ~1 nm. This suppresses the development of any structural order significantly different from the high temperature melts. Second, the *ab initio* MD simulation can handle only ~100 atoms for reasonable computing time. As a result, in the simulation box there may be only a few alloying (solute) atoms, and significant statistical fluctuation is thus likely. Moreover, the periodic boundary conditions applied on the small box (~1 nm) may impose constraints on the type/degree of order developed. Third, *NPT* quenching, which is the case in laboratory, is highly computationally intensive for *ab initio* MD. Therefore, *ab initio* MD may be more suitable for studying liquid structure and properties; for glasses, the structures obtained by *ab initio* MD quenching, especially for multicomponent BMGs, are expected to be quite different from those in the laboratory samples, even though some similarities of the main structural features are possible.

### 2.3.4. Classical molecular dynamics

The above mentioned difficulties can be alleviated, although only partly, by using classical MD employing empirical potentials to describe the force field. By assuming different expressions for the potential energy term, one can study different types of systems. For example, for the most commonly used Lennard-Jones (LJ) potential, the potential energy between two atoms is [138]:

$$V_{IJ} = 4\epsilon \left[ \left( \frac{\sigma}{R_{IJ}} \right)^{12} - \left( \frac{\sigma}{R_{IJ}} \right)^6 \right] \quad (19)$$

where  $R_{IJ}$  is the distance between atom  $I$  and atom  $J$ :  $R_{IJ} = |\vec{R}_I - \vec{R}_J|$ .  $\epsilon$  and  $\sigma$  are parameters that define the main character of the potential:  $\epsilon$  quantify the depth of the potential, while  $\sigma$  gives the minimum point of the potential via  $R_{min} = \sqrt[6]{2}\sigma$ . The total potential energy can be solved by adding the potential energy of each pair.

The LJ potential is a pair potential. It has simple expression so that the calculation is fast. LJ potential is found suitable for simulating noble gases such as argon, or other systems with van der Waals interactions, but it is usually insufficient for modeling metallic materials [153].

The embedded-atom method (EAM) potential is more sophisticated in the sense that it is a many-body potential. In EAM, the potential energy of an embedded atom  $I$  can be expressed as [154,155]:

$$E_I = F_\alpha \left( \sum_{J \neq I} \rho_\beta(R_{IJ}) \right) + \frac{1}{2} \sum_{J \neq I} \Phi_{\alpha\beta}(R_{IJ}) \quad (20)$$

where  $\alpha$  and  $\beta$  are the element types of the center (embedded) atom  $I$  and the neighboring atom  $J$ , respectively.  $\rho_\beta$  is the charge density function of  $\beta$ ;  $F_\alpha$  is the embedding function of  $\alpha$ ;  $\Phi_{\alpha\beta}$  is the pair potential function between  $\alpha$  and  $\beta$ . Note that the charge density here is the “effective” density for

EAM, not the true charge density. The total potential energy of the system is the summation of the potential energy of each atom. It has been shown that with the embedding function accounting for the many-body effect, EAM may be used for modeling many metals [156–160].

In EAM, the many-body interaction is incorporated with spherical symmetry with no angular dependence. This simplification makes the potential relatively simple and the computations reasonably fast, but also results in some limitations for its application. Nevertheless, it is particularly suitable for simulation of metallic systems due to the non-directional nature of most metallic bonds. There are also improved empirical potentials that include angular dependence [161,162]. However, the accuracy sacrifices the efficiency.

In general, since the interatomic interactions are described using simpler expressions, the classical MD simulation runs much faster than *ab initio* MD. The time-scale can be extended to tens of nanoseconds for a system of reasonable size (larger than the typical length-scale of MRO). The NPT quenching can also be readily simulated. To study a realistic MG-forming system, the key is thus to obtain reliable and accurate empirical potentials, and this can be done by fitting the potential parameters with the data from experiments and *ab initio* calculations. This approach has been used extensively in our studies [163]. Note, however, that the use of empirical potentials cannot solve all the problems associated with simulation. The time-scale in MD simulation is still orders of magnitude shorter than the time-scale for realistic BMG formation. At short range where the chemical interaction is strong, it is expected that the main structural features and characteristic SRO (and perhaps MRO) can be reproduced qualitatively. At macroscopic level, however, the simulation results could be less relevant. For this reason, caution must be used when interpreting the observations in simulations and making connections with realistic BMGs. Despite the limitations, computer simulation is still a useful and often powerful approach for revealing the general trend, basic principles and atomic-level details.

### 3. Atomic-level structure of metallic glasses

In this section we will describe and discuss the atomic-level structure of MGs, in terms of the short-to-medium range structural (both topological and chemical) features. We will start from the simplest monatomic systems, and then consider the binary and multicomponent MGs. Prototypical MGs of different categories will be considered separately, as they usually have different structures. The structure of the MGs is also discussed in connection with that in their parent liquids. Several key structural models proposed over the past 50 years will be assessed, in light of the most-up-to-date information.

#### 3.1. Structure of monatomic liquids

The structure of liquid, particularly the supercooled liquid, is closely related to the structure of MGs. A key feature of the metallic liquid is its high packing density. It is known that pure crystalline metals have dense packing, such as in fcc and hcp lattices. Upon melting, the density only decreases by a few percent, indicating that the metallic liquid, while possessing no long-range ordering of atoms, is still rather dense. To achieve such high density and packing efficiency, the local atomic arrangements must be well correlated and exhibit certain degree of SRO and MRO. In other words, the nearest-neighbor atoms cannot be truly randomly arranged; instead, they must be ordered in some way and to some extent, to meet both topological (dense) and chemical (stable) requirements. The prevalence of the SRO around each and every atom naturally leads to correlations over medium range beyond the nearest-neighbor shell.

##### 3.1.1. Dense random packing of hard spheres

The pioneering work in solving the structure of metallic liquids was led by Bernal [164,165], Scott [166], and Finney [167,168]. If the atoms in metals are approximated as hard spheres, the question is then how to pack the 3-D space with identical hard spheres as densely as possible, without introducing crystalline order. This is Bernal's original idea of dense random packing (DRP) of hard spheres (DRPHS). Obviously, in a DRPHS, there should not exist a hole (empty space) that is sufficiently large to accommodate one more identical sphere without adjusting its neighbors. Given this, Bernal

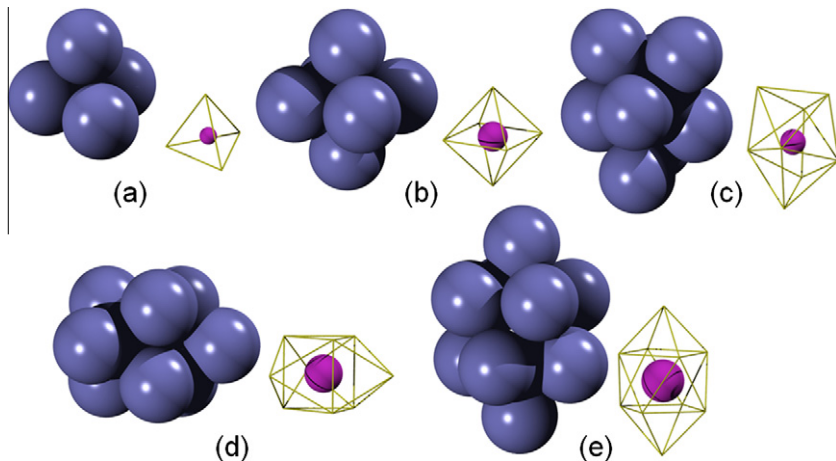


**Fig. 15.** Bernal's canonical holes: (a) tetrahedron (b) octahedron (c) tetragonal dodecahedron (d) trigonal prism capped with three half octahedra (e) Archimedean antiprism capped with two half octahedra. In each panel, the left figure shows the hard sphere packing surrounding the hole, and the right figure shows the hole in the center (the radius of the pink sphere corresponds to the size of the hole).

proposed that five types of holes with edges of equal length (i.e., equilateral triangle faces) are likely the basic structural units of monatomic liquids, as shown in Fig. 15.

Among the five polyhedral holes, tetrahedron has the highest packing efficiency, because each atom in the tetrahedron is in contact with all the other three atoms. The other polyhedral types have larger holes with lower packing efficiency. Unfortunately, a 3-D space tiling cannot be fulfilled with the equilateral tetrahedron only, thus other holes must be involved. For example, in the close-packed fcc/hcp structure, tetrahedra (Fig. 15a) and octahedra (Fig. 15b) are involved (the number ratio of tetrahedra and half octahedra is 1:1 per unit cell), and they are fully ordered to fill the entire 3-D space. The polyhedra in Fig. 15c–e are incompatible with long-range translational symmetry, and they are believed to be present in liquids. In fact, since there is no global “regulation” of the holes in liquids, while the system strives to maximize the number of tetrahedra (i.e., the tetrahedrality [169]), other types become inevitable and naturally emerge, and the liquid structure is thus a “mixture” of these five basic units (with moderate distortion, i.e., edges are not precisely equal, but approximately equal). Experiments and computer modeling have been employed to produce and analyze a DRPHS. For example, in a steel bearing experiment, Bernal found ~70% tetrahedra, 20% half octahedra, together with all others holes (with distortions) [165]. In a computer generated DRPHS, Barnett et al. [170] and Sadoc et al. [171] observed similar features. Note that the fraction of tetrahedra in the DRPHS is even higher than that in fcc/hcp structure, although the overall packing efficiency of DRPHS is lower. This is because the large holes contained in a DRPHS, while only a small fraction, take a rather large space. The regularly distributed octahedral holes in fcc/hcp are no longer seen in the DRPHS, and the corresponding empty space is now randomly redistributed (and to some extent concentrated) among various types of holes. The spatial aggregation of tetrahedra in the DRPHS leads to many five-edged faces, as noticed by Bernal [165] and Finney [167]; this feature will be discussed in more detail below.

The above idea can be better perceived in a bottom-up approach. Starting from a center atom, we pack atoms around it one by one; each atom is required to touch three others to form an equilateral tetrahedron. The resulting structure is the so-called polytetrahedral packing [172]. We can pack at most 12 atoms this way until it is impossible to put in the 13th, but the 12 atoms leave a gap in the shell, see Fig. 16. Such a gap originates from the long-recognized fact that the 3-D space cannot be tiled with equilateral tetrahedron only, which is termed packing frustration by Nelson and Spaepen [172,173]. There are two ways to deal with the gap. One may either move the 12 atoms around to form eight tetrahedra and accommodate the empty space in the six half octahedra, and such a cluster is the unit of fcc/hcp packing (Fig. 16). Alternatively, one may also homogeneously redistribute the empty

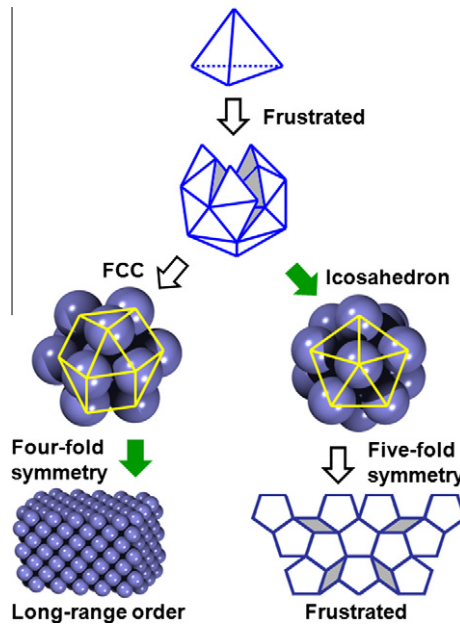


**Fig. 16.** Frustration map of the polytetrahedral packing of identical hard spheres. Green solid arrow points to the optimal choice at each stage.

space among the 12 shell atoms such that they do not really touch each other, and that leads to an icosahedron with 20 slightly distorted tetrahedra (edges formed between neighboring shell atoms are 5% longer). The former scheme, with octahedra involved, is no longer a polytetrahedral packing; while the latter is still of polytetrahedral nature, despite the slight mismatch of bond length. It is interesting to note that the latter packing scheme is characterized by five-edged faces, which were indeed observed in DRPHS. Compared to the fcc/hcp cluster, the icosahedron has better rotational symmetry and establishes more bonds (Fig. 16). Therefore, as far as a cluster with 13 atoms is concerned, icosahedron is actually a more preferable arrangement than fcc/hcp, and it could be the dominant structure in monatomic liquids, as originally postulated by Frank [174] in 1952. This local motif will be encountered time and time again in our discussions on the structures of MGs and liquids, in the rest of this review.

However, if one tries to pack the 3-D space with the icosahedral clusters, packing frustration arises again due to the incompatibility of the fivefold rotational symmetry with long-range translational order, see Fig. 16. In other words, although the icosahedron outperforms fcc/hcp in dealing with the short range frustration, it induces long-range frustration that would otherwise be non-existent for fcc/hcp. Such a “dilemma” leads to confusion, so that the liquid and crystal have different optimal choices for the atomic arrangement in the nearest-neighbor shell. The sizable barrier for the transition from the icosahedral packing in the amorphous state to the long-range ordered crystals, therefore, can be the structural basis for the supercooling observed for metallic liquids [172–174].

The packing frustration has a geometric origin, as described by Coxeter [175] in terms of curved 3-D space. Its physical relevance is further emphasized by Sadoc [176] and Nelson [173,177]. Here we give a brief introduction following Ref. [172]. It is obvious that there is no frustration for 2-D packing of identical hard spheres on a flat surface, as six spheres surrounding the center sphere on the plane fits perfectly with sixfold rotational symmetry, and this can be repeated infinitely to cover the entire surface. However, imagine we have a curved 2-D surface (e.g., on a spherical surface with very large but finite radius), frustration would arise if we try the same packing, because on average, the number of spheres that can pack closely around the center sphere is no longer an integer, but

between 5 and 6. This means that the packing cannot be perfect, and at some point, we either have to have a missing sphere, or need to insert an extra sphere to fill the gap. The sixfold environment is violated at such points (becoming fivefold or sevenfold). These points are thus rotational defects called disclinations [173], analogous to the translational defect (dislocation) in conventional crystals. The scenario can be naturally extrapolated to a 3-D space. Although the flat 3-D space cannot be filled with equilateral tetrahedra only (the average CN is not an integer, but between 12 and 13), the packing could be accomplished in some *curved* 3-D space (i.e., a 4-D space), where 20 equilateral tetrahedra form a perfect icosahedron with fivefold symmetry, which repeats itself infinitely to fill the space. In such a curved 3-D space, the icosahedral phase would be a true ground state at both short range and long range. Unfortunately, the projection from that curved 3-D space to the realistic flat 3-D space introduces packing frustration and inevitably packing defects (e.g., disclinations corresponding to fourfold or sixfold bipyramids with missing or extra tetrahedron [173]), so that the icosahedral phase is destabilized, especially over long range. As a way out, the fcc/hcp structure, which is not a polytetrahedral packing but has fourfold symmetry compatible with long-range translational order, becomes the ground state for many bulk crystalline metals, Fig. 16. In this sense, the fact that we are living in a flat 3-D space may be the ultimate origin for the complex glass/liquid behavior.

### 3.1.2. Packing of soft spheres with pair potentials

Metallic bonds have minimal directionality compared to covalent bonds because the bonding electrons are not localized between atom pairs. For such an “ions embedded in electron gas” scenario, the general trend is that the more neighbors around the center atom (at a characteristic nearest-neighbor distance), the more ions sharing the valence electrons, and the lower the potential energy. This is the origin of the dense packing in metals. In the hard sphere model, the spheres are incompressible, and there are no attractive interactions between the spheres either. A more realistic yet still simple approach is to model the interaction of spheres using pair potentials, so that they are not only softened, but also have the potential energy as the driving force to achieve dense packing. Typical pair potentials include the LJ potential, Morse potential [178], Dzugutov potential [179], etc. see Fig. 17 for a comparison of these potentials. A common feature of these potentials is the energy minimum at an interatomic distance  $r_{eq}$ , which resembles the diameter of the hard sphere. In order to minimize the system potential energy, each atom prefers more neighbors at  $r_{eq}$ , so that by simulated quenching in MD or MC, dense packing would be approached. Although the simple pair potential is insufficient to describe the realistic interactions of metallic atoms, it is a useful tool to generate DRP in computer, and to mimic the generic liquid behavior.

Early simulations employing pair potentials were conducted by Finney [168] and Hoare [180], and the icosahedral order was demonstrated to be pronounced. With the Morse potential, Doye and Wales

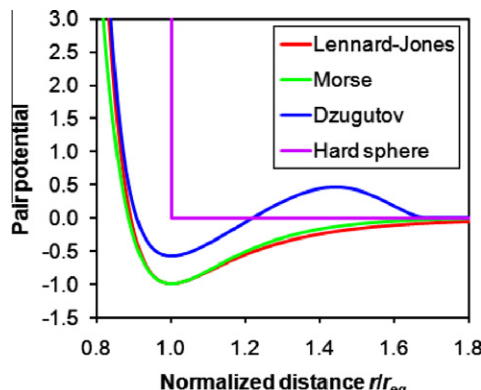


**Fig. 17.** Comparison of various pair potentials (with arbitrarily selected potential parameters). The effective potential for hard sphere model is also given.

[181] found that for small clusters, icosahedra indeed have lower energy than fcc/hcp clusters. The energy relation was also studied as a function of the cluster size and the hardness of the potential. Honeycutt and Anderson [90], using the LJ potential, compared the energy of fcc and Mackay icosahedron. They found that for fcc to have lower energy than icosahedra, the system should at least contain 5000 atoms. Steinhardt et al. [87,88] analyzed a configuration generated using LJ potential with bond orientational order, and the icosahedral structure is identified and quantified by the non-zero  $\tilde{W}_6$  and  $\tilde{W}_{10}$  parameters. Dzugutov introduced a second peak in the pair potential to destabilize fcc structure and avoid crystallization during simulated quenching; as a result, icosahedra were readily obtained and studied [179,182].

### 3.1.3. Supercooled pure metallic liquids

The relevance of the modeling work discussed above needs to be validated by experiments. The challenge is to achieve supercooling in pure metallic liquids. Turnbull [183] successfully supercooled Hg droplets in 1952, and demonstrated that metals can have a significant supercooled region if heterogeneous nucleation is suppressed. Reichert et al. [184] used evanescent X-rays to probe the structure of liquid Pb fragments at a solid–liquid (Si–Pb) interface, and fivefold local symmetry was observed. In recent studies, the electromagnetic/electrostatic levitation technique [185] has been developed and employed by Kelton, Holland-Moritz, and their co-workers. In such a container-less setup, supercooling has been achieved in several metals, including Fe, Zr, Ni, Co, Ti [186–190]. The supercooled liquids can be probed using XRD or neutron scattering. Interestingly, although these metals have different crystalline structures, the existence of icosahedral order in the liquids appears to be universal. The icosahedral order in supercooled Cu droplets was also confirmed by Di Cicco et al. [191], using XAFS and RMC. Despite this common feature, however, differences in structural details were also observed. For example, compared to Ni, the icosahedra in Ti liquid were found to be more distorted [188].

As an alternative approach, *ab initio* simulation based on DFT may also provide a fairly accurate description of the liquid structure. Supercooled liquids of Ni [192], Cu [193], Fe [194], Zr [195], Ta [196], and Ti [197] have been studied, and the structures have been analyzed using various techniques. On the one hand, the signature of (nearly) icosahedral order has been found in all the systems; on the other hand, however, the degree of icosahedral order and topological distortion are significantly different. In general, ETMs tend to have much more distorted icosahedra than LTM. For example, in supercooled Zr, a bcc-type order is found to be in competition with the icosahedral order [195]. In supercooled Ta, an A-15 structure was identified, which has a high degree of fivefold symmetry but a low fraction of complete icosahedra [196]. In Ti, the icosahedral order was again observed to be highly distorted [197]. The origin of the complexity is presumably the different electronic structure, as revealed by *ab initio* calculations of 13-atom clusters [198–200]. Therefore, the exact structure of pure metallic liquids is not simply determined by topology; the electronic interaction and bonding properties are also important. The hard/soft spheres or pair potentials are too simple to distinguish the structural details of realistic metallic liquids, although they may be able to capture the most general features from the topological perspective (e.g., fivefold symmetry, short-range icosahedral order).

## 3.2. Structure of LTM–NM metallic glasses

We now move on to discuss the structure of MGs. Many important MGs are made by mixing LTMs and NMs (such as the metalloids) at the composition around 3:1–4:1. Examples include the first MG ( $\text{Au}_{75}\text{Si}_{25}$  [1]), BMG with excellent GFA ( $\text{Pd}_{40}\text{Cu}_{30}\text{Ni}_{10}\text{P}_{20}$  [201]), BMG exhibiting sizable compressive plasticity ( $\text{Pt}_{57.5}\text{Cu}_{14.7}\text{Ni}_{5.3}\text{P}_{22.5}$  [202]), and the Fe-based BMGs (e.g., Fe–Cr–Mo–B–C [203]) with low cost and appealing mechanical and magnetic properties. To understand the structure of such LTM–NM MGs, binary systems such as Ni–P and Fe–B have been selected as the prototypes and studied by many researchers.

### 3.2.1. Model based on dense random packing of hard spheres

Early attempts in solving the structure of binary LTM–NM MGs were based on the DPRHS model, and led by Cargill [204,205] and Polk [206,207]. Cargill found good agreement between the measured

PDF of Ni-P and that of a DRPHS, and thus proposed that the structure of LTM-NM MGs could be represented by DRPHS. Cargill's model did not differentiate the LTM and NM atoms because they have similar Goldschmidt radii. Polk, however, noticed that treating both LTM and NM as identical hard spheres would result in a density smaller than experimental measurement. It was then proposed that only the LTM atoms assume the DRPHS configuration, while the NM atoms fill in the canonical holes. This postulation was justified by (1) the measured Ni-P distance is smaller than the sum of their Goldschmidt radii; (2) the composition of LTM-NM MGs is NM-lean and (3) the LTM has larger atomic scattering factor than NM, such that the LTM-LTM partial is dominant in the total structure factor or PDF. It should be noted that although the match of PDF is fairly good between the DRPHS and experiments, including the splitting second peak, the relative intensity of the sub-peaks is inconsistent. Better match of this feature was achieved by relaxation of DRPHS using pair potentials, as performed by von Heimendahl [208] and Finney [209].

### 3.2.2. Stereochemical model

The model based on DRPHS did not emphasize the chemical order, although Polk's approach did imply NM-NM avoidance. Hyperfine field measurement by Vincze et al. [210], EXAFS study by Hayes et al. [211], NMR study by Panissod et al. [122] and thermodynamic analysis by Allen et al. [212] all suggested strong chemical order in LTM-NM type MGs that cannot be explained by the DRPHS. These observations appear to support the stereochemical model proposed by Gaskell [213,214]. The core of Gaskell's model is that the SRO (nearest-neighbor shell) in glass is well-defined and almost always identical to that in the corresponding crystals, and the difference lies in the MRO, i.e., crystals have ordered packing of the stereochemical units, while the packing in glass is random. This model explained the structure of silicate glass very well. Gaskell proposed that it also applies for MGs, and the stereochemical unit for Ni-P is the tri-capped trigonal prism (TTP) with nine Ni atoms in the shell (six for the trigonal prism and three for the caps) and one P atom in the center, see Fig. 18. This structure is indeed found in the crystalline  $\text{Ni}_3\text{P}$  compound (with a large unit cell). Following this approach, Gaskell successfully reproduced the PDF measured in experiments. The key question is, then, how the TTP units fill the space in a dense and efficient manner, but different from the  $\text{Ni}_3\text{P}$  crystal. Their packing and connection could be disordered, but certainly not featureless. Gaskell suggested a chain-like connection of the trigonal prism by sharing edges (Fig. 18). In a more detailed treatment by Dubois et al. [215], a chemical twin model was used to approximate the packing of TTP units.

### 3.2.3. Efficient packing of quasi-equivalent NM-centered clusters

Gaskell's model based on TTP units has been very successful in some LTM-NM MGs. However, a number of questions remain. First, is the TTP unit universal for this type of MGs? Experiments and simulations show that the TTP unit could be distorted in some LTM-NM MGs, and other types of structural unit may emerge. For example, by comparing the PDF obtained from neutron diffraction, Waseda and Chen [216] found that the local structure of Fe-B could be different from that in Fe-P. Boudreax

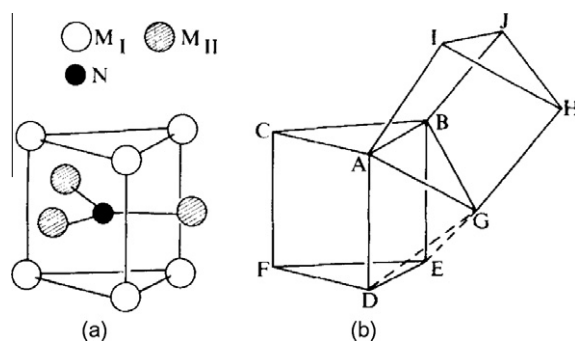


**Fig. 18.** Gaskell's stereochemical model for LTM-NM MGs. (a)  $N$  is the NM atom,  $M_I$  and  $M_{II}$  are the LTM atoms. (b) Chain-like connection of the TTP units. (Reproduced from [213] with permission © 1978 by Nature Publishing Group.)

and Frost [217], in their computer simulated Pd–Si, Fe–P, and Fe–B, found two different structural units: octahedron and trigonal prism, and the relative occurrence is composition dependent. Lamparter [218] fit the measured partial PDFs of Ni–P using RMC, and found that the distorted P-centered TTP does not seem to be more ordered than randomly distributing nine Ni atoms around P. It is true that the RMC itself favors maximal randomness, but the result at least shows that distorted TTP can also fit the partial PDFs with almost perfect agreement. Evteev et al. [219] simulated  $\text{Fe}_{83}(\text{C/B/P})_{17}$  MGs and various structural units were found in addition to the TTP, including the octahedron and bi-capped square Archimedean antiprism (BSAP). The relative fraction of each type depends on which metalloid is involved, even though  $\text{Fe}_3\text{C}$ ,  $\text{Fe}_3\text{B}$ , and  $\text{Fe}_3\text{P}$  all have the same crystalline structure (with TTP unit). These results suggest the stereochemical model is inadequate to represent the general structure of LTM–NM MGs. First, the local structure is more complicated than being always identical to that in crystal, and is also likely to be system dependent and composition dependent. Second, how the structural units are packed, i.e., the MRO, is still unclear.

Recently, by combining XRD, EXAFS, RMC and *ab initio* simulation, Sheng et al. [152] resolved the structure of various MGs, with emphasis on the LTM–NM type. First of all, the solute–solute avoidance and strong chemical order are confirmed again. Second, it is found that the SRO around NM in MGs is not necessarily the same as in the crystals; the effective size ratio between the solute and solvent atoms plays an important role. Depending on the relative size of the LTM (e.g., Ni, Fe) and the NM (e.g., P, C, B), the dominant SRO could be TTP with Voronoi index of  $\langle 0, 3, 6, 0 \rangle$ , BSAP with Voronoi index of  $\langle 0, 2, 8, 0 \rangle$ , etc., with some other distorted clusters coexisting. The fractions of each type of polyhedra also vary with system and composition. For example, the SRO around B in  $\text{Ni}_{81}\text{B}_{19}$  was found to be predominantly TTP  $\langle 0, 3, 6, 0 \rangle$ , while the dominant SRO around P in  $\text{Ni}_{80}\text{P}_{20}$  was identified to be  $\langle 0, 2, 8, 0 \rangle$  (the competing crystals  $\text{Ni}_3\text{B}$  and  $\text{Ni}_3\text{P}$  both have the TTP local structure). The average CN in  $\text{Ni}_{80}\text{P}_{20}$  was determined to be 10.5 using Voronoi method, slightly larger than the value of 9.4 determined using atomic-pair distance cutoff. The distribution into various cluster types reflects the continuous nature and intrinsic distortion/variation of the local structure, which is different from Gaskell's assumption of a fixed stereochemical unit identical to that in the crystals with unambiguous CN and uniform bond length. The motif is system dependent and composition dependent, emphasizing the dominant role of the effective atomic size ratio. On the basis of the efficient packing of solute-centered clusters, the MRO was further proposed to be the DRP of these clusters by sharing shell atoms (face sharing, edge sharing, and vertex sharing [220]), as demonstrated by the fivefold character and icosahedral-like feature of the solute–solute correlation, see Fig. 19.

The experimental and computer simulation studies by Sheng et al. [152] and their observations of efficient packing of quasi-equivalent solute-centered clusters partly corroborates the hypothetical structural model proposed by Miracle [221]. However, there are also salient differences, which will be discussed in Section 3.7.2. in the context of a more general comparison of the various models.

### 3.2.4. Multicomponent LTM–NM metallic glasses and chemical heterogeneity

Based on the LTM–NM prototype, there are various multicomponent BMGs containing more than one TM and/or NM. The structure of these BMGs is expected to be related to but more complicated than the binary LTM–NM MGs. A complete structure of a multicomponent BMG is very difficult to solve, and only limited examples have been studied, revealing some characteristic structural features of these BMGs.

Egami et al. [222] studied the structure of Pd–Ni–P using anomalous XRD tuned at the Pd K-edge. By examining the differential and partial PDFs around Pd, it is concluded that Pd and Ni atoms mix with each other almost randomly, suggesting weak chemical SRO of Pd and Ni in Pd–Ni–P. The excellent GFA of this alloy is thus mainly due to the destabilized competing crystals, instead of any unusual features of the glass. The destabilization was explained by the fact that  $\text{Pd}_3\text{P}$  and  $\text{Ni}_3\text{P}$  crystal structures are different and complex, and it is even more difficult to form  $(\text{Pd}-\text{Ni})_3\text{P}$  crystals. Alamgir et al. [223], using EXAFS and extended energy loss fine structure techniques, investigated the structure of  $\text{Pd}_{x}\text{Ni}_{(80-x)}\text{P}_{20}$  BMGs. It was found that the local environment of Pd in  $\text{Pd}_{60}\text{Ni}_{20}\text{P}_{20}$  glass resembles that in the  $\text{Pd}_3\text{Ni}$  crystal, while the atomic-level structure of  $\text{Pd}_{30}\text{Ni}_{50}\text{P}_{20}$  glass is similar to the crystal structure of  $\text{Ni}_3\text{P}$ . The metal atom environment in  $\text{Pd}_{40}\text{Ni}_{40}\text{P}_{20}$  BMG appears to be a weighted average of  $\text{Pd}_{30}\text{Ni}_{50}\text{P}_{20}$  and  $\text{Pd}_{60}\text{Ni}_{20}\text{P}_{20}$  structures, but the structure around P is similar to  $\text{Pd}_{60}\text{Ni}_{20}\text{P}_{20}$ , rather

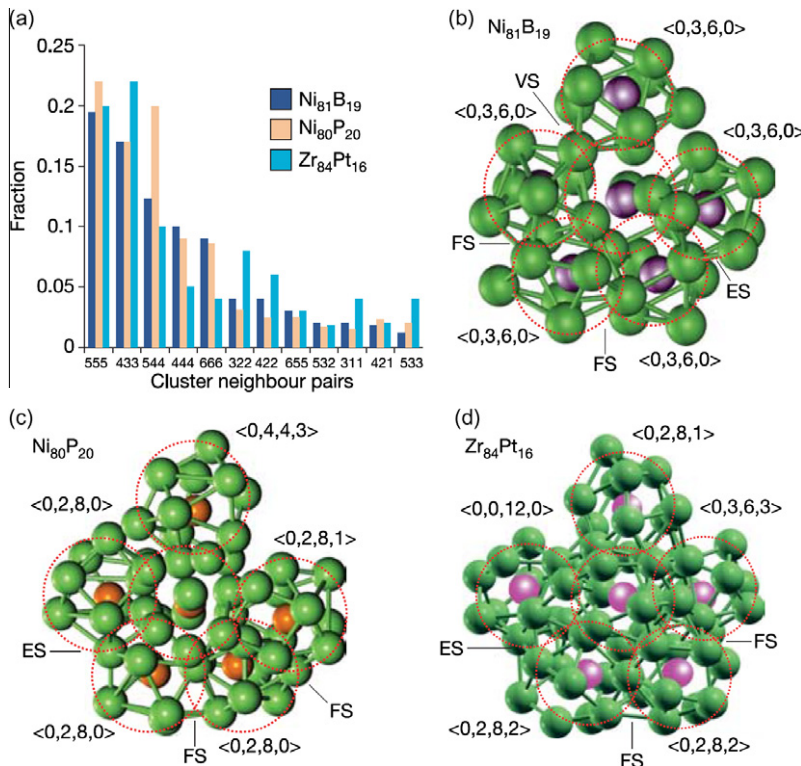


**Fig. 19.** Solute-centered clusters in several binary MGs and their efficient packing characterized by fivefold and icosahedral-like feature. (Reproduced from [152] with permission © 2006 by Nature Publishing Group.)

than  $\text{Pd}_{30}\text{Ni}_{50}\text{P}_{20}$ . The above results by Egami et al. and Alamgir et al. are essentially consistent, and suggest that in Pd–Ni–P BMGs, the P environment is well-defined (e.g., TTP or BSAP), while the Pd and Ni atoms surround the P centers randomly, with the local make-up scaling with the global composition.

Hirata et al. [224] studied the structure of  $\text{Pd}_{40}\text{Ni}_{40}\text{P}_{20}$  using HRTEM. While the average structural feature as indicated by the electron diffraction pattern is typical for amorphous materials, a close inspection reveals nanoscale fcc-like clusters (presumably Pd or Ni) embedded in an amorphous matrix; the latter is mainly composed of P-centered TTP units. In other words, the BMG sample has nanoscale phase separation, containing (subcritical) nuclei of fcc Pd/Ni, and such heterogeneity may not be easily detected in a macroscopic diffraction test. However, it is not clear if these fcc-like clusters are intrinsic of the glass, or they are present only because in their samples phase separation (such as primary crystallization) has already been initiated.

Starting from  $\text{Pd}_{40}\text{Ni}_{40}\text{P}_{20}$ , one may add Cu to substitute Ni, and the GFA is enhanced in  $\text{Pd}_{40}\text{Cu}_x\text{Ni}_{40-x}\text{P}_{20}$ . The best GFA is achieved at  $x = 30$  [201]. Tang et al. [225], using NMR, studied the hopping rate of P atoms as the composition of  $\text{Pd}_{40}\text{Cu}_x\text{Ni}_{40-x}\text{P}_{20}$  changes from  $x = 0$  to  $x = 30$ . It is found that the hopping rate increases significantly when  $x$  is increased to above 25, indicating structural changes beyond simple substitution of Ni with Cu. The higher hopping rate at  $x > 25$  indicates that the openness of the structure becomes higher, which is in good agreement with the composition dependence of molar volume as measured by Shen et al. [226]. Specifically, it was found that at  $x < 10$ , the molar volume of the MG increases linearly, and the slope is consistent with the atomic volume difference between Ni and Cu. However, at  $x > 10$ , the slope is notably larger, pointing to changes of the topological structure. In the meantime, the molar volume of the crystallized sample also increases dramatically. The origin

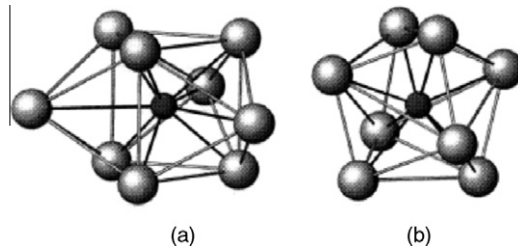


**Fig. 20.** (a) P-centered TTP structure with nine neighbors (b) P-centered transformed tetragonal dodecahedron with eight neighbors. (Reproduced from [227] with permission © 1999 by Japan Institute of Metals.)

for the above observations may be that the crystallized  $\text{Pd}_{40}\text{Ni}_{40}\text{P}_{20}$  and  $\text{Pd}_{40}\text{Cu}_{40}\text{P}_{20}$  have very different structures. The former is dominated by TTP where P atoms have nine neighbors with higher packing efficiency, while the latter is a tetragonal phase with P surrounded by eight atoms with greater openness (Fig. 20). Presumably, when Cu fraction  $x$  is larger than a critical value, there is a transition from “simple substitution of Ni with Cu in the  $\text{Pd}_{40}\text{Ni}_{40}\text{P}_{20}$  type structure” to “creation of local regions with  $\text{Pd}_{40}\text{Cu}_{40}\text{P}_{20}$  type structure”. The latter would lead to bifurcation of the P local structure into two different environments, as well as the non-uniform composition dependence of the P hopping rate and the molar volume. The above explanation was confirmed using the anomalous XRD by Park et al. [227], who found different local structures around Ni and Cu, which can be explained by assuming that Cu is associated with the tetragonal dodecahedral packing, while Ni is associated with the TTP. The scenario of two different chemical environments around P was further supported in a P 2p core-level photoemission spectroscopy study of  $\text{Pd}_{42.5}\text{Cu}_{30}\text{Ni}_{7.5}\text{P}_{20}$  conducted by Hosokawa et al. [228].

The bifurcation of local chemical SRO was also observed in other LTM–NM MGs. For example, FdezGubieda et al. [229] studied the SRO in  $(\text{Fe}_{0.2}\text{Co}_{0.8})_{75}\text{Si}_x\text{B}_{25-x}$  MG using XANES and EXAFS. Preferential coordination of B with Fe, and Si with Co, was found, and the bond length (Fe–B or Co–Si) is close to the summation of covalent radii, suggesting covalent-like bonding. May et al. [230] observed phase separation in the amorphous state before crystallization in a similar Fe–Co–Nb–Cu–Si–B system, indicating that there might be chemical heterogeneity in the as-quenched MG.

The above results for complex multicomponent LTM–NM BMGs have two important implications. First, chemical heterogeneity (or nanoscale phase separation) and subcritical nuclei could be fairly common, especially in samples processed under non-ideal (or not well-controlled) processing conditions. This is a major factor that needs to be considered when studying the structure of MGs in experiments. Since the nanoscale phase separation or embedded nuclei may not be detected by conventional XRD or neutron diffraction, and the probing beam size is usually much larger than the length-scale of heterogeneity, the measured data represent essentially an average. One usually extracts local structural motifs using the average information by assuming homogeneous structure. However, if internal heterogeneity exists, such an approach using conventional techniques may not be able to differentiate the various local environments and reproduce the true 3-D glass structure. Second, the nanoscale chemical heterogeneity is often caused by the substituting alloying elements which have a zero or positive heat of mixing with one or more of the existing solvent elements, e.g., alloying of Pd–Ni–P with Cu. Since both Ni and Cu form strong bonds with P, but do not attract one another, two different local environments may be created when the three elements are mixed. This process often leads to salient structure and property changes, including the GFA, as suggested by the examples above.

### 3.3. Structure of SM–RE metallic glasses

It is interesting to notice that in Al-based MGs, RE is usually involved, and in RE-based MGs, SM (mostly Al, sometimes Ga) is a faithful companion. The advantage of Al-based MG is its light weight

and high specific strength. However, the GFA of Al-rich alloys is relatively low, and BMG formation in Al-rich systems has only limited success [231–233]. Some RE-based MGs [234], particularly the Ce-based ones, have low elastic moduli and low  $T_g$  (e.g., close to room temperature). Therefore, they can be easily heated to the supercooled liquid regime and re-shaped like plastics [235].

### 3.3.1. Structure of Al-rich metallic glasses

The structure of Al-rich MGs has been studied using both experiments and computer simulations, and the results will be summarized and compared below.

Hsieh et al. [236,237] studied  $\text{Al}_{90}\text{Fe}_x\text{Ce}_{10-x}$  using XRD. Since the composition is very Al rich, the solute Fe and Ce were found to be surrounded by Al only. The average Al coordination around Fe and Ce and the bond lengths were extracted from the XRD data. The Al–Fe bond length was measured to be significantly shorter than the sum of their metallic radii, which the authors ascribed to the electron orbital hybridization between Al and Fe. Mansour et al. [238,239] studied Al–Co–Ce and Al–Fe–Ce, and further confirmed the bond shortening for Al–Co and Al–Fe pairs, as well as the smaller CN around Co/Fe than expected from the nominal metallic radii. The Al–Ce bond length and the CN of Ce, however, appear to be normal in both cases. These results indicate that the Al–Co and Al–Fe pairs indeed involve special electronic interactions, while the Al–Ce bond seems to be typical of metallic ones. Egami [240] pointed out that the strong and covalent-like Al–Fe interaction originates from the hybridization of the 3d-states of Fe with the sp-states of Al, and this is supported by the increasing melting temperature upon alloying some LTM (e.g., Fe) into Al. The bond shortening between Al and certain LTM (Fe, Co, Ni, Cu) and the typical metallic bond between Al and some REs (Y, La, Ce, Sm, Gd, Tb, Dy) were further addressed by Saskl et al. [241,242], Bacewicz et al. [243], and Zalewski et al. [244]. In addition, it is found that the RE-shell is much more disordered than the LTM-shell, as demonstrated by the broad first peak in the Al–RE partial PDF (dissociated from the total PDF) [241,242,244].

The above experimental results seem to be consistent. First of all, the Al-rich MG structure is a dense packing of Al–LTM clusters and Al–RE clusters, in which the solute LTM and RE are surrounded by the solvent Al only. The Al–LTM bond length is shortened to be  $\sim 2.5 \text{ \AA}$  (for Fe, Co, Ni), and the Al CN around the LTM solute is 6–7. The Al–LTM bond has covalent-like nature due to the strong interaction between LTM 3d electrons and Al sp electrons. The Al–RE bonds, however, have no significant shortening, and the Al CN around the RE solute is  $\sim 16$ , consistent with the expected value from the ratio of the metallic radii. The Al–RE bonds are thus typical metallic bonds. In addition, the Al–RE bond length has a broad distribution, which is in contrast to the uniform bond length of Al–LTM pairs.

Several authors took a different approach and used *ab initio* MD to simulate the structure of Al-rich MGs. For example, Jakse et al. [245] simulated  $\text{Al}_{80}\text{Mn}_{20}$  and  $\text{Al}_{80}\text{Ni}_{20}$  liquids and found pronounced chemical SRO. In a more systematic study by Sheng et al. [93], the partial PDFs obtained in *ab initio* MD simulations were used to generate a larger system, employing the inverse Monte Carlo (IMC) method (note that IMC is different from the RMC discussed earlier, and details can be found in Ref. [246]). The larger system has the same partial PDFs as the ones in *ab initio* simulation, but imparting much smaller fluctuation and much higher resolution, which facilitates direct extraction of the structure factor to compare with experiments. Sheng et al. found that the basic principles for atomic packing in LTM–NM MGs, as discussed in the preceding sections, also apply in the Al-rich MGs. That is, the solute atoms (LTM, RE) are surrounded by the solvent atom Al, and the CN is determined by the effective size ratio. The solute-centered clusters are then efficiently packed in the 3-D space by sharing solvent atoms, constituting the MRO (Fig. 21). Note that in the *ab initio* simulations, the Al–LTM bond shortening is also observed. The CN, as obtained using the Voronoi method, is  $\sim 9$  for LTM (Fe, Co, Ni) [93]. This CN, while consistent with the efficient packing model based on the effective (i.e., with shortening of the bond length considered) size ratio, is larger than the value (6–7) derived from some experiments (see preceding paragraph). This suggests that the LTM-centered Al–LTM clusters may also entail dense packing, rather than the open environment (low CN) previously reported. The CN around RE (Y, La, Ce, Nd, Gd) is  $\sim 17$  in simulation, close to the experimental results.

The above structure picture leads to the speculation that for Al-rich Al–RE–LTM ternary MGs, an optimal composition for glass formation should allow each and every Al atom to be shared by both a LTM-centered cluster and a RE-centered cluster. This way, all Al atoms are energetically stabilized and all clusters are efficiently packed and connected. Such a composition can be located by the cluster

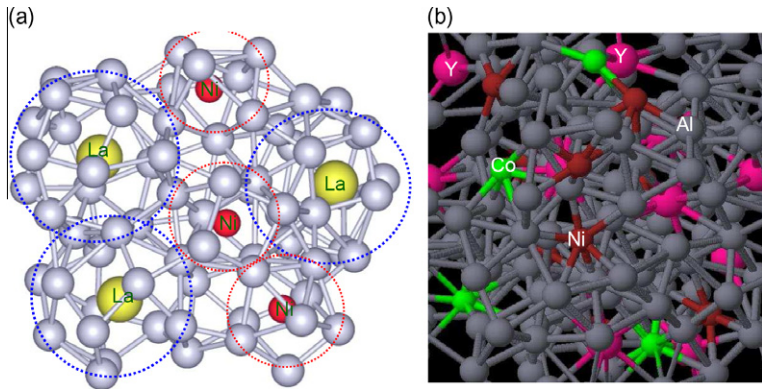


**Fig. 21.** Structure model for Al-rich MGs: dense packing of solute (LTM, RE) centered clusters. (Reproduced from [93] with permission © 2008 by Elsevier.)

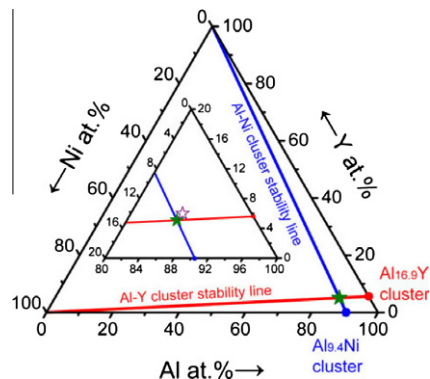


**Fig. 22.** Application of cluster line method in designing Al-rich BMGs. (Reproduced from [232] with permission © 2009 by Elsevier.)

line method as shown in Fig. 22, which was found helpful in the search for the first Al-rich BMG with Al composition greater than 50% [232,233]. Earlier cluster line models can be found in the work of Dong et al. [247,248].

### 3.3.2. Origin of the prepeak

The measured XRD or neutron diffraction spectra of Al-rich MGs usually have an obvious prepeak; an example is given in Fig. 23. The prepeak in the reciprocal space should correspond to certain medium-range correlations in real space. Hsieh et al. [237] examined the prepeak in terms of the sublattice formed by the solutes (Fe and Ce in Al-Fe-Ce). It was found that although the distribution of Ce is relatively random, ordering in the Fe sublattice does exist, which could be the main reason for the prepeak. Similarly, Ahn et al. [249] studied an Al-Ni-Nd MG, and noticed that Ni has much more significant contribution to the prepeak than Nd. Saskl et al. [241,242] emphasized instead the general medium-range correlation in the sublattice formed by both LTM and RE atoms. They found that the LTM-LTM, LTM-RE, and RE-RE correlations may all contribute to the prepeak; which one actually dominates is system dependent, and also related to the technique used (XRD or neutron diffraction).

Based on the experimental observations, it seems that two conditions are favorable for strong prepeaks: (1) solute-lean composition and cluster packing structure, with isolated solute atoms

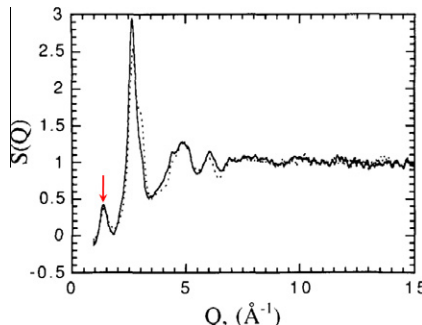


**Fig. 23.** The prepeak (marked by red arrow) in the structure factor of an Al-rich MG. (Reproduced [237] from with permission © 1991 by Elsevier.)

forming a sublattice-like pattern and (2) solute is the strong scatterer with significantly higher atomic scattering amplitude than the solvent. The first condition (i.e., well-separated solutes forming a sublattice) results in a strong low- $q$  peak in the solute–solute partial structure factor, while the second condition (strongly scattering solutes) gives the solute–solute partial a sufficiently large weighting factor (Eq. (4)), for the low- $q$  peak to be observed as a prepeak in the total structure factor. Interestingly, Al-rich MGs satisfy both, while some other commonly known MGs do not. For example, the LTM–NM MGs meet the first condition, but the solvent (LTM) is the strong scatterer, thus prepeak in LTM–NM MGs is usually not observed. In addition to Al-rich MGs, there are also non-Al-based MGs satisfying the two conditions and showing strong prepeaks, such as Zr<sub>73</sub>Pt<sub>27</sub> [250] and Zr<sub>70</sub>Cu<sub>29</sub>Pd<sub>1</sub> [251]. The solute (Pt or Pd) atoms in these MGs have much higher scattering factor than Zr and Cu.

This line of reasoning is better illustrated in Fig. 24, using a model Pd<sub>82</sub>Si<sub>18</sub> obtained by MD simulation (EAM potential provided by Dr. H.W. Sheng). The system is solute-lean with a formula (Solvent)<sub>82</sub>(Solute)<sub>18</sub>, and there is obvious solute–solute avoidance, as evidenced by the partial PDFs. As a result, the solute–solute partial PDF yields a large low- $q$  peak in its partial structure factor. If we use the scattering factors of Pd and Si for the solvent and solute, respectively (Pd is a much stronger scatterer than Si), the solute–solute partial has too small a weighting factor to be detected in the total structure factor, and no prepeak is observed. However, if we assume Zr to be the solvent and Pt to be the solute to mimic Zr–Pt, and use the corresponding scattering factors to re-calculate the total structure factor, a strong prepeak appears. Note that the MD sample used here is in fact an equilibrium liquid (at 1300 K), which demonstrates that chemical SRO persists even in liquid, and as long as there is strong chemical order and solute–solute correlation, prepeak can be observed when the solute is a much stronger scatterer than the solvent both in MGs and in liquids [252,253].

Note that the two conditions proposed above seem to be sufficient but not necessary. They highlight a desirable scenario to observe strong prepeaks, but observable prepeaks may exist even when the two conditions are not fully satisfied (e.g., in the concentrated Ce<sub>55</sub>Al<sub>45</sub> glass [254]).

### 3.3.3. Comparison with LTM–NM metallic glasses

It would be interesting to compare the Al-rich MGs with the LTM–NM MGs discussed in the earlier sub-section. They appear to have similar structure (quasi-equivalent solute-centered clusters and efficient packing of these clusters), but very different GFA. Specifically, many LTM–NM based multicomponent MGs can be made 10 mm or above in size, while only a couple of Al-based multicomponent MGs have barely reached the BMG criterion (1 mm in the thinnest dimension) very recently [231–233]. The origin may lie in the very different phase diagram features of Al–LTM/RE and LTM–NM systems. A typical LTM–NM binary phase diagram usually has a deep eutectic [212], i.e., when LTM is alloyed with NM, the melting temperature decreases precipitously. In contrast, the melting temperature of Al increases significantly when alloyed with LTM/RE to beyond a few atomic percent. These diagrams show that Al-rich alloys have much more competitive crystalline compounds than LTM–NM

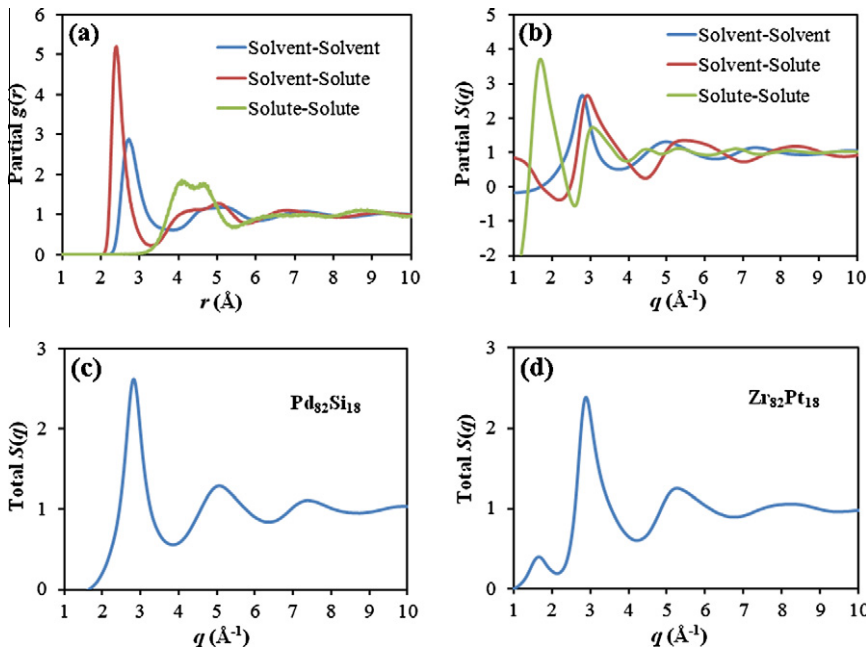


**Fig. 24.** (a) Partial PDFs and (b) partial structure factors of the binary (Solvent)<sub>82</sub>(Solute)<sub>18</sub> model metallic liquid. Total structure factors calculated from the partials in (b), using the atomic scattering factors for (c)  $\text{Pd}_{82}\text{Si}_{18}$  and (d)  $\text{Zr}_{82}\text{Pt}_{18}$ , respectively.

alloys have. In other words, the dramatically different GFA of the two types of MGs is probably not because the amorphous structures are very different, but mainly because the competing crystals are different, in terms of their *relative* stability.

### 3.3.4. Structure of RE-rich metallic glasses and polyamorphism

The structure of RE-rich MGs has not been systematically studied. Nevertheless, an interesting observation is the polyamorphism found in some Ce-based MGs. Sheng et al. [254], by using *in situ* XRD, first reported an amorphous-to-amorphous phase transition in  $\text{Ce}_{55}\text{Al}_{45}$  MG under hydrostatic pressure. A major feature of this transition is the significant increase of density with compression, and a hysteresis loop in the loading-unloading volume-pressure plot. Similar observations were reported by Zeng et al. [255], in a La-Ce-Al MG. The origin of this polyamorphic transition is the delocalization of 4f electrons in Ce, which has been confirmed by *ab initio* simulations of the  $\text{Ce}_{55}\text{Al}_{45}$  MG [254] and recently by X-ray absorption experiments in a  $\text{Ce}_{75}\text{Al}_{25}$  MG [256]. Due to the delocalization, some Ce–Ce pairs can form shorter bonds than those between the Ce atoms with localized 4f electrons, as shown in Fig. 25. The shortened Ce–Ce bonds and the double-shell structure of Ce–Ce partial PDF at high pressures are thus the structural origin for the anomalous density increase that distinguishes the two polyamorphs.

In contrast, another RE-rich MG ( $\text{La}_{75}\text{Al}_{25}$ ) does not exhibit unusual pressure effect in a similar experiment: the compression is reversible with no hysteresis loop, and the equation of state can be nicely fitted with the Murnaghan equation [257]. At atomic level, the structure can be described as Al-centered cluster with La and Al (mostly La) in the shell. It is found that the CN around Al can be tuned by pressure, increasing from 9 (prism-like) to 12 (icosahedron-like) when the hydrostatic pressure changes from 0 GPa to 40 GPa. The cause of the CN change was ascribed to the different compressibility of La (softer) and Al (harder) elements, which leads to the change of effective atomic size ratio between solute (Al) and solvent (La).

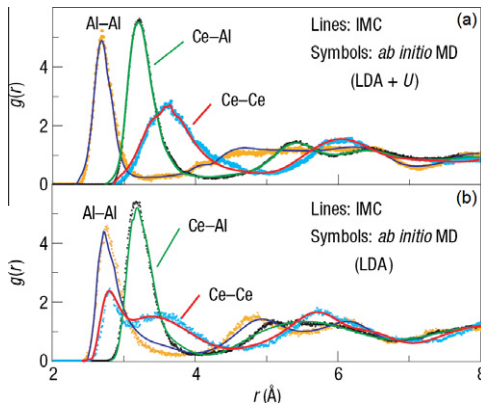


**Fig. 25.** Polyamorphism in a Ce<sub>55</sub>Al<sub>45</sub> MG. Partial PDFs of (a) low pressure phase with localized Ce 4f electron and (b) high pressure phase with delocalized Ce 4f electron. (Reproduced from [254] with permission © 2007 by Nature Publishing Group.)

### 3.4. Structure of ETM–LTM metallic glasses

This is arguably the most popular MG category, as many ETM–LTM-based compositions can be made into BMGs of relatively large sizes, with interesting properties that are currently being studied worldwide. For example, a group of BMGs that is being intensively investigated for mechanical properties can be represented by (Zr,Hf,Ti,Ta,Nb)–(Cu,Ni,Ag)–(Al)–(Be). However, in terms of glass structure it is not obvious what characteristics the ETM–LTM MGs would have, because different from the LTM–NM and the Al-rich types, the composition of ETM–LTM MGs is no longer solute-lean and in fact often resides in the middle concentration range of the phase diagram. The description of quasi-equivalent clusters must be modified and extended, as will be illustrated in the following.

#### 3.4.1. Structure of Cu–Zr binary metallic glasses

Cu–Zr as a binary BMG former [258–260] has recently received much attention. It has good GFA over a wide composition range (from Cu<sub>30</sub>Zr<sub>70</sub> to Cu<sub>70</sub>Zr<sub>30</sub>), and it is the prototype for many important BMGs in this ETM–LTM category, from binary Ni–Zr, Ni–Nb, Cu–Hf, to multicomponent Zr–Cu–Ni–Al, etc. Moreover, the related MGs are usually concentrated alloys, making it inappropriate to differentiate the solute and solvent. This makes the “solute-centered cluster surrounded by solvent only” model discussed in the previous sections no longer applicable. For the above reasons, understanding the structure of Cu–Zr at different compositions is not only important but also challenging.

First of all, since Cu and Zr have different atomic size and thus different molar volume, it would be interesting to find out whether the mass/atomic density of Cu–Zr MGs formed over the wide composition range follows the rule of mixtures, i.e., a linear interpolation of those of pure Cu and Zr. The density of Cu–Zr MGs has been measured in different experiments [261–266], and the results are summarized in Fig. 26. Despite the systematic discrepancies between data sets from different groups, it appears that the density roughly falls on a straight line close (parallel) to the interpolation of fcc Cu and hcp Zr density. However, a recent experiment by Li et al. [267] used a novel technique to measure the density, and the results cast doubt on previous conclusions. They associated the bending of a cantilever (deposited with Cu–Zr MG on one side) during crystallization with the density difference between the glass and the crystallized compounds. By assuming known densities of the crystalline products, the glass density can be derived. The ingenious part of the experiment is that the composition deposited on a row of cantilevers can be tuned almost continuously from Zr-rich to Cu-rich, and the difference in the bending angle upon crystallization can be directly compared in a single annealing experiment. Due to the high resolution and fine composition interval in this experiment, the authors were able to detect the subtle deviation of the density from the linear interpolation. Specifically, they found three density peaks which nicely correspond to the three compositions with the best GFA in the

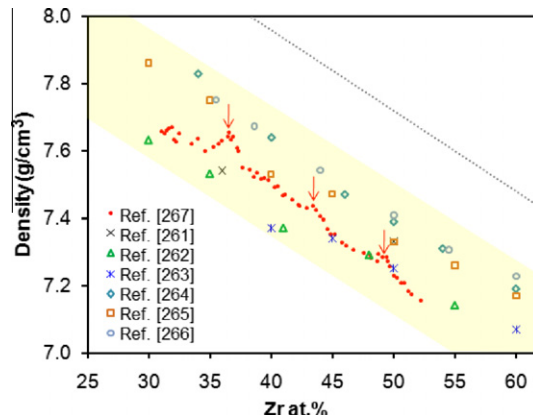


**Fig. 26.** Density of Cu–Zr MGs as a function of Zr at.%. Results by Li et al. [267] (red solid circles) are compared with data measured previously using traditional methods. Dotted line is the interpolation of the density of fcc Cu and hcp Zr at room temperature.

Cu–Zr system (arrows in Fig. 26). This very interesting behavior was not noticed before, presumably due to the relatively sparse data points and lack of systematic study under consistent experimental conditions. The three density peaks would suggest special atomic-level structures at these three particular compositions, implying that the BMGs formed at these compositions are almost intermetallic-like. However, although the method designed by Li et al. has obvious advantages, it is an indirect measurement of the density. During annealing, the Cu–Zr MGs become supercooled liquids when the temperature is above  $T_g$ . Crystallization then sets in when the crystallization temperature ( $T_x$ ) is reached. One important and implicit assumption behind their interpretations of the results is that the viscous flow (inelastic deformation) of the supercooled liquids during bending, before crystallization is completed, does not significantly reduce the final bending angles, or it causes the same small reduction for all compositions. However, since the GFA is different for different compositions, the stability of the supercooled liquids is also different. It is possible that the liquids at the three best GFA compositions can survive for a longer time during crystallization and bending, such that the inelastic relaxation canceled a larger fraction of the bending angle. If this were to happen, the smaller final bending angle may be due to either the larger glass density, or the better GFA (the higher stability of supercooled liquids) at these compositions, or a mixed effect of both. Complementary experiments such as hardness measurement on these thin film samples may be useful in confirming the density peaks. Also, to obtain accurate density values using this method, one need to make sure that the MGs are fully crystallized at all compositions with similar grain sizes and stresses in the film, and the subsequent coarsening and relaxation in the intermetallic grains make no difference to the bending (or affect the bending in a similar way for all compositions).

The composition dependence of the Cu–Zr MG structures can be further investigated through an examination of the PDFs and CNs, as well as the chemical SRO characterized by the partial CNs. Mattern et al. [265] and Ma et al. [268] used XRD and neutron diffraction to examine the SRO in Cu–Zr, and solved the partial CNs by decomposing the first peak in the total PDF. Although the extracted partial CNs in different experiments are somewhat different [265,268], the overall trend of the composition dependence is consistent. Similar trend is also reproduced in MD-simulated Cu–Zr [269], as shown in Fig. 27. In addition, Cu–Cu, Cu–Zr, and Zr–Zr bond lengths solved from XRD data are almost equal to the sum of metallic radii, suggesting pure metallic bonding. Ma et al. [268] further studied the chemical SRO and packing efficiency around Cu and Zr atoms. They found that around Cu, the unlike (Cu–Zr) bonds are favored, while around Zr, the fraction of Zr–Zr bonds is higher than expected from the global composition. Moreover, the packing around Cu nearly achieved the highest possible packing efficiency with the given partial CNs, while the packing around Zr is less efficient. These results suggest that the Cu–Zr structure can be better understood from the perspective of

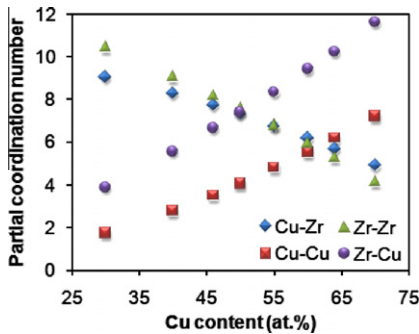


Fig. 27. Partial CNs of MD-simulated Cu–Zr MGs as a function of Cu content [269].

Cu-centered clusters, as also supported by computer simulations and local symmetry analysis (see discussion below). Note that in the composition range of Fig. 27, the center Cu/Zr atoms in the clusters are surrounded by both Cu and Zr atoms in the shell, which is different from the P-centered clusters in Ni<sub>80</sub>P<sub>20</sub>, where P atoms are surrounded by Ni only.

Additional information regarding the local symmetry in Cu–Zr MGs can be obtained by conducting a Voronoi analysis, which has been done by several groups using configurations obtained in MD simulations or RMC fitting to experiments [63,135,269–275]. The results are in general consistent despite some quantitative differences. Figs. 28 and 29 show the results by Cheng et al. [269,270]. Here each sample contains 10,000 atoms, and all samples were made using MD simulation employing EAM potentials, in an *NPT* ensemble at cooling rate 10<sup>11</sup> K/s (unless explicitly indicated otherwise). From the Voronoi indices, it can be seen that the five-edged faces are dominant in Cu–Zr. From Zr-rich to Cu-rich, with the CN changing gradually, the dominant Voronoi polyhedra also change. It has been found to be instructive to examine the Cu-centered clusters. The packing around Cu seems rather regular: for each CN, there are only a few dominant cluster types, and their total fraction approaches 80% of all Cu atoms, as shown in Fig. 28. Among the various polyhedra around Cu, the Cu-centered full icosahedra with Voronoi index <0,0,12,0> appear special, because the increase of their fraction with increasing Cu is much more dramatic than others. On the Zr-rich side, the fraction of Cu-centered <0,0,12,0> is very small, and a major fraction of Cu atoms are in clusters with lower CNs (10 or 11),

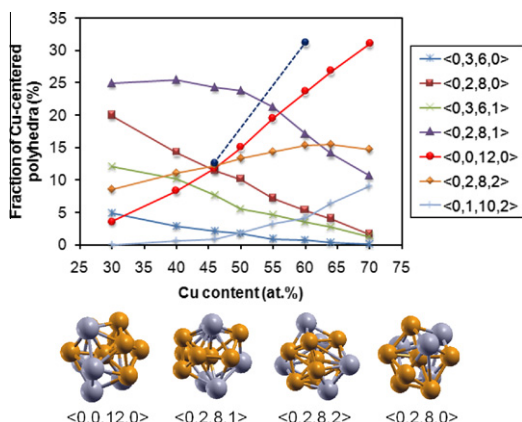


Fig. 28. Fractions of Voronoi cells around Cu in MD-simulated Cu–Zr MGs, as a function of composition. Blue full circles and dashed line mark the fractions of <0,0,12,0> in MG samples made at cooling rate one order of magnitude slower than other samples. Several representative Cu-centered clusters are shown in the lower panel (orange balls for Cu and gray balls for Zr).

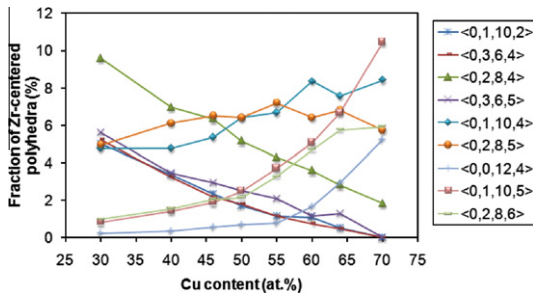


Fig. 29. Fractions of Voronoi cells around Zr in simulated Cu–Zr MGs.

such as  $\langle 0,2,8,0 \rangle$  and  $\langle 0,2,8,1 \rangle$ . With increasing Cu content, the average CN around Cu increases towards 12 (due to the changing effective size ratio between the shell atoms and the center atom), and the  $\langle 0,0,12,0 \rangle$  clusters quickly become dominant. This implies a dramatic increase of the fivefold bond and the degree of icosahedral order. Moreover, the fraction of  $\langle 0,0,12,0 \rangle$  is more sensitive to the cooling rate (used in MD simulation) compared to other clusters, especially on the Cu-rich side. When the MD quenching rate was reduced by one order of magnitude (to  $10^{10}$  K/s), the trend is even more dramatic, see Fig. 28. In experiments where the cooling rate is orders of magnitude lower, it is expected that the  $\langle 0,0,12,0 \rangle$  clusters are more abundant for Cu-rich MGs, and its increase with Cu composition would also be steeper. In contrast, the behavior of the Zr environment is relatively featureless. Fig. 29 shows the most populous types of Zr-centered clusters. First of all, the distribution of cluster types is rather broad, and they all have fractions less than 10% for the entire composition range. The sum of these fractions is much smaller than 50%, which means there are a lot more other types with even lower fractions (not shown in Fig. 29). In other words, there is no obviously dominant type for Zr-centered clusters. Second, the composition dependence is not very strong for most cluster types, and their population shows mostly a gradual and systematic shift with the changing CN. Therefore, Cu-centered clusters appear to be the efficiently packed characteristic structural unit in Cu–Zr, with well-defined topological SRO. This finding in MD simulation is consistent with the experimental observations by Ma et al. [268], and also justifies the approach to examine the Cu–Zr MGs structure from the perspective of Cu-centered clusters. The important role of Cu-centered clusters in controlling properties will be further examined in Section 3.7.1. (which also underscores the usefulness of analyzing the structure of these MGs from the vantage point of the Cu-centered clusters). Note that the above structural features are mainly about the arrangement of atoms in the nearest-neighbor shell, and its variation does not necessarily affect the density and CN. For example, the pronounced changes in the fraction of Cu-centered  $\langle 0,0,12,0 \rangle$  clusters do not contradict with the trend of density and partial CNs in Figs. 26 and 27.

Very recently, Li et al. [135] studied the medium-range correlation of different Voronoi cells, and found that the distribution of  $\langle 0,0,12,0 \rangle$  clusters in Cu–Zr is not completely random. Instead, they tend to aggregate and connect with each other, forming chains and networks. This finding, together with the above results, suggest that although the density of Cu–Zr behaves like an ideal homogeneous solution of Cu and Zr, the degree of fivefold symmetry and icosahedral order, i.e., the fraction (and connectivity) of the  $\langle 0,0,12,0 \rangle$  clusters, exhibits unusual behaviors, in terms of the cooling rate and composition dependence, as well as the trend to form MRO. Further studies have in fact shown that they indeed play a special role in controlling the formation and properties of this MG (see Section 4).

Other simulations and experiments on the structure of Ni–Zr [276,277], Ni–Ti [278,279], Ni–Nb [280,281], Cu–Ti [282], Cu–Hf [283], Zr–Pd [284] Zr–Pt [285] MGs have demonstrated that they share structural features similar to those in the Cu–Zr MGs. Specifically, on the LTM-rich side, icosahedral order with CN  $\sim 12$  is found to be pronounced; on the ETM-rich side, however, LTM-centered BSAP with CN = 10 and TTP with CN = 9 may have larger fractions. Direct evidence for the latter case has been found in a recent experiment using nanobeam electron diffraction under TEM [119], where a Zr<sub>66.7</sub>Ni<sub>33.3</sub> (ETM-rich) MG was studied, and  $\langle 0,2,8,0 \rangle$ ,  $\langle 0,3,6,1 \rangle$  and  $\langle 0,2,8,1 \rangle$  clusters have been

identified. The similarity of structure in ETM–LTM MGs in terms of both the dominating cluster types and their composition dependence is in fact expected, because these ETM–LTM pairs (e.g., Zr–Cu, Ti–Ni, Hf–Cu) are similar in both the atomic size ratio and the chemical affinity. It should be noted that while the structures of these MGs share certain features and the trend of composition dependence, they are nevertheless not identical, as suggested by a comparative study of Ni–Zr and Cu–Zr at the same Zr content [286,287].

### 3.4.2. Structure of Cu–Zr–Al metallic glasses

By alloying Cu–Zr with a few percent of Al, the GFA of the MG can be significantly enhanced, and the properties are also obviously modified. It is thus intriguing to understand how the local structure of Cu–Zr is changed by alloying with Al.

A recent study by Cheng et al. [163] shows that the addition of Al greatly increases the fraction of  $\langle 0,0,12,0 \rangle$  coordination polyhedra around both Cu and Al, and thus enhances the overall fivefold topology and icosahedral order, see Figs. 30 and 31. The 3-D structures constructed for the ternary MG, in comparison with that of the base binary, is shown in Fig. 30, which also includes a comparison of the interconnection of icosahedra to form MRO (in the form of icosahedra patches and chains). Further studies employing *ab initio* calculations have revealed the twofold origin of the effect of Al. First, due to the electron orbital hybridization between Al (*sp*) and Cu (*d*), in this Al-lean environment, the Al–Cu bond is ~5% shorter than the sum of their metallic radii. As seen in Fig. 32, the charge density distribution around the Cu-surrounded Al exhibits some degree of polarization, in contrast to the spherical distribution around Cu with Zr as neighbors. As a result, Al has an environment-specific effective size: it appears smaller in bonding with Cu, but exhibits the normal size with respect to

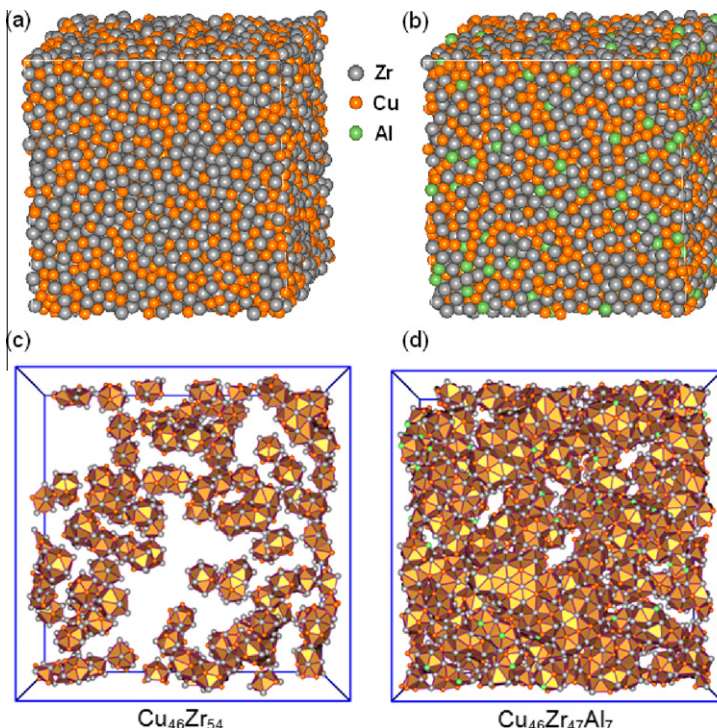


**Fig. 30.** 3-D configurations of the (a)  $\text{Cu}_{46}\text{Zr}_{54}$  and (b)  $\text{Cu}_{46}\text{Zr}_{47}\text{Al}_7$  MG samples obtained in MD simulation. The population and degree of connectivity of the  $\langle 0,0,12,0 \rangle$  icosahedra are obviously higher in (d)  $\text{Cu}_{46}\text{Zr}_{47}\text{Al}_7$  than in (c)  $\text{Cu}_{46}\text{Zr}_{54}$ . For clarity, only the top half of the simulation box is shown in (c) and (d). (Reproduced from [163] with permission © 2009 by American Physical Society.)

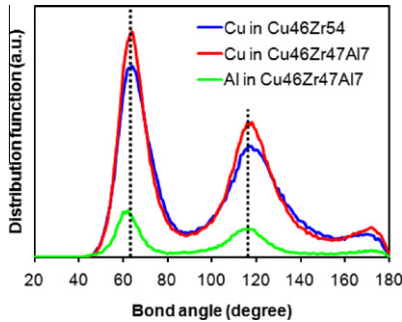


**Fig. 31.** Bond angle distribution in Cu<sub>46</sub>Zr<sub>47</sub> (around Cu) and Cu<sub>46</sub>Zr<sub>47</sub>Al<sub>7</sub> (around Cu and Al) in MGs. Bond angles of perfect icosahedron are labeled by dotted lines. Addition of 7 at.% of Al significantly improves the fivefold symmetry and icosahedral order.

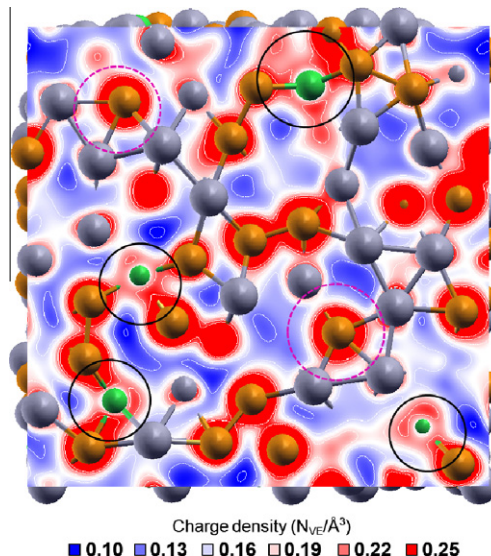


**Fig. 32.** Charge density distribution in Cu<sub>46</sub>Zr<sub>47</sub>Al<sub>7</sub>. Black circles highlight unusual charge distribution for Cu–Al bonds due to electron orbital hybridization, compared with the more hard-sphere-like Cu–Zr bonds (dashed pink circles) [163].

Zr. Second, the above chemical effect and the shortened Al–Cu bond topologically favors both Cu-centered and Al-centered (0,0,12,0), and the chemical affinity renders the icosahedral clusters more stable. As such, chemistry and topology work in concert, effectively enhancing the fivefold atomic arrangement and lowering its energy. Some of the above results are corroborated by recent experiment by Georgarakis et al. [288], and *ab initio* simulation by Lekka and Evangelakis [289].

### 3.4.3. Structure of Cu–Zr–Ag metallic glasses

Similar to Al, alloying with Ag also has significant effects on the GFA and properties of Cu–Zr. However, the underlying origin is different. Unlike Al, Ag and Cu are both LTMs, and they are known to have positive heat of mixing (immiscible in equilibrium at low temperatures). Therefore, Ag and Cu in Cu–Zr–Ag MGs are likely to repel each other to some extent, and create chemical heterogeneities. This is confirmed in a recent study by Fujita et al. [290]. Using *ab initio* simulation, they found Ag–Ag pairs and rings in a Cu–Zr–Ag MG (Fig. 33), and Cu and Ag atoms are surrounded by icosahedral

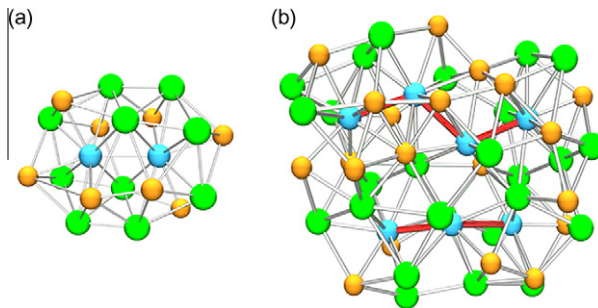


**Fig. 33.** (a) An interpenetrating cluster with paired Ag atoms in the center (b) a large interpenetrating clusters centered by stringed Ag atoms. The red line denotes Ag–Ag contacts, and the bronze, green, and light blue balls represent Cu, Zr, and Ag atoms, respectively. (Reproduced from [290] with permission © 2009 by American Physical Society.)

clusters. Here Ag atoms do not scatter in the Cu–Zr matrix like Al in Cu–Zr–Al; instead, they aggregate to reduce the chance to bond with Cu. Such a local structural feature can successfully reproduce the EXAFS measured in experiments. MD simulations by Kang et al. [291] also lead to similar results and conclusions.

#### 3.4.4. Structure of $(\text{Ti}, \text{Zr}, \text{Nb}, \text{Hf}, \text{Ta}) - (\text{Ni}, \text{Cu}, \text{Pd}, \text{Ag}) - (\text{Al}) - (\text{Be})$ metallic glasses

We now consider the more general cases in this ETM–LTM category, which can be represented as  $(\text{Ti}, \text{Zr}, \text{Nb}, \text{Hf}, \text{Ta}) - (\text{Ni}, \text{Cu}, \text{Pd}, \text{Ag}) - (\text{Al}) - (\text{Be})$ . In addition to Al, Be is also found to be very effective in improving the GFA of ETM–LTM-based BMGs. For example, the Be-bearing Vitreloy series [292] have outstanding GFA, and due to their high stability, they are also excellent prototypical systems for studying the properties of supercooled liquids and glass transition [25]. The element Be has the smallest atomic size in all metals; the hcp Be has an anomalous Poisson's ratio ( $\sim 0.05$ ), which is almost one order of magnitude lower than other (hcp) metals, suggesting unusual bonding associated with Be. Presumably, these very special geometrical and chemical characters lead to its unique role as an alloying element in the stabilization of ETM–LTM supercooled liquids and BMG formation.

Unfortunately, it is extremely difficult to solve the atomic structure of the above multicomponent systems containing more than three elements. The complexity arises from not only the number of elements itself, but also the complicated chemical affinity between element pairs and the increasing possibility of chemical heterogeneity. In other words, the structure and bonding would have large variations at atomic-level or sub-nanometer scale. There have been both experimental and computational studies on multicomponent BMGs. Due to the limited element-specific resolution, most experiments can only solve the average profile of the structure (average CN, bond length, etc.), while most simulations, having to use *ab initio* method (empirical potential for multicomponent system is rarely available), are severely limited by the time-scale and length-scale involved in the computer world, and may not reproduce the true structure of the laboratory BMGs.

Ma et al. [293], by grouping the atoms according to their atomic sizes, approximated the  $\text{Zr}_{52.5}\text{Ti}_5\text{Cu}_{17.9}\text{Ni}_{14.6}\text{Al}_{10}$  BMG as pseudoternary  $(\text{Zr}) - (\text{Al}, \text{Ti}) - (\text{Cu}, \text{Ni})$  (i.e.,  $\text{Zr}-\alpha - \beta$ ), and studied the structure using XRD and neutron diffraction. The first peak in the total PDF was fitted using the non-negligible sub-peaks due to  $\text{Zr}-\text{Zr}$ ,  $\text{Zr}-\alpha$ ,  $\text{Zr}-\beta$ , and  $\beta - \beta$  pairs, for both XRD and neutron data. It was found that the solutes ( $\alpha$  or  $\beta$ , i.e., Ti, Cu, Ni, Al) tend to avoid each other, and form clusters with Zr (the solvent) in the shell. This resembles the cluster packing scenario proposed for LTM–NM and Al-rich MGs. However, since the total solute composition is close to 50 at.%, complete avoidance of solute is not possible, and the structure may be better pictured as interpenetrating solute-centered clusters.

Hufnagel and Brennan [294] studied the effect of minor Ta addition in the  $\text{Zr}-\text{Cu}-\text{Ni}-\text{Al}$  BMGs, i.e.,  $(\text{Zr}_{70}\text{Cu}_{20}\text{Ni}_{10})_{90}\text{Al}_{10}$  versus  $(\text{Zr}_{70}\text{Cu}_{20}\text{Ni}_{10})_{86}\text{Ta}_4\text{Al}_{10}$ . The shift of the first peak in the total PDF indicates that the Ta is strongly coordinated with Ni and/or Cu, but the average CN is unchanged. By comparing the Zr differential PDFs measured using anomalous XRD. They found that 4% Ta has little effect on the nearest-neighbor shell of Zr. However, it did significantly enhance the MRO, as demonstrated by the

**Table 3**

Heat of mixing (kJ/mol) as predicted by Miedema's model. The metallic radii ( $\text{\AA}$ ) of these elements are given in the X-X cells [295].

	Ti	Zr	Nb	Hf	Ta	Ni	Cu	Pd	Ag	Al	Be
Ti	1.46	0	2	0	1	-35	-9	-65	-2	-30	-30
Zr	0	1.49	4	0	3	-49	-23	-91	-20	-44	-43
Nb	2	4	1.46	4	0	-30	3	-53	16	-18	-25
Hf	0	0	4	1.67	3	-42	-17	-80	-13	-39	-37
Ta	1	3	0	3	1.58	-29	2	-52	15	-19	-24
Ni	-35	-49	-30	-42	-29	1.28	4	0	15	-22	-4
Cu	-9	-23	3	-17	2	4	1.27	-14	2	-1	0
Pd	-65	-91	-53	-80	-52	0	-14	1.41	-7	-46	-8
Ag	-2	-20	16	-13	15	15	2	-7	1.42	-4	6
Al	-30	-44	-18	-39	-19	-22	-1	-46	-4	1.43	0
Be	-30	-43	-25	-37	-24	-4	0	-8	6	0	1.13

splitting of the second-nearest-neighbor shell in the Zr differential PDF. Based on the observations, it was proposed that Ta helps to improve the efficiency of cluster packing. Here the clusters, considering the results by Ma et al. [293], are presumably solute- (Cu-, Ni-, or Al-) centered with Zr atoms shared in the shell. The Ta atoms, which are slightly smaller than Zr, may join the shells and adjust the connection of the solutes (Cu, Ni, Al), making the overall sharing schemes more efficient.

Although more systematic studies are still desirable, some general principles can already be discussed. The values of heat of mixing and atomic sizes of related elements in this category are summarized in Table 3. It is clearly seen that the heat of mixing between elements within ETM (or LTM) group is mostly positive, while the heat of mixing between ETM and LTM elements is mostly negative; Al and Be have negative heat of mixing with almost all others. Similar to our previous discussion for multi-component LTM–NM MGs, one or more ETM/LTM elements with positive heat of mixing are likely to induce (nanoscale) chemical heterogeneity, as demonstrated by the Cu–Zr–Ag example. In addition, the atomic size ratio and the relative composition between ETM and LTM determine the dominant SRO. In terms of the LTM-centered cluster, the LTM-rich BMGs are likely to contain more  $\langle 0, 0, 12, 0 \rangle$  icosahedra, while the ETM-rich BMGs may have more clusters with CN < 12, such as the  $\langle 0, 2, 8, 1 \rangle$  and  $\langle 0, 2, 8, 0 \rangle$  clusters. For some very Zr-rich MGs (e.g., Zr<sub>80</sub>Pt<sub>20</sub> [152]), solute avoidance may occur, which resembles the LTM–NM or Al-rich MGs.

It should be noted that the numbers quoted in Table 3, including the heat of mixing obtained by Miedema's model and the tabulated atomic radii, are only semi-empirical estimates. To obtain the accurate values in a particular system, experiments or *ab initio* calculations are required. For example, the quoted Al–Cu heat of mixing in Table 3 underestimates the true value in Cu–Zr–Al primarily due to the unusual bond shortening and composition-dependent electronic structure, which are not accounted for in the empirical model. As a specific example, the formation enthalpy of CuAl (I2/m) in experiment and *ab initio* calculation is around -20 kJ/mol [163], much more negative than the predicted heat of mixing in Table 3.

### 3.5. Structure of AM–LTM metallic glasses

MGs in this category have unique and appealing properties. For example, the biodegradable Mg–Ca–Zn BMG has been recently suggested for biomedical applications [296]. However, the structure of these MGs has not been systematically studied. A few examples will be given below, and the possible structural features will be discussed.

Bailey et al. [297] studied the structure of Mg–Cu MG using MD simulation, and found a large fraction of fivefold bonds in the simulated sample. The average CN around Cu (and Mg) is composition dependent, changing from less than 10 to above 12 with increasing Cu content. On Cu-rich side where the CN is close to 12, the predominant fivefold bonds would indicate Cu-centered icosahedral SRO. This is similar to the Cu–Zr case. Jovari et al. [298] studied the structure of Mg<sub>60</sub>Cu<sub>30</sub>Y<sub>10</sub> using EXAFS. In addition to the prevalence of fivefold bonds, local structures very similar to the Mg<sub>2</sub>Cu (Laves phase)

and  $\text{YCu}_2$  crystals were found as well. The Mg–Cu and Cu–Y bonds are noticeably shorter than the sum of metallic radii, and the CNs around Mg and Cu are close to 12. Hui et al. [299] studied  $\text{Mg}_{65}\text{Cu}_{25}\text{Y}_{10}$  using *ab initio* MD simulation. Cu- and Mg-centered icosahedral clusters were also identified, corroborating the experimental observations. Similar packing structure was noticed in earlier simulations by Qi and Wang [300] in a model  $\text{Ca}_7\text{Mg}_3$  MG.

Very recently, Senkov et al. [301] studied the structure of  $\text{Ca}_{60}\text{Mg}_x\text{Zn}_{40-x}$  BMGs ( $x = 10, 15, 20, 30$ ). It was found that the Mg- and Zn-centered clusters with primarily solvent Ca in the nearest-neighbor shell are the basic building blocks. The average CN around Mg is  $\sim 11$ , with the most dominant Voronoi polyhedron being  $\langle 0, 2, 8, 1 \rangle$ , while the average CN around Zn is 9–10, having large fraction of  $\langle 0, 3, 6, 0 \rangle$  and  $\langle 0, 2, 8, 0 \rangle$  clusters. Ca atoms have average CN of 13. *Ab initio* simulations found similar CN values (11 for Mg, 9 for Zn, 13 for Ca). Apparently, the  $\langle 0, 0, 12, 0 \rangle$  full icosahedra do not dominate in these MGs, although fivefold bonds in the form of pentagonal bipyramids constitute the most populous structural unit.

From these limited examples, it appears the fivefold bond is also typical in AM–LTM MGs, and icosahedral order is prominent in some alloys and at certain compositions. However, since the atoms involved in this group cover a wider range of atomic sizes than the ETM–LTM MGs (AMs such as Ca and Mg have sizes considerably larger than ETM), it is expected that the atomic-level structure may have more significant composition dependence. At low AM composition, icosahedral order is more likely to dominate, while at high AM contents the solute-centered clusters tend towards BSAP and TTP types.

### 3.6. Icosahedral order: metallic glasses and quasicrystals

As noted by Steinhardt, “somewhere between the amorphous glasses and the rigidly regimented periodic crystals lie the quasicrystals: ordered, predictable, yet non-periodic arrangements of atoms” [302]. Since the discovery of the first quasicrystal [303], its structure has been intensively studied. Fivefold rotational symmetry, which is incompatible with the translational symmetry in conventional crystals, is characteristic of the quasicrystals. The structural units, including those with fivefold symmetry (e.g., icosahedral clusters), are arranged in a predictable but non-periodic way: one may find an axis of rotational symmetry, or a point of centrosymmetry, but not a periodicity for translational repetition. A 2-D schematic plot (Penrose tiling [302]) illustrating the structure of quasicrystals is shown in Fig. 34.

Since fivefold environment is quite common in liquids and MGs, as discussed in previous sections, it is tempting to speculate that there might be structural similarities between quasicrystals and MGs. Indeed, icosahedral quasicrystalline phases have been found in many MG-forming alloys, such as  $\text{Ti}_{39.5}\text{Zr}_{39.5}\text{Ni}_{21}$  [304],  $\text{Zr}_{59}\text{Ti}_3\text{Cu}_{20}\text{Ni}_8\text{Al}_{10}$  [305],  $\text{Zr}_{65}\text{Cu}_{7.5}\text{Al}_{7.5}\text{Ni}_{10}\text{Ag}_{10}$  [306], and  $\text{Hf}_{65}\text{Al}_{7.5}\text{Ni}_{10}\text{Cu}_{12.5}\text{Pd}_5$  [307]. It is interesting to note that the above alloys, and several other ETM-containing quasicrystal-forming systems, are all ETM-rich in composition. According to our analysis above, the supercooled

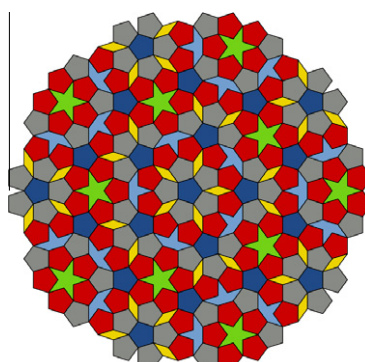


**Fig. 34.** A 2-D Penrose tiling (<http://en.wikipedia.org/wiki/Quasicrystal>). The tiles may correspond to a group of atoms in a real quasicrystal, and the pentagonal tiles are usually centered by icosahedral clusters.

liquids of these alloys should contain icosahedral clusters, but at relatively low fractions compared to the LTM-rich compositions; the latter, however, do not form quasicrystals upon quenching. There are several other well-known quasicrystal-forming alloys such as the Al-based ones [303]. They do not form BMG, and icosahedra are not expected to be the dominant structure in these MGs either. In fact, although icosahedral clusters are indispensable building blocks in quasicrystals, they may not be the most populous if we examine the SRO around each and every atom. Taking Fig. 34 as an example, each tile in the figure may represent a group of atoms in a quasicrystal, but only atoms at the very center of the pentagonal tiles are required to have icosahedral SRO; other atoms in pentagonal tiles, or atoms in other tiles, are not necessarily embedded in icosahedra. In other words, the fraction of atoms actually embedded (at the center) in icosahedra could be low, although a lot more atoms are involved in icosahedra (as shell atoms only); this is exactly the case for ETM-rich metallic glass/liquid, and the similarity may explain why quasicrystals preferentially form in this composition range. Some may wonder why quasicrystals do not form more often in the competition with MGs, since abundant five-fold bonds and icosahedral order develop over rather wide liquid composition ranges. This is partly because these intermetallic-compound-like quasicrystals have narrow free energy curves, i.e., the free energy rises rapidly when the alloy moves away from some specific compositions. The stringent composition and structure requirements for quasicrystals make them less competitive than MGs, except at some particular compositions. The nucleation of quasicrystal from MG-forming liquids and its implications for the structure of the liquids will be discussed in more detail in Section 4.1.2.

It should be noted that while it is now a consensus that icosahedral order is a characteristic SRO in many metallic liquids, glasses, and quasicrystals, the exact definition of icosahedral order may differ for different authors, and this is often where confusions and misunderstandings arise. The geometrically perfect/ideal icosahedron has a slightly smaller atom (with a size ratio of 0.902) at center and equilateral edges (see Section 3.7.1), which is the prototypical form of the non-ideal icosahedral clusters in real materials. However, such perfect icosahedra do not really exist in liquids and glasses, owing to the different sizes of the various atomic species involved in the alloy as well as thermal fluctuations. The  $\langle 0,0,12,0 \rangle$  clusters, as we discussed above for example in the Cu-Zr alloys, have complete fivefold environment (i.e., all 12 bonds are fivefold bonds), and are termed full icosahedra in our discussion (see an example in Fig. 28). In this definition, clusters are not required to be perfect icosahedra; they are considered “full” as long as the distortion is not significant enough to change the complete fivefold bonding environment. Considering the intrinsic fluctuations and uncertainties in liquids and glasses, such a definition should be appropriate for studying the amorphous structures, as demonstrated above in Cu-Zr. Some authors used the term “icosahedral” order in a more loosely defined way. For example, the predominance of 555 pairs (CNA index) or 1551 pairs (H-A index) has been taken as evidence of icosahedral order. However, it should be clarified that many commonly seen clusters in MGs all have high fractions of fivefold bonds (and thus high fraction of 555 or 1551 pairs), such as  $\langle 0,3,6,0 \rangle$ ,  $\langle 0,2,8,0 \rangle$ ,  $\langle 0,2,8,1 \rangle$ ,  $\langle 0,2,8,2 \rangle$ , and  $\langle 0,1,10,2 \rangle$ . Obviously, not all of them can be called icosahedra. Those with CN close to 12 (e.g.,  $\langle 0,2,8,1 \rangle$ ,  $\langle 0,2,8,2 \rangle$ ,  $\langle 0,1,10,2 \rangle$ ) may be reasonably defined as distorted icosahedra. In DRPHS or monatomic metallic liquids, the fivefold bonds are found to be populous, but the fraction of  $\langle 0,0,12,0 \rangle$  full icosahedra is not high, as the majority of the fivefold bonds are in the distorted icosahedra (e.g., [192,193]). The full icosahedra dominate only in some MGs at certain compositions (e.g., Cu-rich Cu-Zr), as their formation requires an appropriate effective size ratio.

### 3.7. General structural models for metallic glasses

Like crystalline alloys, different MGs can also have very different structures. There are two approaches to understand the various MG structures. One is to study individual MGs and summarize the main structural features, similarities, and differences, which have already been surveyed in previous sections. The other is to identify the underlying mechanisms and general principles that determine the structures of MGs, which can be used to design MGs and establish the structure basis of MG behaviors. Of course, the two approaches are closely linked, and our discussions above (e.g., those on various models) have in fact touched on both. This section focuses more on the second approach, with additional thoughts on the general models.

### 3.7.1. Polytetrahedral packing model and the role of disclinations

We first discuss the structure in terms of polytetrahedral packing that incorporate disclinations, built on the original idea and early studies by Nelson and Spaepen [172]. In Section 3.1., we have mentioned that equilateral tetrahedron alone cannot fill the flat 3-D space, and even if we allow slight distortion, the resulting icosahedron with fivefold rotational symmetry is still incompatible with long-range translational order. In a bulk polytetrahedral packing, therefore, rotational “defects” (i.e., disclinations), usually seen as sixfold and fourfold bipyramids, are inevitable. They are termed sixfold and fourfold (corresponding to  $-72^\circ$  and  $+72^\circ$ , respectively [173]) disclinations in the rest of this review, for convenience of discussion. In DPRHS, while striving to use as many tetrahedral holes and icosahedra as possible, local distortions and other types of holes provide the required disclinations to fill the gap. Alternatively, if we abandon the effort to maximize the tetrahedrality, we may rearrange the shell atoms to obtain an fcc cluster with Voronoi index  $\langle 0, 12, 0 \rangle$  (which is not a polytetrahedral packing), and the packing frustration is dissolved. The question is, then, does there exist a compromising structure, in which polytetrahedral packing with long-range order is achieved, by allowing moderate mismatch in bond lengths and incorporating ordered distribution of disclinations? The answer is yes, and the idea was actually introduced by Frank and Kasper in 1958 to explain the structure of complex alloys [308,309].

We start from an example, the A15 phase. The unit cell of A15 structure consists of two  $\langle 0, 0, 12, 0 \rangle$  icosahedral cells and six  $\langle 0, 0, 12, 2 \rangle$  cells ( $CN = 14$ ) with two sixfold disclinations for each, see Fig. 35. Like  $\langle 0, 0, 12, 0 \rangle$ , the  $\langle 0, 0, 12, 2 \rangle$  cluster is also a polytetrahedral packing, i.e., by connecting the shell atoms that are nearest neighbors (as determined by the Voronoi method), we have a triangulated coordination shell with nearly equal edges. In addition, the radial bonds connecting the center atom with the neighbor atoms are  $\sim 2\%$  longer. Since the  $\langle 0, 0, 12, 2 \rangle$  cluster has two disclinations to relieve the packing frustration, it is now possible to fill the space by arranging  $\langle 0, 0, 12, 0 \rangle$  and  $\langle 0, 0, 12, 2 \rangle$  in an ordered manner, as demonstrated by the A15 unit cell in Fig. 35.

In fact, similar polytetrahedral packing can also be achieved for other CNs, if we allow the radial bonds to be longer or shorter, but still require a triangulated coordination shell with nearly equal edges. In Fig. 36, we plot all these clusters from  $CN = 8$  to  $CN = 16$ , labeled by the corresponding Voronoi indices. The clusters for  $CN = 12, 14, 15, 16$  are the canonical Kasper polyhedra with sixfold disclinations only (no disclination for  $CN = 12$ ) [308], while the clusters for  $CN = 8, 9, 10$  correspond to the canonical Bernal holes [164] with fourfold disclinations only (or anti-defect of the canonical Kasper polyhedra [172,173]). For a triangulated coordination shell in a polytetrahedral packing,  $2n_4 + n_5 = 12$  must be satisfied [308], and  $\langle 0, 1, 10, 0 \rangle$  ( $CN = 11$ ) and  $\langle 0, 0, 12, 1 \rangle$  ( $CN = 13$ ) do not exist because single disclination (either fourfold or sixfold) is prohibited. As a result, clusters for  $CN = 11$  and 13 contain both types of disclinations. Given the above constraints, it is interesting to notice that all clusters in Fig. 36 have maximum possible number of fivefold bonds  $n_5$  with minimum disclinations at the corresponding CN [310]. These clusters are often labeled as Z8,Z9,...,Z16, and some authors call all of them Kasper polyhedra [152,310]. To avoid confusion and conflict with the original definition of Kasper polyhedra [308], in the following discussion of this review, we will call these polytetrahedral clusters (with various CN and minimum disclinations) “Z clusters”. It is important to note

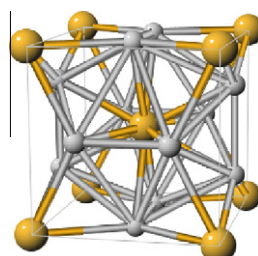


**Fig. 35.** The unit cell of an A15 structure. Large yellow atoms are centers of  $\langle 0, 0, 12, 0 \rangle$  Voronoi cells, while small gray atoms are centers of  $\langle 0, 0, 12, 2 \rangle$  Voronoi cells.

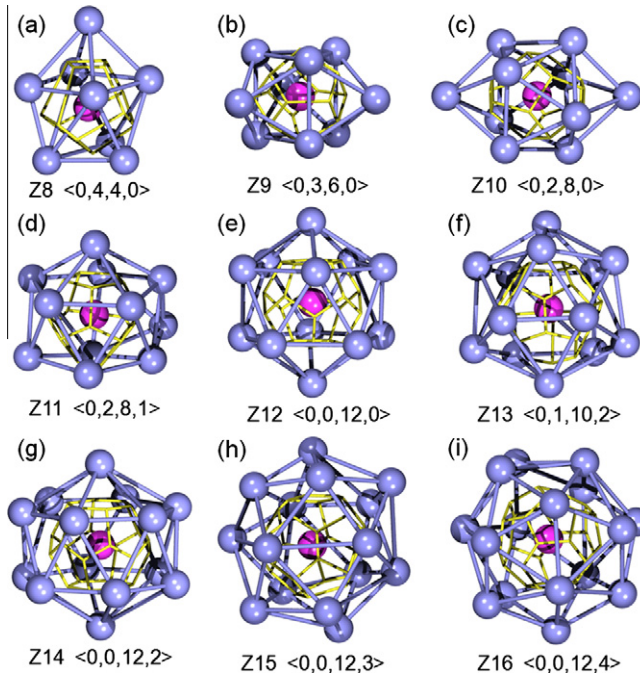


**Fig. 36.** Z clusters with polytetrahedral packing and triangulated shell. For each cluster, the center atom is colored pink, and the yellow edges outline the Voronoi cell.

that the bond lengths (for both the shell bonds and the radial bonds) are not necessarily identical for a given type of Z cluster. In other words, the Z cluster defined here is not a definite configuration, but a range of configurations featured by the same CN and Voronoi index. Such a tolerance is actually required in order to represent MG structures, because atoms may have different sizes and they may also have various arrangements and fluctuations in a real-world MG. Except for Z12, all other clusters have fourfold and/or sixfold disclinations, and can be used to relieve the packing frustration.

Since the Z clusters cover a wide CN range, the radial bond length would not be equal to the shell bond length. For example, for CN = 8, the radial bond is 19% shorter; while for CN = 16, the radial bond is 9% longer. Therefore, when the atom in center has a different size than the shell atoms to favor a particular CN other than 12, the disclinations required for space tiling, the topological efficiency and energetic stability of the individual clusters, and the long-range ordering of these clusters containing disclinations, may be all achieved simultaneously. This is the case for the Frank–Kasper phases in some complex alloys [308] (e.g., A15 phase in Fig. 35).

The Z clusters can be distorted while keeping the CN unchanged. The distortion would create four-fold and six-fold disclinations in pairs, subject to the constraint of  $2n_4 + n_5 = 12$ . For example,  $\langle 0,0,12,0 \rangle$  can be distorted to be  $\langle 0,2,8,2 \rangle$ ,  $\langle 0,3,6,3 \rangle$ , etc.;  $\langle 0,2,8,0 \rangle$  can be distorted to be  $\langle 0,3,6,1 \rangle$ , etc. The reverse process would annihilate the disclination pairs and recover to the Z clusters. Borodin [311,312] has systematically studied all possible clusters for polytetrahedral packing, and we summarize the most relevant ones for MGs in Table 4. For an efficient packing of solute-centered cluster, the most stable/favored configuration is presumably the Z clusters with fewest disclinations [152,311,312], and the CN would be determined by the effective size ratio of solute and solvent. If CN is not 12, the stable Z cluster would contain disclinations. We call these disclinations “intrinsic”: they are not true defects in terms of energy, and are intrinsic to the cluster as a result of efficient packing with atoms of difference sizes. The extra disclination pairs due to distortion and lower packing efficiency are called extrinsic disclinations. In 3-D packing, the former complement the fivefold symmetry to fulfill the space tiling without sacrificing the stability. The latter, however, make the cluster energetically

**Table 4**

Polytetrahedral clusters with fourfold and sixfold disclinations.

CN	Z clusters	→ increasing (extrinsic) disclination density →
8	(0,4,4,0)	
9	(0,3,6,0)	(0,4,4,1)
10	(0,2,8,0)	(0,3,6,1)
11	(0,2,8,1)	(0,3,6,2)
12	(0,0,12,0)	(0,2,8,2)
13	(0,1,10,2)	(0,2,8,3)
14	(0,0,12,2)	(0,1,10,3)
15	(0,0,12,3)	(0,1,10,4)
16	(0,0,12,4)	(0,1,10,5)
17	(0,0,12,5)	(0,1,10,6)
		(0,2,8,7)
		(0,3,6,8)
		(0,4,4,9)

unstable and play the role of structural defects. For example, the Frank–Kasper phase contains ordered intrinsic disclinations only [172,173], while in MGs, both intrinsic and extrinsic disclinations exist, with a random spatial distribution [310]. The disclinations associated with each cluster can be represented by the fourfold or sixfold lines connecting the center and shell atoms, see Fig. 37a. Therefore, if we plot all the disclination lines in a random packing of Z clusters, we would have a pattern similar to Fig. 37b.

In MGs, the intrinsic disclinations associated with the regular Z clusters are introduced and stabilized to relieve packing frustration, and this can be achieved by selecting the size ratio and composition for desired CNs, as noted by Doye and Meyer [313] and Ganesh and Widom [193]. In high temperature liquids, the structure is highly distorted and extrinsic disclinations dominate. Upon

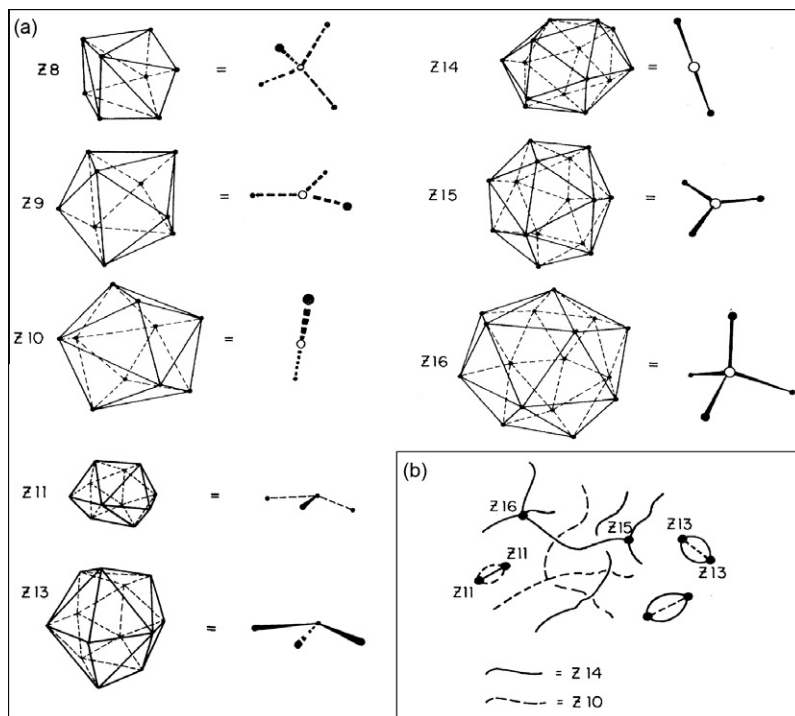


**Fig. 37.** (a) Z clusters and their disclination representations. (b) Schematic plot of disclinations in a random polytetrahedral packing with Z clusters. In both panels, bold lines represent the sixfold disclinations, and dashed lines represent the fourfold disclinations. (Adapted from [173] with permission © 1983 by American Physical Society.)

cooling, the density of extrinsic disclinations gradually decreases, and more Z clusters form. The MG after glass transition would naturally inherit certain density of extrinsic disclinations. Such a density can be further reduced by using slower cooling rate or annealing. The reduction of disclination density (i.e., annihilation of extrinsic disclination pairs) leads to the sharper first peak of partial PDF (i.e., more uniform bond/edge length) [314–316] and larger fraction of regular Z clusters. The intrinsic disclinations may also be better aligned in this process. In fact, Nelson and Spaepen proposed that the ideal glass, if it exists, should be a Frank–Kasper phase with infinite unit cell [172,173], which is consistent with the scenario described above (i.e., extrinsic disclinations are eliminated).

Based on the above discussion, it appears that the extrinsic disclinations in MGs resemble the dislocations in crystals, both of which are structural defects associated with distortion and instability. However, one should not read too much into this analogy. A dislocation can be easily told apart from the otherwise perfect crystalline lattice, while the structural signature of a disclination in MGs (not in Frank–Kasper phases or quasicrystals) is much more smeared and subtle in the amorphous matrix. In fact, it is very difficult to unambiguously define a structural defect in MG, and a disclination, even we can identify it, would not work like a dislocation in crystals. The so-called defects in MGs must be interpreted statistically. For example, knowledge of the spatial distribution and local density of extrinsic disclinations, instead of the position or type of an individual disclination, would be more useful and relevant in understanding the structural state and microscopic properties of the MG, as will be demonstrated later in this review.

The disclination model can be examined using computer simulations. Early work by Qi and Wang [300] has demonstrated the entangled disclinations in a Ca<sub>7</sub>Mg<sub>3</sub> model MG. Here we study the Cu–Zr example that was discussed previously. First of all, with increasing Cu content from Cu<sub>30</sub>Zr<sub>70</sub> to Cu<sub>70</sub>Zr<sub>30</sub>, average CN around Cu increases from ~10 to ~12, while average CN around Zr increases from ~14 to ~16. It can be seen from Fig. 28 that the dominant clusters around Cu are always Z clusters, regardless of the composition and average CN (Table 5). In addition to the Z clusters, there are smaller fractions of non-Z clusters but with relatively low density of disclinations, such as ⟨0, 3, 6, 1⟩ and ⟨0, 2, 8, 2⟩. As for the Zr-centered clusters (Table 6), however, the distribution is rather broad. Specifically, on the Zr-rich side, Z clusters are in fact not the most populous compared to the non-Z clusters. This is because at this composition, Cu has an average CN < 12, such that the Cu-centered Z clusters contain intrinsic fourfold disclinations. However, with average CN > 13 around Zr, the corresponding Z clusters have no fourfold disclination. Since the same disclination is shared by nearest-neighbor pairs, lower Cu concentration, which leads to larger fraction of Cu intrinsic fourfold disclinations and fewer Cu–Cu bonds, would necessarily mean that more of these fourfold disclinations need to be shared with Zr. This is why on the Zr-rich side many Zr-centered clusters are non-Z clusters, containing high density of disclinations. When moving to the Cu-rich side, the average CN around Cu approaches 12, for which the Z cluster (⟨0, 0, 12, 0⟩) has no intrinsic disclination. This relieves the constraint on Zr so that its local packing becomes more regular (i.e., clusters with fewer disclinations, such as ⟨0, 1, 10, 4⟩ and ⟨0, 1, 10, 5⟩, become more populous). Note that the intrinsic

**Table 5**

Fractions of Cu-centered polytetrahedral clusters in Cu–Zr (%). Dominating clusters are italicized.

	Index	Cu <sub>30</sub> Zr <sub>70</sub>	Cu <sub>50</sub> Zr <sub>50</sub>	Cu <sub>70</sub> Zr <sub>30</sub>
CN = 9	⟨0, 3, 6, 0⟩	4.9	1.7	0.1
CN = 10	⟨0, 2, 8, 0⟩	19.9	10.0	1.6
	⟨0, 3, 6, 1⟩	12.0	5.5	1.3
CN = 11	⟨0, 2, 8, 1⟩	24.9	23.7	10.6
	⟨0, 3, 6, 2⟩	4.0	4.4	2.3
	⟨0, 4, 4, 3⟩	4.8	2.5	1.3
CN = 12	⟨0, 0, 12, 0⟩	3.6	15.0	31.0
	⟨0, 2, 8, 2⟩	8.5	13.4	14.7
	⟨0, 3, 6, 3⟩	4.2	5.6	4.9
CN = 13	⟨0, 1, 10, 2⟩	0.0	1.8	9.0
	⟨0, 2, 8, 3⟩	0.0	0.6	2.2
	⟨0, 3, 6, 4⟩	0.0	2.1	5.3

**Table 6**

Fractions of Zr-centered polytetrahedral clusters in Cu-Zr (%).

	Index	Cu <sub>30</sub> Zr <sub>70</sub>	Cu <sub>50</sub> Zr <sub>50</sub>	Cu <sub>70</sub> Zr <sub>30</sub>
CN = 13	(0,1,10,2)	5.0	1.7	0.0
	(0,2,8,3)	1.9	0.5	0.0
	(0,3,6,4)	5.2	1.8	0.0
CN = 14	(0,0,12,2)	2.1	2.3	1.1
	(0,1,10,3)	4.9	3.6	1.4
	(0,2,8,4)	9.6	5.2	1.8
	(0,3,6,5)	5.6	2.5	0.0
	(0,4,4,6)	3.1	1.6	0.2
CN = 15	(0,0,12,3)	1.0	2.3	4.4
	(0,1,10,4)	4.8	6.4	8.4
	(0,2,8,5)	5.0	6.5	5.7
	(0,3,6,6)	3.5	3.1	1.5
	(0,4,4,7)	1.5	1.3	0.5
CN = 16	(0,0,12,4)	0.2	0.7	5.2
	(0,1,10,5)	0.8	2.5	10.4
	(0,2,8,6)	1.0	2.1	5.9
	(0,3,6,7)	0.0	1.0	1.3
CN = 17	(0,0,12,5)	0.0	0.0	1.1
	(0,1,10,6)	0.0	0.0	3.0
	(0,2,8,7)	0.0	0.0	2.4

sixfold disclinations associated with Zr may also need to be accommodated by Cu when Zr-Zr pairs are insufficient at Zr-poor compositions. However, since both Z11 and Z13 are abundant around Cu (average CN = 12 for Zr-poor Cu-Zr), and they both contain intrinsic sixfold disclinations, the requirements can be met without significantly sacrificing the packing efficiency around Cu. The above analysis not only reveals the polytetrahedral packing nature of the Cu-Zr MG, but also shows that packing around Cu is indeed more efficient. In comparison, packing around Zr, influenced by the intrinsic fourfold disclinations associated with Cu, cannot achieve the highest packing efficiency for Zr itself. Such a compromised balance is composition dependent, and the overall packing frustration (for both Cu and Zr) is minimized on the Cu-rich side. These descriptions are consistent with experimental observations by Ma et al. [268] and simulation results of Cheng et al. [269], and also confirm the dominating role of Cu-centered clusters.

In addition to the composition dependence, it is also important to examine the cooling rate effect. In Tables 7 and 8 we show the polytetrahedral clusters in two MGs obtained at three different cooling

**Table 7**Cooling rate effect on polytetrahedral packing around Cu in Cu<sub>46</sub>Zr<sub>54</sub> and Cu<sub>64</sub>Zr<sub>36</sub> MGs (%).

	Index	Cu <sub>46</sub> Zr <sub>54</sub>			Cu <sub>64</sub> Zr <sub>36</sub>		
		10 <sup>12</sup> K/s	10 <sup>11</sup> K/s	10 <sup>10</sup> K/s	10 <sup>12</sup> K/s	10 <sup>11</sup> K/s	10 <sup>10</sup> K/s
CN = 9	(0,3,6,0)	2.3	2.1	2.1	0.2	0.3	0.3
CN = 10	(0,2,8,0)	11.9	11.4	12.7	3.6	4.0	3.5
	(0,3,6,1)	8.3	7.7	7.1	3.1	2.7	2.5
CN = 11	(0,2,8,1)	23.5	24.3	26.1	15.0	14.1	13.7
	(0,3,6,2)	4.1	4.5	3.9	2.9	2.9	2.5
	(0,4,4,3)	3.1	3.1	3.0	2.1	1.9	1.7
CN = 12	(0,0,12,0)	9.7	11.8	12.6	23.7	26.7	31.1
	(0,2,8,2)	12.1	12.2	12.2	15.3	15.5	15.2
	(0,3,6,3)	6.1	5.7	5.0	6.2	5.4	4.8
CN = 13	(0,1,10,2)	1.0	0.9	1.2	6.2	6.4	6.7
	(0,2,8,3)	0.2	0.4	0.5	1.5	1.4	1.3
	(0,3,6,4)	2.2	1.5	1.5	4.2	3.9	3.5

**Table 8**Cooling rate effect on polytetrahedral packing around Zr in Cu<sub>46</sub>Zr<sub>54</sub> and Cu<sub>64</sub>Zr<sub>36</sub> MGs (%).

	Index	Cu <sub>46</sub> Zr <sub>54</sub>			Cu <sub>64</sub> Zr <sub>36</sub>		
		10 <sup>12</sup> K/s	10 <sup>11</sup> K/s	10 <sup>10</sup> K/s	10 <sup>12</sup> K/s	10 <sup>11</sup> K/s	10 <sup>10</sup> K/s
CN = 13	$\langle 0, 1, 10, 2 \rangle$	2.8	2.3	2.4	0.0	0.5	0.0
	$\langle 0, 2, 8, 3 \rangle$	0.0	0.7	0.8	0.0	0.0	0.0
	$\langle 0, 3, 6, 4 \rangle$	2.1	2.2	1.9	0.4	0.5	0.3
CN = 14	$\langle 0, 0, 12, 2 \rangle$	1.8	2.1	2.2	1.1	1.2	1.7
	$\langle 0, 1, 10, 3 \rangle$	4.1	3.6	4.1	2.1	2.0	1.9
	$\langle 0, 2, 8, 4 \rangle$	6.6	6.4	6.5	3.0	2.8	2.7
	$\langle 0, 3, 6, 5 \rangle$	2.8	2.9	3.4	1.1	1.3	1.0
	$\langle 0, 4, 4, 6 \rangle$	2.2	2.0	1.7	0.5	0.0	0.0
CN = 15	$\langle 0, 0, 12, 3 \rangle$	1.6	1.8	1.6	3.7	3.2	5.3
	$\langle 0, 1, 10, 4 \rangle$	5.3	5.4	5.9	7.2	7.6	8.8
	$\langle 0, 2, 8, 5 \rangle$	5.9	6.5	7.0	6.6	6.8	6.8
	$\langle 0, 3, 6, 6 \rangle$	3.8	3.8	3.2	2.4	2.6	2.3
	$\langle 0, 4, 4, 7 \rangle$	0.0	1.3	1.4	1.1	1.2	0.8
CN = 16	$\langle 0, 0, 12, 4 \rangle$	0.6	0.6	0.0	2.5	2.9	3.9
	$\langle 0, 1, 10, 5 \rangle$	2.0	1.9	2.1	6.6	6.7	7.9
	$\langle 0, 2, 8, 6 \rangle$	2.0	2.1	2.0	5.1	5.8	5.5
	$\langle 0, 3, 6, 7 \rangle$	1.1	0.9	0.9	1.8	0.0	1.4
CN = 17	$\langle 0, 0, 12, 5 \rangle$	0.0	0.0	0.0	0.0	0.5	0.6
	$\langle 0, 1, 10, 6 \rangle$	0.0	0.0	0.0	1.1	1.3	1.7
	$\langle 0, 2, 8, 7 \rangle$	0.0	0.0	0.0	1.1	1.3	1.3

rates. For Cu-centered clusters, it is clear that with decreasing cooling rate, the fractions of Z clusters at the favored CNs (11 and 12 for Cu<sub>46</sub>Zr<sub>54</sub> and 12 for Cu<sub>64</sub>Zr<sub>36</sub>, italicized in Table 7) increase, reducing the disclination density and narrowing the CN distribution. This shows the annihilation of extrinsic disclinations during cooling, and the fact that Z clusters with the favored CNs (determined by the size ratio) are the most stable local structural units in MGs. The cooling rate dependence of Zr clusters, at least in MD simulation, is not obvious. This again justifies the use of Cu-centered clusters to study Cu-Zr MGs.

We have focused our discussion on the Cu-Zr example. But in fact, the polytetrahedral packing with Z clusters seems to be quite general. It also applies for the other MG types covered in this review, such as the LTM-NM and Al-based MGs. In general, it appears that the atomic structure of MGs can be perceived as consisting of regular and distorted Z clusters. The type of the dominant Z cluster is determined by the average CN, which can be estimated from the effective atomic size ratio and the make-up of nearest-neighbor shell; the latter is further determined by the overall composition of the MG and the chemical affinity between the constituent elements.

The principle of polytetrahedral packing is to maximize the packing efficiency in the nearest-neighbor shell, so that atoms in the cluster are best accommodated locally. But in many cases, the best local packing scheme (often with high rotational symmetry) may not be compatible with long-range translational order. As a result, simple crystals usually adopt a different local arrangement of atoms. One example is the icosahedral versus fcc packing in monatomic systems. In more complicated cases, although the detailed structure could be different, the fundamental competition between glass and crystal, in terms of local versus global choice of optimal structure, is expected to be the same. A demonstration of this competition is that in MGs, the average nearest-neighbor distance between two atoms is sometimes close to, but often even shorter than, the bond length in corresponding intermetallic compounds (see examples in Table 9). The average CN in glass may also be higher. This suggests that without worrying about the constraint to establish long-range order, the preferred short-range packing can be better satisfied in a glass than in crystals. A similar argument has been made for some chalcogenide glasses [317]. Likewise, the fact that the clusters are not isolated but part of the 3-D bulk material may also affect the average packing structure of the cluster. Liu et al. [318], by studying the normalized peak positions in the PDFs of various MGs, suggest that the MG short-to-medium-range

**Table 9**

Nearest-neighbor distance and partial CNs of cluster packing in glasses and crystals, demonstrating that some MGs may have even higher *local* (short-range) packing efficiency than in crystals. Note that the partial CNs in glasses may have relatively large uncertainty.

Glass Crystal Refs.	(center atom)–(shell atom)	Glass		Crystal	
		Average partial CN	Average bond length (Å)	Partial CN	Bond length (Å)
Ni <sub>80</sub> P <sub>20</sub> [133,319,320]	Ni–Ni	10.7	2.5	10.7	2.6
	Ni–P	2.3	2.2	3	2.3
	P–Ni	9.3–10.5	2.2	9	2.3
	P–P	12–13	3.9	11	3.9
Cu <sub>35</sub> Zu <sub>65</sub> [134,320]	Cu–Cu	4.6	2.63	4	3.22
	Cu–Zr	6.9	2.80	8	2.90
	Zr–Cu	3.7	2.80	4	2.90
	Zr–Zr	9.4	3.16	4	3.04 (1) 3.22 (2)
Al <sub>89</sub> La <sub>6</sub> Ni <sub>5</sub> Al <sub>3</sub> Ni & Al <sub>11</sub> La <sub>3</sub> [93,242]	Al–Ni	6–9.4	2.43	9	2.49
	Al–La	15.8–17.5	3.33	16	3.365
Mg <sub>60</sub> Cu <sub>30</sub> Y <sub>10</sub> Mg <sub>2</sub> Cu [298]	Mg–Mg	7.5	2.93	6	3.02
	Mg–Cu	1.4	2.72 (1)	4	2.74
	Cu–Cu	2.4	3.03 (2)		
		2.0	2.55	2	2.62

<sup>a</sup> Ni<sub>3</sub>P has complex crystal structure. For Ni–Ni, Ni–P, P–Ni partials, atoms with distance less than 3 Å are considered nearest neighbors. The partial CN and bond length are average of all nearest neighbors at all sites. P atoms with distance less than 5 Å are considered P–P neighbors, and the P–P distance is also an average.

structure can be viewed as having characters of both spherical periodic order and local translational order, which is probably a result of the compromise to satisfy to certain extent both the local individual atoms and the 3-D structure as a whole. In other words, while each and every atom strives to maximize the spherical symmetry around itself, they eventually share certain translational features to accommodate each other in their endeavor to fill the entire space.

### 3.7.2. Efficient packing of solute-centered clusters

The polytetrahedral packing model discussed above provides a description of the SRO, but a picture of the MRO is not given. In the polytetrahedral packing model, the atomic size ratio is a critical parameter determining the CN and cluster type, and the most favored clusters are likely to be the Z clusters with minimal disclinations, which is supported by available results in experiments and simulations for various MGs. In fact, the importance of atomic size (and its difference between the constituent species) in determining the SRO in MGs has been well recognized and discussed by many researchers, for example Inoue and Takeuchi [7], Egami and Waseda [321], Doye and Meyer [313], and Miracle and Senkov [221,322–324]. Taking a step further, if the MG is solute-lean and the solute atoms are surrounded by solvent only, then the solute-centered clusters can be considered as the basic building blocks of MGs, and a plausible interpretation of the MRO would be the efficient packing of these clusters by sharing solvent atoms in the shell. This is the idea behind the efficient cluster packing (ECP) model recently proposed by Miracle [221]. In the context of ECP, there are two basic questions to be addressed: (1) how to achieve stable solute-centered clusters by selecting the size ratio *R* between center solute and surrounding solvent and (2) how these clusters are connected and arranged in medium range.

Miracle and co-workers have conducted systematic research to answer these two questions, as detailed in Refs. [221,322–326]. Briefly, their model assumes that the representative SRO in MGs is the solute-centered clusters with solvent efficiently packed surrounding the center solute. The CN is determined by the size ratio *R* between solute and solvent. If we divide the total surface area of the

solute (center) atom by the area effectively occupied by each solvent (shell) atom, the average CN for efficient packing can be solved, which increases continuously with increasing  $R$ . For the CN to be an integer, there are thus preferential and discrete  $R$  values ( $R^*$ ) corresponding to each CN, see Table 10 [324]. Note that the approach described above only follows the area criterion (i.e., the total surface area of the center atom is equal to CN times of the area occupied by a single shell atom); the calculation itself does not consider the feasibility of the packing (i.e., how to arrange the shell atoms to cover the entire area seamlessly, without overlap and empty space). It turns out that such ideal packing schemes with the exact  $R^*$  and the maximum packing efficiency can only be achieved for CN = 4 (tetrahedron), 6 (octahedron), and 12 (icosahedron) [308,324], while for other CNs, the  $R^*$  values are actually a lower bound expectation, because ideal packing for these CN- $R^*$  combinations does not exist, and in a realistic packing (assuming the atoms are hard and incompressible), the observed  $R^*$  favoring certain CN is likely to be higher than the values listed in Table 10, as demonstrated by the candidate clusters proposed in Ref. [325]. Note that several candidates were studied for each CN in [325], including not only the Z clusters discussed previously in the context of polytetrahedral packing, but also some other possibilities that have not been observed in MGs so far.

The solute-centered clusters connect with each other by sharing solvent atoms in the shell, and pave the space to constitute the MRO. Miracle believes that the solute centers ( $\alpha$ ) usually form an fcc (or simple cubic in some cases) array extending to no more than a few cluster diameters, while there is no orientational order amongst the clusters, rendering random packing of the solvent atoms ( $\Omega$ ). There are two additional solute sites with different sizes in an fcc lattice: the octahedral site ( $\beta$ ) and the tetrahedral site ( $\beta$ ), see Fig. 38. For each solute ( $\alpha, \beta, \gamma$ ), the size ratio  $R$  relative to the solvent ( $\Omega$ ) determines the preferred CN and the size of the solute-centered cluster. When the composition and the relative sizes are all tuned to an appropriate combination, efficient packing of solute-centered clusters with the solutes forming an fcc array can be achieved (Fig. 38), and the glass structure is designated as  $\langle \text{CN}_\alpha, \text{CN}_\beta, \text{CN}_\gamma \rangle_{\text{fcc}}$ . Note that the three solute sites are characterized by size, not the element type. For example, Cu and Ni would be treated the same solute in this model, as they have very similar size.

**Table 10**

Optimal size ratio  $R^*$  between solute (center) and solvent (shell) atoms and the corresponding CNs for efficient packing [324].

CN	$R^*$	CN	$R^*$	CN	$R^*$
4	0.225	10	0.799	16	1.183
5	0.362	11	0.884	17	1.248
6	0.414	12	0.902	18	1.311
7	0.518	13	0.976	19	1.373
8	0.617	14	1.047	20	1.433
9	0.710	15	1.116	21	1.491

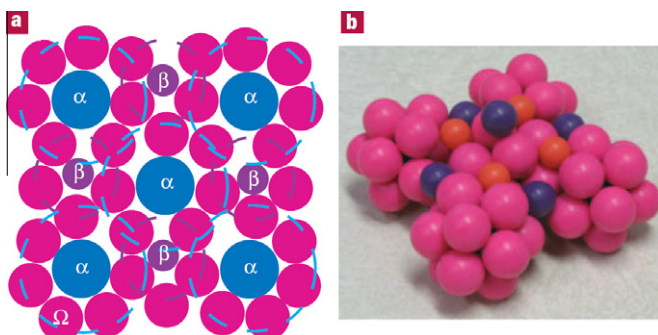


**Fig. 38.** Miracle's model: fcc MRO of solute-centered clusters. The 3-D structure in (b) is of  $\langle 12, 10, 9 \rangle_{\text{fcc}}$  type. (Reproduced from [221] with permission © 2004 by Nature Publishing Group.)

The above model found support from the following observations [322]: (1) given the R values in an MG, its composition can be estimated using the model, and compared with the glass forming composition in experiments; (2) the partial PDFs, particularly the solute–solute spatial correlation, can be extracted from the model and compared with the experimentally measured PDF data; (3) the partial CNs and (4) density are also available from both the model and experiments for comparison.

As mentioned earlier, recent findings of Sheng et al. [152] confirmed the dominance of solute-centered clusters and proposed the possibility of DRP of these clusters, which is characterized by icosahedra-containing, DRP-like MRO rather than crystal-like MRO. Specifically, DRP of P-centered clusters was found in Ni<sub>80</sub>P<sub>20</sub> configurations generated using both RMC and *ab initio* MD, and the 3-D structure can reproduce various experimental results, including the XRD, partial PDFs, Ni and P K-edge EXAFS and XANES, etc. Similar MRO was also observed in *ab initio* simulations of several other MGs such as Ni<sub>81</sub>P<sub>19</sub> and Zr<sub>84</sub>Pt<sub>16</sub>. In addition, the solute-centered clusters identified in realistic glasses by Sheng et al. are only quasi-equivalent and of various CNs/types in a distribution, and interconnect via a variety of arrangements (vertex-, edge-, and face-sharing).

The above debate leads to a fundamental question: what determines the cluster packing scheme and the MRO, i.e., what is the principle underlying the medium-range correlation of the solute centers? If the quasi-equivalent clusters can be treated as hard spheres, both fcc and icosahedral packing would be fairly efficient and stable within the typical range of MRO (a few cluster diameters up to ~1 nm). The MRO in a realistic MG, however, may not be a clear-cut fcc or icosahedral configuration. The ordering is more likely to be distorted, and with increasing length-scale, the distortion could be significant enough to smear out the difference between the fcc-like MRO and icosahedral-like MRO [326]. More importantly, the hard sphere packing scheme does not hold well for cluster packing by sharing shell atoms. The correlation between the clusters cannot be represented by the simple pair interaction; instead, it is much more complicated and determined by the various sharing schemes of solvent atoms. To maximize the stability and achieve global low energy, the solute-centered clusters must be arranged in a way that the solvent atoms are also surrounded by preferential CNs with highest possible packing efficiency. Therefore, simply ignoring the environment of solvent atoms and sticking to a pre-defined solute sublattice would not always give the realistic picture; it is a convenient tool to use to construct an MG structure, but certainly not the fundamental rule that nature follows. In other words, there does not seem to be a reasonable justification why a certain type of MRO (either fcc-like or icosahedral-like) should be universal in MGs. Both of them (and perhaps other schemes) are possible, and the details may also be system-specific. In fact, the MRO may not be uniform even in a given glass.

Despite the variation and uncertainty of the MRO type, there is one principle that appears to be true: the packing of the solute-centered clusters must be dense and efficient [327]. In this regard, the ECP model has its general implications in understanding the MG structures and MRO. An advantage of assuming fcc-like cluster packing is that it allows quantitative estimates of the composition and size ratio for glass formation. Miracle and co-workers have applied this approach to many different MGs, to rationalize (although it cannot predict) the composition range for glass formation. The model has been successful because it highlights correctly the dominant SRO (CN) in some (solute-lean) MGs, and is also consistent with the main principle of the MRO (dense and efficient packing).

### 3.7.3. Summary and comparison of the structural models

In previous sub-sections, several structural models have been mentioned and discussed, including both specific models describing particular MGs and more general models outlining the basic principles. Here we present a brief summary and comparison of these structural models.

**3.7.3.1. DRPHS model.** Starting from a single sphere, the effort to build the densest packing with identical hard spheres would be inherently frustrated, because the densest local unit, tetrahedron, cannot be repeated to fill the 3-D space. As a result, the less dense units containing “holes” must be involved. Bernal proposed that five types of holes, including the tetrahedron, could be the basic structural units in monatomic liquids. In the DRPHS structures obtained in either experiments or simulations, tetrahedra are found to be dominant, and there are a large number of five-edged faces. These features are qualitatively consistent with subsequent observations in monatomic supercooled metallic liquids.

However, the DRPHS appears to have a maximum packing fraction of 0.64, which is ~14% lower than the packing fraction of fcc/hcp crystals (0.74). This difference is not realistic in most metals, for which the density only decreases slightly upon melting (usually less than 5%) [153]. Moreover, the characteristic packing fraction of 0.64 and the definition of DRP have been questioned recently. For example, Torquato et al. [328] noted that “dense” and “random” are not truly compatible with or independent of each other. When the packing becomes sufficiently dense, certain degree of order naturally follows. The packing fraction may increase continuously with order parameter, rendering the DRP ill-defined. It was then proposed that the DRP structure with 0.64 packing fraction actually corresponds to a maximally random jammed (MRJ) state, i.e., the jammed structure with maximal randomness [328]. Computer simulations by Sheng and Ma [329] demonstrated that the inherent structure of monatomic liquids indeed has intrinsic connections with the MRJ state. For MGs, therefore, the DRPHS captures only part of the truth: dense and efficient packing appears to be a fundamental principle, as illustrated repeatedly in preceding sections. But the metal atoms are not hard spheres, and packing is clearly not random.

**3.7.3.2. Polytetrahedral packing model.** The polytetrahedral packing is characterized by triangulated coordination shells surrounding the center atom with nearly equal edges. The DRPHS is essentially a frustrated polytetrahedral packing. Anikeenko et al. [330,331] showed that the DRP with its packing fraction reaching the 0.64 limit (or the MRJ) is the densest polytetrahedral packing one can achieve using identical hard spheres – to obtain even higher packing fraction, partially crystalline order with non-polytetrahedral nature has to be involved. Kamien and Liu [332] further suggested that the DRP corresponds to a metastable noncrystalline branch, which bifurcates from the crystalline branch. In other words, although the packing fraction can increase continuously, to exceed the 0.64 packing fraction a transition of the packing nature from noncrystalline to partially crystalline must be incurred. This explains why the 0.64 packing fraction has been reproducible in many experiments and simulations. For multicomponent systems, frustration of polytetrahedral packing can be greatly relieved by size mismatch and intrinsic disclinations associated with the Z clusters ( $CN \neq 12$ ), such that the packing fraction can be further enhanced, and the structure is also more stable. Indeed, the polytetrahedral packing characterized by Z clusters has been widely observed in various MGs, and appears to be a general principle of the MG structure (as detailed in Section 3.7.1). The success of polytetrahedral model originates from three characters of MGs: the lack of non-local constraint and long-range correlation, the weak directionality of metallic bonds, and the tendency to maximize the number of bonds at the favored bond lengths. Specifically, the choice of packing scheme in a metallic liquid/glass is made to maximize the local satisfaction of atoms and atomic clusters, without considering the compatibility with long-range order and the common good of the bulk structure. For metal atoms with weak directional preference, the local cluster is best satisfied (with low energy and high stability) by assuming the configuration of Z clusters with maximal tetrahedrality and number of nearest neighbors. It should be noted, however, that the polytetrahedral model describes the SRO only, and the MRO is not explicitly accounted for, although it is clear that polytetrahedral packing around each and every atom inevitably lead to certain type/degree of MRO.

**3.7.3.3. Stereochemical model.** Since the nearest-neighbor interaction is the strongest of all, Gaskell believes that the SRO in MGs is the same as that in the corresponding crystals, while the differences lie in the MRO (random for MGs and ordered for crystals). Although such a stereochemical description has been proven true in some MGs, particularly a group of LTM–NM MGs, it is not generally applicable, and does not appear to be a principle underlying the MG structure, as demonstrated in recent experiments and *ab initio* MD simulations. In fact, in MGs where the bonds are mostly metallic, the valence electrons are shared by ions in a non-directional fashion. As a result, the CN and bond angle are no longer subject to the strict constraints that usually apply for covalent or ionic glasses (such as silica glass, where the stereochemical model works well), and efficient packing turns out to be a more important and general structural principle in MGs. We have mentioned that in many cases, the SRO in the crystalline compound may not be the most “comfortable” configuration for the atomic cluster, as it could be a compromise to allow the long-range translational order. When such a constraint is lifted in MGs, the SRO may have other choices with different atomic arrangement or even different

CN ([Table 10](#)). Moreover, the CN in MGs can have intrinsic flexibilities and is not stereochemically fixed as in crystals.

**3.7.3.4. ECP model.** The general description of ECP model for solute-lean MGs has been demonstrated to be true, despite the difficulties in characterizing the exact MRO. In fact, it is unlikely that there would be a general and definite answer to the type of the MRO: either fcc or icosahedral could be an approximate description. It is expected that the MRO in the ECP model has a wide distribution and intrinsic fluctuation, which may make the efforts in distinguishing the subtle details fruitless. Miracle's model [221,322] based on the fcc description of MRO is a simplified picture facilitating calculation, but it is not necessarily the rule that the ECP really follows. The observations of DRP-like MRO by Sheng et al. [93,152] in several MGs provide a more realistic picture, but it is difficult to develop a quantitative model for simple calculations, out of the statistical results with inherent uncertainties. Moreover, for MGs of concentrated compositions, the solute–solute avoidance is no longer possible. The solute atoms connect with each other, forming chains or networks, and the structure may not be viewed as ECP by sharing solvent atoms. For example, in Cu–Zr MGs, it is useful to decipher the structure from the perspective of Cu-centered clusters, with both Cu and Zr in the shell. The ECP model needs modifications considering the interpenetration of clusters, and efforts have been made along this direction, by Miracle [333], Lu [334], and their co-workers.

Finally, it should be emphasized that the “clusters” discussed above should not be perceived literally as separated or isolated clusters. They are only a way to view and describe the densely packed atoms inside the MG structures, such that the packing principles and MG properties (see sections later) can be better described and summarized. It is an approach that is often justified by the convenience and insights it brings in analyzing the structure and structure–property relationship of the MG (e.g., P-centered cluster in Ni–P, or Cu-centered cluster in Cu–Zr, see their roles in controlling properties later). The ECP model should not be pictured as a “clusters (or molecules) plus voids” model. Different from network or molecular glasses, MG is truly atomic glass. Barring processing flaws, intrinsically the MG structure is dense and the atoms are well coordinated and homogeneously distributed throughout the material everywhere. In other words, every atom is surrounded by other atoms, in a coordination polyhedron. These local environments vary to some extent, but not to the point that there is empty space (such as voids) that separates the clusters. The excess volume (or free volume) is distributed on atomic scale. The “clusters plus glue atoms” model proposed by Dong and co-workers [248,335] could be a better approximation than the “clusters plus voids” model. However, the designation of “glue atoms” should not be conceived as implying that some atoms do not have their own well-defined coordination polyhedra and are not in any well-coordinated clusters. In reality, an MG is composed of a wide spectrum of various types of coordination polyhedra that fill space uniformly, rather than a composite/mixture of two bifurcated and distinct entities (one particular type of clusters plus defective boundaries containing random filler atoms).

### 3.7.4. MRO: a fractal packing proposition

Recently, a study suggests that the MRO in MG structure may be characterized as fractals. By summarizing neutron scattering data on various MGs, Ma et al. [266] noticed that the first peak position of the diffraction spectrum (or equivalently the total structure factor) and the average atomic volume of the MG have a universal scaling relation. The power-law scaling yields a fitting parameter ( $D_f$ ) of 2.31, which is smaller than the expected value ( $D_f = 3$ ) for 3-D solids (such as in an fcc crystal). The observation by Ma et al. is thought-provoking, and it may have important implications on the structure of MGs. Intuitively, a  $D_f$  smaller than three appears to indicate certain fractal feature in the atomic packing. Further analysis, however, suggests additional complexity of this problem.

First of all, the  $D_f = 2.31$  scaling constant is not truly universal for all MGs, as also noted by the authors [266]. To illustrate the scatter of data points, in [Fig. 39](#) below we have included all the data used by Ma et al. [266], and added a few more data points (red) from literature [152,236,254, 257,336]. The newly added points are from MGs of both metal–metal and metal–metalloid types, and some of them appear to not follow the original fitting very well.

Despite the increasing scatter when more (and more types of) MGs are included, the power-law scaling with  $D_f < 3$  seems to hold well for a selected group of MGs, especially some closely related ones

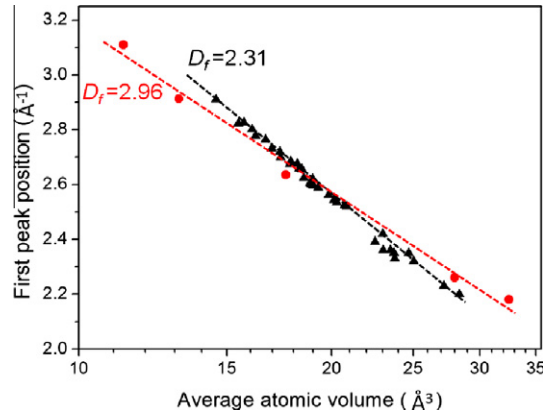


**Fig. 39.** Power-law scaling in various MGs, including the data used by Ma et al. [266] (black triangle) and a few more data points obtained from literature (red circles from left to right: Ni<sub>80</sub>P<sub>20</sub> [152], Pd<sub>40</sub>Cu<sub>30</sub>Ni<sub>10</sub>P<sub>20</sub> [336], Al<sub>90</sub>Fe<sub>5</sub>Ce<sub>5</sub> [236], Ce<sub>55</sub>Al<sub>45</sub> [254], La<sub>75</sub>Al<sub>25</sub> [257]). For reference, the newly added data are fitted to obtain the red line.

(e.g., the Cu–Zr series). Inspired by their experimental observation, we did the same fitting for the MD-simulated Cu<sub>x</sub>Zr<sub>100-x</sub> MGs ( $x = 20, 30, 46, 50, 55, 64, 70, 80$ ) [269], and the results are shown in Fig. 40. Interestingly, the data points can be nicely fitted with  $D_f = 2.658$ . Although this value is different from the  $D_f = 2.31$  in experiment, it is also smaller than three.

However, does this prove that the atomic packing in MGs is fractal, at least in Cu–Zr? The key question is, what is the physical meaning of the above power-law fitting and the extracted fitting parameter  $D_f$  – is it truly a fractal dimensionality? Let us start by considering three simpler cases. First, for an fcc structure, it is obvious that the first peak position scales with the inverse of the lattice constant ( $a$ ), while the average atomic volume scales with  $a^3$ . The  $D_f = 3$  is thus consistent with its dimensionality. Second, for a bulk amorphous structure with non-zero atomic density, we can do a thought experiment by scaling its size (with a scaling factor,  $a$ ) in the 3-D space while keeping the topology unchanged. After this simple expansion/shrinkage, the PDF should be scaled by  $a$  along the  $r$  axis, and the structure factor, according to its definition (Eq. (3)), should be scaled by  $a^{-1}$  along the  $q$  axis (so is the first peak position). The average atomic volume again scales with  $a^3$ . Therefore, in this thought experiment on an amorphous structure,  $D_f = 3$  is still expected. Third, for an fcc structure and a bcc structure with the same atomic number density (i.e., same average atomic volume), their lattice

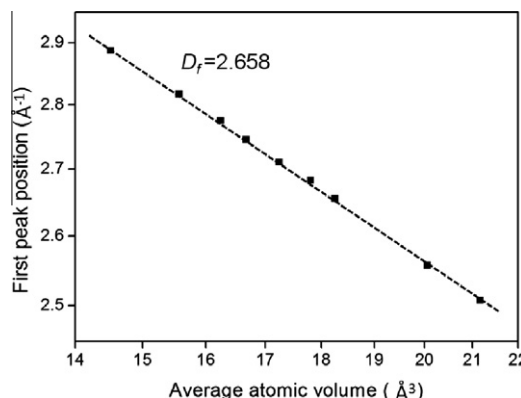


**Fig. 40.** Power-law scaling in MD-simulated Cu–Zr MGs: the first peak position in simulated total structure factor (XRD) versus the average atomic volume.

constants are different, and the positions of the first (main) peak in their diffraction patterns also differ. This illustrates that different topological structure may lead to different peak positions, even at fixed average atomic volume.

MGs with different average atomic volume can also have different topological structures, and they are not simple scaling of a fixed topology with varying atomic sizes (the latter alone should yield  $D_f = 3$ ). In other words, with the changing composition, the short-to-medium range order and atomic packing topology will also change (e.g., in the Cu-Zr MGs at different compositions [269]), and this changing topology (as well as its possible trend as the average atomic size scales up/down) is presumably the key to understand the observation of  $D_f < 3$  (i.e., why  $D_f < 3$ , instead of  $D_f \approx 3$  or  $D_f > 3$ ). In fact, since each data point in Fig. 39 may actually represent a different topological structure, the interpretation of the fitting (and  $D_f$ ) is not as straightforward as the simple examples in the preceding paragraph. What makes the situation even more complicated is the fact that the total structure factor (as measured in X-ray or neutron scattering experiments) is not solely determined by the topological structure of the MG. Instead, it is a weighted summation of all partial structure factors, and the partial structure factors are Fourier transformation of partial PDFs (see Eqs. (3) and (4) in Section 2.1.2). In this sense, partial structure factors are truly about the topological structure, whereas the total structure factor is influenced by the weighting factors, which are determined by the relative scattering amplitude of each element. The latter is not about the structure but an elemental property. Since the first peak positions in the partial structure factors of a multicomponent MG are often very different, the peak position of the total structure can be affected by the weighting factors of the partials, and thus may not fully represent the topological structure.

Based on the above discussion, it seems that more work is needed in this direction, to further justify and understand the possible fractal structure in MGs. In addition to the interpretation in reciprocal space (structure factor), an understanding of the real space fractal packing is also important. First of all, as pointed out by Coddens in an earlier debate on quasicrystals [337–339], the fractal in a dense 3-D material, if it ever exists, can only survive up to medium range, and the fractal correlation must break down over long range (otherwise the density of the material would vanish). Second, there should be a basic unit for the fractal packing, which defines the lower limit of the fractal length-scale. The basic unit could be atoms, or clusters, etc. The key to show fractal packing is the  $R^{DF}(D_f < 3)$  radial distribution of such units. Unfortunately, directly solving this  $D_f$  from the total PDF has proven difficult, as noted by Ma et al. [266].

The proposition of fractal packing in MGs is enlightening and deserves further study, with unsettled questions remaining to be answered. Besides the above-mentioned ones, how to connect it with prior models built on efficient packing of solute-centered clusters is also challenging. If the cluster packing is truly dense, assuming an fcc-like or DRP-like MRO, then we need to understand why it can also be fractal (on average) with a dimensionality significantly smaller than three. The assumption that MGs are made up of “clusters plus voids” would be inconsistent with the high packing density of MGs (only a few percent lower than the densely packed crystals with fcc or hcp structure), as well as the strong non-directional cohesion of metal atoms. However, it is possible that a sub-group (but not all) of the atoms and clusters may actually interconnect and organize themselves in a way that resembles a fractal packing. It is our opinion that more work is needed to fully resolve this puzzle and explain the fitting results when  $D_f < 3$ .

#### 4. Structure–property relationship in metallic glasses

Structure–property correlation is a central theme of materials research, and it is also the indispensable link between theory and application. The structure of a material influences its properties in different ways. For example, at room temperature the element carbon can have at least two bulk polymorphs: diamond and graphite, in which both the atomic and the electronic structures are rather different, leading to their distinctively different properties. For crystalline metals, in addition to the different phases and lattice structures (e.g., fcc, bcc, etc.), which fundamentally determine the intrinsic properties and ideal behaviors, the structural defects such as dislocations, twins, and grain boundaries often play a key role. There are many microstructural details to look into, when interpreting or

predicting the behaviors of a crystalline alloy, and there exists vast literature on the structure–property relationship in metals and alloys.

The properties of MGs also change pronouncedly when the internal structures change. Several examples have been given in Figs. 5–9, showing the consequences of the changes in composition, or variations in the processing conditions for MGs of a fixed composition. However, compared to crystals, the structure–property correlation in amorphous materials such as MGs is very difficult to study, for multiple reasons. First of all, structurally it is difficult to tell apart the various MGs. For example, HRTEM usually shows the maze pattern and no observable difference for the MGs (see Fig. 14). Second, the glass structure is difficult to describe and quantify, as amply illustrated in the last section. Third, similar to the situation with glass structure, the understanding of glass properties is also nowhere close to the level that has been achieved for crystals. As a result, quantitative prediction about how the atomic-level structures influence the macroscopic properties of MGs is rather difficult to establish.

Nevertheless, there have been considerable efforts devoted to this direction over the years, and encouraging progress has been made recently. In particular, some insight into the microscopic structural processes underlying the glass behavior, much of which has been derived from computer simulations (e.g., [63,340]), is beginning to allow verifiable predictions. This ultimately could lead to quantitative and predictive theory on various length-scales. This section summarizes and discusses the knowledge accumulated in this important area.

#### 4.1. Correlation between glass structure and thermodynamic/kinetic properties

The atomic-level structure is intimately connected with the thermodynamics of MGs and their parent supercooled liquids, as the configurational potential energy and configurational entropy are rooted in atomic bonding and structural ordering. Structure is also a major factor influencing the diffusion and structural relaxation (the relaxation time-scales with viscosity), and hence controls the kinetics of liquids/MGs. Meanwhile, the configurational entropy and the relaxation time, as we have discussed in Section 1, can be connected by the Adam–Gibbs equation. The configurational entropy is also related to the configurational potential energy for a given system [19]. As such, all the above are linked with each other, with common structural origins. The general trend is that the lower the temperature, the lower the configurational potential energy, the lower the configurational entropy, the slower the relaxation kinetics, and the more ordered the amorphous structure. In addition, different liquids/glasses may have quantitative differences in their behavior during the cooling process (such as the fragility), depending on what the controlling order is, and how and how fast it develops in the supercooled liquid to influence the evolution of thermodynamic and kinetic parameters.

##### 4.1.1. Potential energy surface description

These correlations between structure and thermodynamic/kinetic parameters are best illustrated using the potential energy surface (PES) [341]. The total system potential energy is a function of the 3-D configuration of the atoms. The PES is an analog of the topological surface, but in the multi-dimensional configurational space, as schematically illustrated in Fig. 41. On the PES, the z-axis is the potential energy of the system, and x/y-axis represents the atomic configuration, or a point in the multi-dimensional configurational space. A kinetic process of the system thus corresponds to relocation on the PES. The landscape of the PES is intrinsically rugged, and the bumps separating the neighboring basins represent energy barriers for dynamic relaxation, which, in real space, is usually observed as inelastic structural rearrangement of atoms. As the configuration evolves, the point representing the system travels on the PES following certain ensemble statistics. The temperature of the system determines which level of the PES is being sampled and surveyed. When the temperature is very high, the kinetic energy is high and the system travels around globally on the PES, thus the material is flowing and ergodic. When the system is quenched to very low temperatures, the PES becomes increasingly hierarchical, which can be depicted as megabasins consisting of subbasins [341]. The relaxation thus starts to bifurcate into megabasin migration and subbasin hopping, which correspond to  $\alpha$ -relaxation and slow  $\beta$ -relaxation (Johari–Goldstein relaxation), respectively. While the characteristic time for  $\beta$ -relaxation may stay Arrhenius following the extrapolation from the high temperature trend, the  $\alpha$ -relaxation slows down dramatically and deviates from the Arrhenius behavior [341]; the

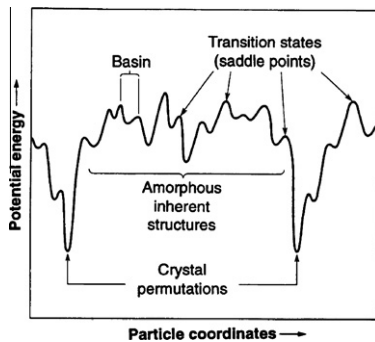


**Fig. 41.** A two-dimensional schematic potential energy surface. (Reproduced from [341] with permission © 1995 by American Association for the Advancement of Science.)

latter is primarily due to the emergence of the megabasins. For metallic liquid/glass at low temperatures, the  $\beta$ -relaxation presumably corresponds to atomic diffusion and the cooperative rearrangement of isolated atom clusters, while the  $\alpha$ -relaxation can be viewed as consisting of a series of  $\beta$ -relaxations leading to irreversible migration of the system to an independent structural state (i.e., a different megabasin on the PES) [51,342,343]. These two relaxations merge to a unified process at high temperatures [19,343]. The viscosity scales with  $\alpha$ -relaxation time, and when the temperature or kinetic energy is sufficiently low,  $\alpha$ -relaxation (or megabasin transition) is dramatically slowed down and practically prohibited [344]. The system is trapped locally in a megabasin and can no longer travel globally, thus the material appears frozen and non-ergodic. The transition process from the high temperature equilibrium liquid to the low temperature glass, the statistical details of the PES influencing the evolution of relaxation in the supercooled regime, and the exact kinetic pathway the system travels across saddle points atop the landscape, are subjects of strong current interest [19,345,346].

On the PES, the configurational potential energy is the energy of a local minimum (basin bottom), and the configurational entropy scales with the number of available basin minima at the corresponding energy level (and temperature). With decreasing temperature, both configurational potential energy and configurational entropy decrease, and their quantitative correlation represents the characteristic statistics of the PES [19]. Since the megabasin barrier scales with  $1/S_c(T)$  [24], where  $S_c(T)$  is the configurational entropy at temperature  $T$ , the effective barrier height (or the depth of the megabasins) increases with decreasing temperature and configurational potential energy.

The above PES interpretation of supercooling and glass formation is schematically shown in Fig. 42. Note that the structure, configurational potential energy, configurational entropy, effective energy barrier of megabasin, and viscosity are all correlated with each other in this dynamic process.

#### 4.1.2. Role of icosahedra in the dynamical slowdown

With supercooling the relaxation dynamics slows down, and the atomic motion is no longer as spatially homogeneous as it was in the high temperature equilibrium liquid. Specifically, within a characteristic observation time, the mobility of atoms can become very different and exhibits heterogeneous distribution in space: some atoms are mobile and move faster, while some others appear to be caged and immobile. The spatial heterogeneity of relaxation dynamics in the supercooled liquid evolves with temperature, in terms of both time-scale and length-scale. For example, at a lower temperature, the heterogeneity may last longer, and has a larger correlation length/size. The above features of dynamical heterogeneity have been extensively studied using computer simulations [347–350]. The next task is to find out whether or not the very different atomic mobility is correlated with the local atomic-level structure, which is also expected to exhibit fluctuation and heterogeneity in liquid/glass. Attempts made on hypothetical computer models [351–354] indicate that the slow particles may have lower configurational potential energy. Although these studies did not further unravel an explicit correlation between the structure motifs and the dynamics, they have provided useful tools and insights.

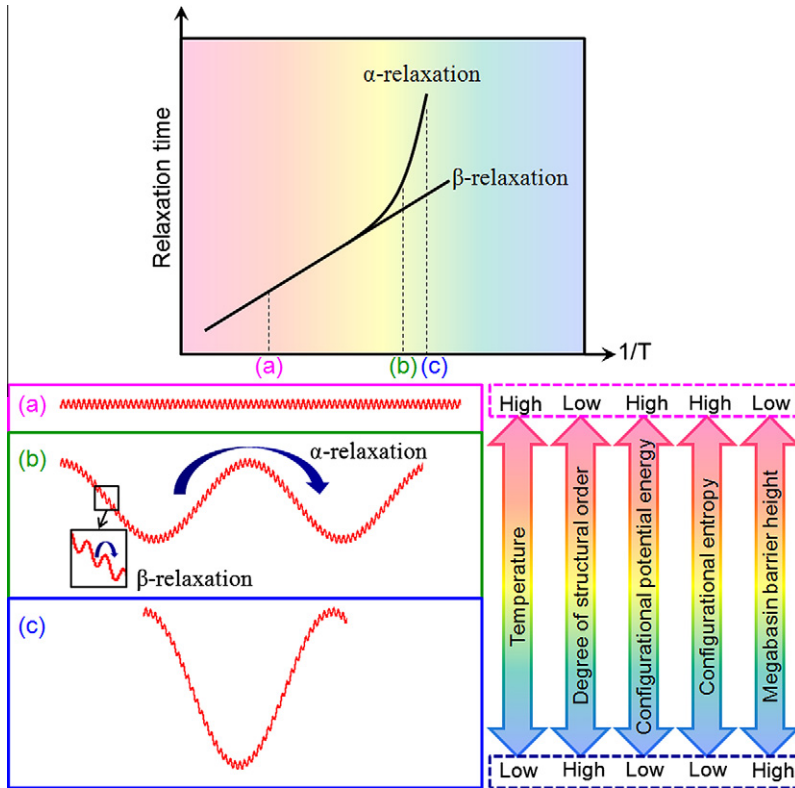


**Fig. 42.** The PES description of relaxation, glass formation, evolution of structure, and thermodynamic and kinetic parameters with supercooling. (a–c) Correspond to different levels of the PES sampled at the three different temperatures.

For monatomic metals, the topological order determines the configurational potential energy and configurational entropy. Since icosahedral order is a key feature of supercooled monatomic liquid, it is reasonable to infer that the icosahedral structure may correspond to lower configurational potential energy, lower configurational entropy, higher transition barrier for structural rearrangement, and slower relaxation dynamics. The lower potential energy of icosahedra has been demonstrated by Doye et al. for various monatomic potentials in computer simulation [181,182]. The lower configurational entropy can be attributed to the minimal disclination defects, especially for the full icosahedra with complete fivefold environment. Such a low enthalpy and low entropy structure unit is favored at low temperatures (e.g., in the supercooled liquid), and it is thus expected to have stabilizing effects on the liquid. Indeed, using the Dzugutov model potential, the non-Arrhenius dynamical slowdown [355] has been directly correlated with the increasing icosahedral order with supercooling [356,357]. Atoms embedded in icosahedra were found to have lower potential energy and lower diffusivity. Li et al. [358] simulated liquid Al using EAM potential, and they found the same correlation as observed by Dzugutov et al. in the model glass, i.e., the icosahedral SRO is responsible for the slow dynamics.

The case is more complicated for binary or multicomponent glasses. The energetically favored clusters of a binary LJ system have been studied by Doye and Meyer [313]. It is shown that by tuning the relative size of atoms, various polytetrahedral clusters including the icosahedra can be favored. Note that for binary cases, the configurational entropy is associated with not only topological order, but also chemical order. The topological order/symmetry can be measured using the Voronoi index or bond orientational order; while chemical order concerns the spatial arrangement of different species, which

may be characterized by parameters such as the partial CNs and chemical SRO parameters. In most cases the topological order and chemical order simply go hand in hand with each other, so that the most favored clusters are usually characterized by high symmetry, as well as ordered arrangement of different species [313]. In other words, better local topological symmetry in a binary or multicomponent liquid/glass is often indicative of higher local chemical order as well. Indeed, using a binary LJ potential, Jain and de Pablo [359] showed that the immobile particles in their system are characterized by icosahedral topological order, and the icosahedral clusters also have lower average potential energy than other particles.

A recent study of Cu-Zr as a typical MG (and BMG) former further highlighted the importance of icosahedral order in realistic MGs [269]. Specifically, with decreasing temperature, it is found that the fraction of Cu-centered  $\langle 0,0,12,0 \rangle$  icosahedra increases dramatically in the inherent structures of the supercooled liquid, at the expense, for the most part, of a group of odd types of polyhedra each having a low fraction, see the “all others” group (red dots) in Fig. 43. Most of these low-population polyhedra are fragmented with high disclination density, or have CNs far from the average CN as determined by the effective size ratio. They are the most unfavorable types of coordination polyhedra for this alloy, and are thus “uncomfortable”, or “unhappy”, or “liquid-like”, as called by various authors. In contrast, the  $\langle 0,0,12,0 \rangle$  full icosahedra stand out from the other types of polyhedra, as the most stable (or comfortable, happy, and solid-like) local motifs in the amorphous structure [360,361]. More discussions on the strikingly different behaviors of these two important groups of polyhedra (full icosahedra versus “unhappy” polyhedra) will be presented in later sections.

By comparing the evolution of potential energy, viscosity, and structure during quenching of a  $\text{Cu}_{64}\text{Zr}_{36}$  MG, it is then tempting to believe that the non-Arrhenius increase of relaxation time and the decrease of potential energy are due to the dramatically enhanced icosahedral order (represented by Cu-centered  $\langle 0,0,12,0 \rangle$  clusters) in the liquid inherent structure. In other words, the development of icosahedral order in  $\text{Cu}_{64}\text{Zr}_{36}$  is the structural origin of its dynamical slowdown; see Fig. 44 for an illustration of this correlation. Note that the  $T_g$  in computer simulation (cooling rate  $\sim 10^{11}$  K/s) seems to correspond to a critical relaxation time of 10 ns, as indicated in Fig. 44. This implies that the simulated glass retains a structure with much less structural relaxation and ordering than the laboratory-made glass. This discrepancy, however, does not refute the observed evolution and correlation between structure and dynamics.

The controlling role of  $\langle 0,0,12,0 \rangle$  icosahedra can be directly demonstrated by their influence on the local atomic mobility, as shown in Fig. 45. Specifically, the majority of particles in the immobile regions are found to be associated with the  $\langle 0,0,12,0 \rangle$  icosahedra, while the fraction of  $\langle 0,0,12,0 \rangle$  icosahedra is minimal in the mobile regions. It is also confirmed that the Cu-centered  $\langle 0,0,12,0 \rangle$

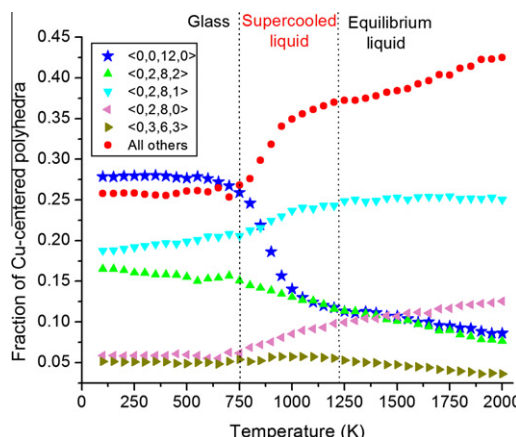


**Fig. 43.** Evolution of Cu-centered polyhedra in the inherent structures of a  $\text{Cu}_{64}\text{Zr}_{36}$  supercooled liquid [361]. Note the opposite evolution trends for full icosahedra and the uncomfortable polyhedra (all others).

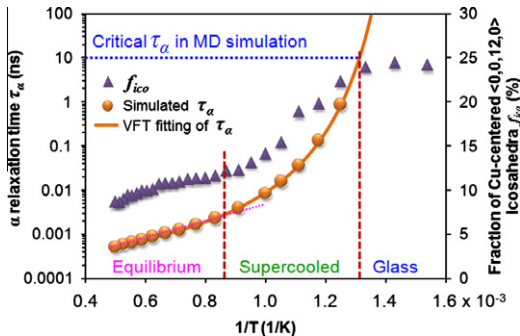


**Fig. 44.** Evolution of relaxation time and fraction of Cu-centered icosahedra in the inherent structures of Cu<sub>64</sub>Zr<sub>36</sub> supercooled liquid [269]. The left and right vertical dashed lines mark the onset temperature for deviation from the Arrhenius behavior and the glass transition temperature in MD simulation, respectively. There is evidently a strong correlation between the dynamical slowdown and the development of full icosahedra in the supercooled liquid.

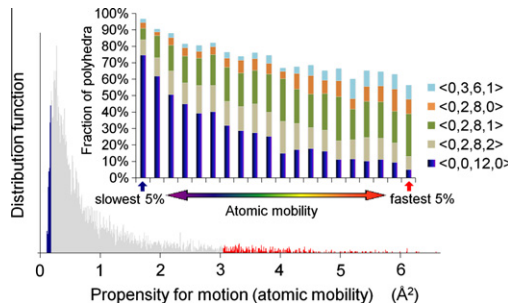


**Fig. 45.** Distribution of atomic mobility (propensity for motion) of Cu in Cu<sub>64</sub>Zr<sub>36</sub> (at 800 K). Left end (blue) area and right end (red) area mark the 5% Cu atoms with the lowest and highest mobility, respectively. In the inset, the Cu atoms are sorted by their atomic mobility from low to high and then divided into 20 groups, each containing 5% of the total Cu atoms. In each group, atoms are categorized by their local structural environment (Voronoi indices of the Cu-centered coordination polyhedra). (Reproduced from [269] with permission © 2008 by American Physical Society.)

clusters have lower average configurational potential energy than other clusters, which corroborates the precipitate drop of the configurational potential energy (i.e., the increase of  $\Delta c_p$  in Fig. 3) along with the development of the icosahedral order. In short, the degree of <0,0,12,0> icosahedral order and its evolution with cooling appears to be the structural signature of the thermodynamic and kinetic behaviors of Cu<sub>64</sub>Zr<sub>36</sub> supercooled liquids.

For comparison purposes, a Cu<sub>20</sub>Zr<sub>80</sub> liquid was also simulated, where the dominant structure around Cu is not the <0,0,12,0> icosahedra. In absence of these icosahedra, the relaxation in Cu<sub>20</sub>Zr<sub>80</sub> is much faster than in Cu<sub>64</sub>Zr<sub>36</sub> at the same supercooling temperature, and the distribution of atomic mobility is also less heterogeneous. Moreover, no particular Voronoi polyhedra are found to be significantly slower than others [269]. The lack of obvious stabilizer with certain local structure explains the faster relaxation and more homogeneous distribution of atomic mobility in this alloy. As the composition changes from Cu<sub>20</sub>Zr<sub>80</sub> to Cu<sub>70</sub>Zr<sub>30</sub>, the fraction of icosahedra increases rapidly (Fig. 28), and the relaxation dynamics of the supercooled liquid (at fixed  $T$ ) also slows down. Note that such a trend is not monotonic, because at even higher Cu concentration (e.g., Cu<sub>85</sub>Zr<sub>15</sub>), the fraction of icosahedra and relaxation time both decrease [269], reversing the trend. This indicates that the coupling between the structure and dynamics is intrinsic and not merely following the rule of mixtures. In Section 3, we have mentioned that the <0,0,12,0> icosahedra are special structurally among the various motifs, and now it is shown that they are also unique in controlling dynamical relaxation properties (they also

have a special role in influencing atomic-level stresses and shear transformations under applied stresses, which will be illustrated later). The Cu-centered  $\langle 0,0,12,0 \rangle$  icosahedral cluster can thus be regarded as the featured and functional structural unit in Cu-Zr MGs.

The above discussion focused on the topological SRO (the icosahedra) and its effects on stabilizing the supercooled liquid. The chemical SRO and its evolution during quenching can be studied by calculating and monitoring the chemical SRO parameters of the liquid inherent structures. The evolution of Warren-Cowley chemical SRO parameter around Cu shows that the Cu-centered clusters in Cu<sub>64</sub>Zr<sub>36</sub> glass have slightly more unlike (Cu-Zr) bonds than those in the inherent structure of high temperature liquid, as the parameter gradually changes from -0.32 to -0.34 with supercooling. Therefore, the chemical SRO around Cu is also improving with quenching, although the change seems not as pronounced as the topological SRO.

In general, the combination of topological and chemical order in the Cu-centered icosahedral cluster leads to its unusual stability, which peaks at the global composition around Cu<sub>70</sub>Zr<sub>30</sub> (in MD simulation). The main topological feature of the stabilizer is the complete fivefold environment with the  $\langle 0,0,12,0 \rangle$  Voronoi index. Similar simulations modeling the structure-dynamics correlation in Cu-Zr have also been conducted by Jakse and Pasturel [362], Mendelev et al. [363], Peng et al. [364], Hao et al. [365], employing *ab initio* or classical MD. Their results all corroborated the correlation found for this amorphous system between the dynamics (or diffusivity) and the icosahedral order [269]. Peng et al. [364] and Hao et al. [365] further examined the relaxation dynamics from the perspective of Zr-centered clusters, and they noticed that the Zr-centered clusters in the slow regions also contain high density of fivefold bonds (with Voronoi index of  $\langle 0,1,10,4 \rangle$  or  $\langle 0,1,10,5 \rangle$ ). Presumably, the low disclination density, represented by either Cu-centered  $\langle 0,0,12,0 \rangle$  or the Zr-centered  $\langle 0,1,10,4 \rangle$  or  $\langle 0,1,10,5 \rangle$  (Section 3.7.1), is the common feature of the immobile regions in the Cu-Zr liquid/glass.

By alloying Cu-Zr with a few percent of Al, one obtains Cu-Zr-Al ternary BMG with much better GFA and very different properties. The structural changes induced by Al alloying has been discussed in Section 3: Al addition dramatically enhances the fivefold environment and fractions of both Cu-centered and Al-centered  $\langle 0,0,12,0 \rangle$  icosahedra. Computer simulations further show that the icosahedral order develops in the supercooled regime at very different rate (much steeper rise in Cu-Zr-Al, Fig. 46), and the relaxation dynamics is significantly slowed down (by over one order of magnitude at 800 K) due to 7 at.% of Al alloying. Moreover, Al addition appears to change the fragility, making the Cu-Zr-Al ternary liquid stronger than Cu-Zr binary liquids, see Fig. 47 [366]. These observations provide a microscopic explanation of the strong alloying effects of Al on the liquid/glass properties, from the structural perspective.

The role of icosahedra in some metallic liquids has also been demonstrated in experiments. Kelton et al. [304] showed that the icosahedral order increases with supercooling in a Ti<sub>39.5</sub>Zr<sub>39.5</sub>Ni<sub>21</sub> liquid,

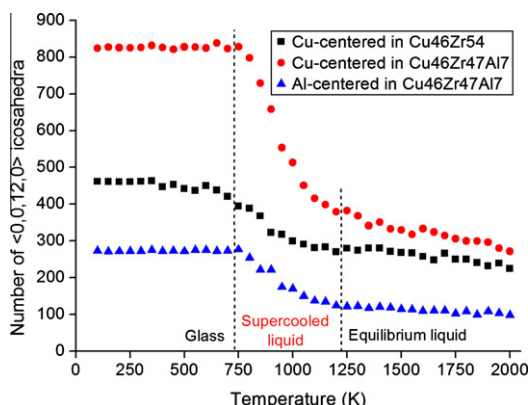


**Fig. 46.** Evolution of inherent structures characterized by the development of  $\langle 0,0,12,0 \rangle$  icosahedra in Cu<sub>46</sub>Zr<sub>54</sub> and Cu<sub>46</sub>Zr<sub>47</sub>Al<sub>7</sub> supercooled liquids [366].

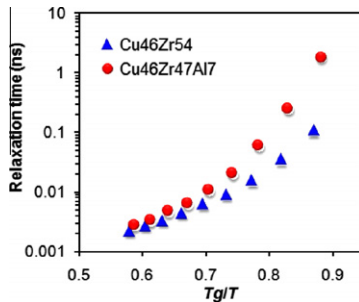


Fig. 47. Angell's plot for Cu<sub>46</sub>Zr<sub>54</sub> versus Cu<sub>46</sub>Zr<sub>47</sub>Al<sub>7</sub>, indicating different fragility of the two alloys [366].

and the increasing icosahedral order results in the crystallization to an icosahedral quasicrystalline phase, rather than the stable hcp C14 Laves phase. Since the driving free energy favors the latter, the preferential formation of the metastable icosahedral phase indicates its smaller nucleation barrier, which can be explained by the structural similarities and small interfacial energy between the liquid and the icosahedral phase. Specifically, because the icosahedral cluster is an essential building block of the icosahedral quasicrystal, the existence of these clusters in the liquid (at an appropriate concentration, see Section 3.6) would greatly facilitate the nucleation and growth of quasicrystals [367]. Lee et al. [368], by comparing various crystal and quasicrystal forming compositions in Ti-Zr-Ni, found that the quasicrystal-forming ones have smaller undercooling. The contrast shows that the icosahedral phase indeed has a low nucleation barrier and a low interfacial energy compared to the other competing crystalline phases, indicating icosahedral order in Ti-Zr-Ni liquids. Shen et al. [305] quantitatively measured the time-dependent nucleation rate in a Zr-based BMG-forming liquid, as well as its increase with supercooling. The evolution of icosahedral order was also demonstrated using RMC fitting. The direct comparison provides an experimental link between the icosahedral order and thermodynamics/kinetics of the supercooled liquid, and also lends support to the trend predicted in computer simulations.

The (heterogeneous) nucleation may also be significantly influenced by the solid–liquid interface [369]. A recent example is given by Schulli et al. [370], who showed that the supercooling of Au-Si eutectic droplets can be enhanced by Si substrate. Specifically, they found that the Au-induced (6 × 6) reconstruction of the Si (111) surface and the pentagonal arrangement of Au atoms at the interface can stabilize the liquid phase, leading to deep supercooling. This is thus another example demonstrating the role of icosahedral order in supercooled liquids.

#### 4.1.3. Non-icosahedral metallic glasses

Although icosahedral order is quite general in metallic liquids/glasses, there are many examples for which icosahedra are not the dominant structure, such as the LTM–NM and Al-rich systems. As discussed in Section 3, the SRO in these cases is presumably the Z clusters, with the favored CN determined by the solute–solvent size ratio, and the MRO could be viewed as a dense packing of the Z clusters. The structure–property relationship in these cases has not been systematically studied yet. However, since the structure can be described as efficient packing of solute-centered quasi-equivalent clusters, the stability of the clusters and the efficiency of the MRO are expected to play a key role. Specifically, the regular Z clusters and their efficient packing in medium range are likely to constitute the relatively stable/immobile regions, while distorted clusters and extrinsic disclinations are potential sources of instability. Recently, Pedersen et al. [371] simulated a binary LJ system which is known to form A<sub>2</sub>B Laves phases upon crystallization, and showed that the formation of regular Frank–Kasper clusters and their connection over intermediate range are responsible for the dynamical slowdown. The results are very similar to what was discussed above for icosahedra as the controlling clusters. It was further shown that the slow clusters are similar to those appear in the crystallized product, indicating that they are the energetically favored SRO in this system. Since their MD model resembles

the case for some LTM–NM MGs, it presumably reflects the structure–property correlation in MGs characterized by non-icosahedral Z clusters.

The above information suggests that while in some MGs the icosahedra, which are structurally different from typical crystalline units (fcc, hcp, etc.), stabilize the liquids, in other MGs some preferred local structural unit(s) other than the icosahedra, sometimes even similar to the competing crystal can also play the role of stabilizer. A question naturally arises as to how this is possible and whether the GFA is necessarily associated with the structural similarity (or disparity) of SRO between the glass and the competing crystal. So far we have emphasized that the icosahedral order is the basis of supercooling for monatomic metals, and it is also the structural origin for various properties of Cu–Zr and related MGs. However, this is not the whole story. Some glasses (e.g., LTM–NM MGs, or silica glass) with good GFA may have SROs in liquid/glass that are very similar to the local motifs in the competing crystal. In these cases, the different MRO is expected to be the main structural feature that distinguishes the glass and crystal. For example, the Ni<sub>3</sub>P crystal (bct structure with  $a = 8.952 \text{ \AA}$ ,  $c = 4.388\text{\AA}$ ) [319] has a complicated arrangement of atoms in the unit cell. Examining the P sublattice and the distribution of neighboring P atoms around a central P, one finds the following P–P CNs and distances: four P at 3.49 Å, two P at 3.71 Å, one P at 3.83 Å, two P at 4.38 Å, and two P at 4.39 Å, for a total of 11 P (the next P–P distance is 5.25 Å). In comparison, in the amorphous Ni<sub>80</sub>P<sub>20</sub> the P-centered quasi-equivalent clusters are packed in an icosahedral-like order, and the P–P distance ranges from 3.3 to 4.7 Å, with each P-centered cluster having 12–13 neighboring ones [152]. In this alloy, therefore, the MRO is different for the glass and the crystal. There appears to be a higher local cluster packing efficiency in the MG, and the crystalline structure is more complex (and thus kinetically less competitive). This may be the structural feature that matters, in promoting the GFA. A similar line of argument was put forward by Egami et al. [222].

An interesting observation is that for MGs with non-directional metallic bonds (e.g., ETM–LTM, AM–LTM), icosahedral order is often representative, while for MGs involving some degree/character of covalent-like bonds (e.g., LTM–NM, Al-rich), the local SRO is more likely to resemble the competing crystals (as proposed in Gaskell's stereochemical model). In the former case, the stable icosahedral SRO with complete fivefold environment is incompatible and in fact competes with the crystalline order, and this is the main reason for the dynamical slowdown and nucleation barrier. In the latter case, the stability of liquid may originate from certain degree of covalent-like bonding in the solute-centered Z clusters, as well as their efficient packing over medium range. The nucleation rate may be reduced by the very different and less competitive MRO in the crystalline structure. In either case, it is the energetically favored local atomic clusters that serve as the kinetic stabilizer of the liquid [372], and the heterogeneous distribution of these clusters (i.e., fluctuation of structural order) leads to the dynamical heterogeneity [373]. Note that in addition to the intrinsic structural heterogeneity, chemical heterogeneity in multicomponent systems is also expected to induce dynamical heterogeneity, and an example has been shown by Fujita et al. [374].

#### 4.1.4. Physical basis for the classification of metallic glasses

In Section 1 we have classified the MGs into four binary prototypes: LTM–NM, ETM–LTM, SM–RE, AM–LTM. Almost all alloys with good GFA so far are found to fall into one of these categories. It is thus of interest to find out what these combinations have in common, and what makes them suitable for glass formation, from the structural, thermodynamic, and kinetic perspectives.

The polytetrahedral packing suffers from frustration, for identical atoms. But appropriate size mismatch of atoms at appropriate composition can relieve the frustration [313]. The Z clusters are stabilized by tuning the effective size ratio to the magic numbers [324] for efficient packing, and at the same time, disclinations required for space tiling are carried by Z clusters with CN ≠ 12. As a result, the glass structure with more than one atomic size can achieve higher packing efficiency and stability than that with identical atoms only [375,376]. The requirement of size mismatch is automatically satisfied when we select elements from different groups in Table 1, such as the four binary prototypes. Meanwhile, most combination pairs in these binary prototypes have negative heat of mixing, and the example for ETM–LTM is given in Table 3 (for other pairs, such as Al–RE and LTM–NM, see Refs. [14,295]). The resulting attraction in the liquid allows the two elements to effectively mix at atomic level. The high packing density and strong chemical affinity between the prototype pairs lead to

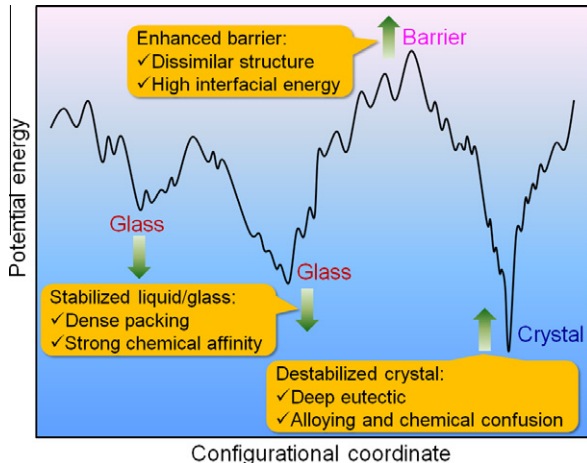


**Fig. 48.** Influences of the internal structure, for example the structural ordering, on the thermodynamic and kinetic properties of MG-forming liquids, as well as on the GFA. Green arrows point to the direction of the energy change towards better GFA.

low potential energy and high stability of the SRO clusters, and these favored SRO clusters may compete with intermetallic compounds, prolong the structural relaxation time and enhance the viscosity, as reviewed above. The prototype combinations are thus a manifestation of the structure–property correlation in MGs, and the current discussion from the structural perspective is in line with Inoue's empirical rules for BMG formation [6] and earlier studies by Polk et al. [377].

Based on the binary prototypes, one may modify the structure and properties by adding more alloying elements. Elements either from the existing group or from other groups can be considered. From the structure perspective, the alloying elements may induce chemical heterogeneity [227,229,290], destabilize competing crystals [222], and lead to more efficient medium-range packing by diversifying the clusters [93,221,322]. The effects of minor alloying on structure and various properties of MGs, especially the GFA, have been reviewed by Lu and Liu [378] and Wang [379].

To summarize, the effects of the atomic-level structure on the thermodynamic and kinetic properties, as well as the resulting impact on the GFA, are schematically illustrated in Fig. 48. Taking Cu–Zr (–Al) as an example, one can explain the GFA following the leads from the structural perspective. The efficient packing of Cu and Zr atoms and their negative heat of mixing stabilize the supercooled Cu–Zr liquids; the deep eutectic in the Cu–Zr phase diagram means that the stable liquids are rather competitive relative to the intermetallic compounds; the icosahedral order with fivefold environment is quite different from the competing crystals with long-range translational symmetry, leading to high interfacial energy and nucleation barrier; alloying with a few at.% of Al destabilizes the binary competing crystals, and further enhances and stabilizes the icosahedral order in liquid by topological and chemical effects. All these contribute to the excellent GFA of Cu–Zr, and the even better GFA of the ternary Cu–Zr–Al.

#### 4.2. Correlation between structure and mechanical properties

As we have introduced in Section 1, MGs have unique mechanical properties, represented by their high strength and lack of ductility. These properties are also sensitively dependent on the composition and processing history, much like the case for crystalline alloys. For crystals, to explain their deformation behavior and dependences on sample composition and processing history, one looks into the “microstructure” of the material. The microstructural features are abundant and distinctive, including phases in various amounts and morphologies, precipitates and interfaces, grains and their size distributions, and crystalline defects such as dislocations, stacking faults, and twins. All these no longer exist in monolithic MGs. A typical high-resolution TEM image, of an Al–La–Ni MG as an example, has

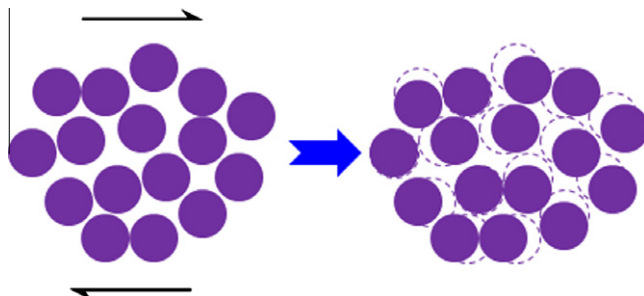


**Fig. 49.** A schematic illustration of STZ in MGs that undergoes shear transformation under stresses.

been given in Fig. 14. Changes in sample composition and/or processing history during cooling and aging do not lead to noticeable changes in the image, but can affect the MG properties dramatically.

The elementary carrier of the stress relaxation processes in MGs is the shear transformation involving a group of atoms in an STZ [70] (Fig. 49). However, unlike the carrier (i.e., dislocation) for crystalline plasticity, which can be unambiguously characterized in a TEM, the structure and evolution of STZs cannot be easily observed and quantified. In fact, STZs cannot be precisely identified in advance before the application of the external stimuli (such as stresses), and the atoms involved change, in response to different stress tensor. Also, the energy barrier of dislocation motion is a characteristic value that can be solved and used for modeling, but the activation barrier of STZ is likely to have a broad distribution. Some very unstable regions may be activated as STZs even in the nominally elastic region. This leads to the question about yield criterion, for which the answer is still not clear in MGs. It is generally believed that the formation of shear band is the cause of yielding and catastrophic failure, but the shear banding process is an avalanche and self-propelling event of STZs involving a wide span of time- and length-scales, which is rather difficult to study. Despite the complexity, recent research has established qualitative connections between the local structure and the above mechanical behaviors in MGs, and the results will be summarized in this section. The structure–mechanical property correlation would help to understand the existing constitutive models, and to provide insights into the micromechanisms that would facilitate future efforts in establishing the deformation theory of amorphous metals.

#### 4.2.1. Structural fluctuation and mechanical heterogeneity

Since the MG structure has intrinsic fluctuations, the local atomic-level structure varies from site to site. The various local structure motifs contained in the MG, their relative fractions, and how they distribute in space should significantly influence the mechanical response of the macroscopic sample under loading. In other words, the structural heterogeneity necessarily leads to mechanical heterogeneity, and these heterogeneities are inherited from the supercooled liquid (see Section 4.1), where the time- and temperature-evolving spatial heterogeneity (both structural and dynamical) is now frozen and becomes static in the glass.

Similar to the mobile and immobile regions in the supercooled liquid, there are also regions with low and high local stiffness in MGs. The stiffness fluctuation is demonstrated by the non-affine elastic field under shear, and has been directly characterized in computer simulations by Yoshimoto et al. [53], Tsamados et al. [50], and Mayr [51]. Recent experiment [380] has confirmed the nanoscale stiffness fluctuation in a Zr-based BMG. The idea has also been applied to study MG behaviors using continuum method, such as the coarse-grained model by Demetriou et al. [381].

Accompanying the local stiffness, the local structural stability, or local energy barrier for structural relaxation, is also inhomogeneous in MGs. In general, the low stiffness regions are more unstable and tend to become preferential sites for localized inelastic deformation. These are thus fertile sites for shear transformations, or potential STZs, which corresponds to the localized shear observed in early computer simulations by Srolovitz et al. [52], Bulatov and Argon [382], Deng et al. [383], Falk and

Langer [75], and others. Recently, the local activation barrier for structural rearrangement and its heterogeneous distribution has been directly characterized by Rodney and Schuh [384].

Both local stiffness and local stability may have their origin in the local structure, and computer simulation is an excellent tool in revealing the correlations that are not possible to visualize in current laboratory experiments. The interplay of SRO and mechanical behaviors in model glasses has been systematically studied by Falk and co-workers [79,340,385–390]. For example, in the unstable and energetic shear band, they found depletion of SRO, as shown in Fig. 50 [390]. More of their results will be discussed later in this section.

Meanwhile, the effect of icosahedral order on the deformation behavior of realistic Cu-Zr-based MGs has been studied by Lekka et al. [391], Lee and co-workers [63,273], Wakeda et al. [274,392], and Cheng et al. [270,361]. It has been demonstrated that the icosahedral order in Cu-Zr(-Al) corresponds to higher local stiffness and yield resistance (stability), while shear transformation preferentially nucleates from more disordered regions where the local stiffness and stability are low, as illustrated in Fig. 51.

The observation in Cu-Zr can be generalized to other non-icosahedral MGs, where the density of extrinsic disclinations, based on previous discussions in this review, is expected to serve as the structural indicator of local stability; the case for Cu-Zr is just one example, with Z12 being the favored Z

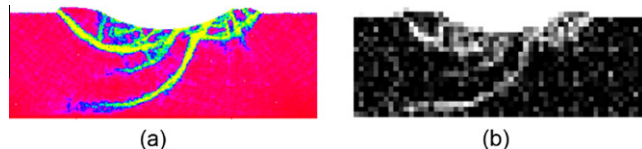


**Fig. 50.** Correlation between shear band formation (a) and destruction of SRO (b) in a simulated nanoindentation test. The characteristic SRO is depleted (white in (b)) in the shear band (yellow in (a)). (Reproduced from [390] with permission © 2007 by Elsevier.)

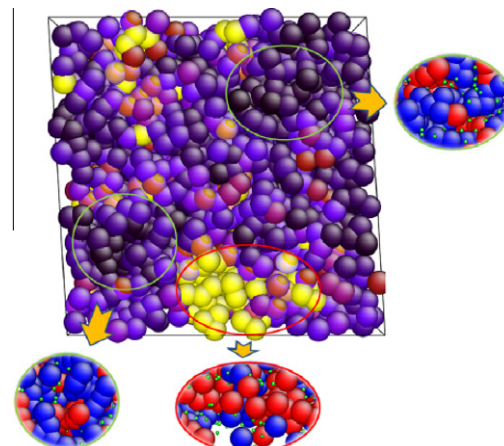


**Fig. 51.** Correlation between icosahedral order and local plastic deformation (STZ). The figure shows the cross-section of a sheared Cu<sub>64</sub>Zr<sub>36</sub> sample. For clarity, only Cu atoms are shown, representing the Cu-centered clusters. The colors are mapped to the various levels of plastic atomic strains (the non-affine strain defined in [75]). The dark purple regions are only elastically deformed while the yellow ones have been involved in shear transformations (in an STZ). Two elastic regions and one STZ are circled out and their local structures are shown in the insets. For the elastic regions, the Cu atoms are mostly in ⟨0,0,12,0⟩ icosahedra (such Cu are colored blue), which are well percolated, while in the STZ, most Cu atoms are embedded in unstable, “fragmented” (i.e., liquid-like) polyhedra (colored red). Cu atoms embedded in other regular polyhedra are shown with much smaller green dots. (Reproduced from [270] with permission © 2008 by Elsevier.)

cluster. A direct demonstration of the general correlation between extrinsic disclination density and the local mechanical properties, however, is awaiting future study. With the microscopic correlation between local structure and local deformation tendency, we can now discuss in various macroscopic mechanical behaviors and their origin in the atomic-level structure. It should be first noted that the local structure and deformation response are coupled only in a statistical sense. Under stresses, regions with similar local structure would not necessarily respond the same way and at the same time. Under the long-range stress/strain field in solids, the relationship between local structure (particularly the SRO) and the deformation behavior cannot be treated as a deterministic one-to-one correspondence. Also, a monolithic glass is a uniform body that cannot be simply interpreted as a composite of well-defined grains (regions) with boundaries.

#### 4.2.2. Shear modulus and elasticity: percolation of rigidity

We first discuss the elastic response of MGs. Given the continuous fluctuation of structure and properties in MGs, a plausible picture for the MG elasticity is to treat the percolated rigid (with high shear resistance) structural units as the elastic backbone that supports the entire matrix, and the floppy and unstable regions as embedded “inclusions”. This description is very similar to the percolation of rigidity in covalent glass proposed by Thorpe [393], where structure units with different rigidity have very different CNs. The differences among the various local structures in MGs, however, may be more subtle and need additional structural parameters to distinguish, as shown in Section 3. The rigid units can sustain large shear stress, so that their percolation in the 3-D space yields the shear resistance and shear elasticity of MG matrix. This idea has been examined and validated in simulations by Shi and Falk [340,389], as well as experiments by Harmon et al. [394] and Dmowski et al. [44]. Recently, observations in a colloidal glass have directly confirmed that the slow clusters and their percolation contribute to the bulk elasticity [395]. The role of the elastic backbone in MGs is also revealed by the spatial and temporal coupling of atomic-level shear stresses over medium-to-long range [396]. It is found that with more rigid structural units and higher degree of percolation, the medium-to-long range correlation of atomic-level shear stresses is stronger, suggesting that the elastic backbone is better established throughout the matrix, and the shear resistance of the MG is enhanced.

The mechanically unstable regions, in contrast, are the carriers of local inelastic deformation while the backbone is sheared elastically. The presence of such “inclusions” is partly why the shear modulus of MGs is smaller than that of the corresponding crystals. The inelastic nature and damping effects of these inclusions under cyclic agitation are also likely to be the origin of the internal friction [54–57] and the softened transverse phonons [58] in MGs. Recent work suggests that they may also be responsible for the widely observed boson peak [397,398].

Computer simulation of Cu-Zr [135] shows that the icosahedral clusters tend to aggregate and connect with each other in the supercooled liquid region, forming strings and networks. Since the icosahedra have been demonstrated to be the rigid structural unit in Cu-Zr [269,270], such a structural evolution is thus an example showing how the rigidity percolation works during the formation of MGs. In fact, Mayr [51] extended the idea of rigidity percolation to explain the glass transition, which can be interpreted as the critical percolation of rigid/stable unit with supercooling.

#### 4.2.3. Yielding: percolation of shear transformation zones

When the MG is sheared elastically, the local inelastic deformation of the inclusions (shear transformations in separated STZs) is confined. The STZs are scattered and embedded in the matrix, which is supported by the elastic backbone. As long as the isolated STZs do not percolate to penetrate a sizable length-scale, they can be reversed upon unloading, under the back-stress from the backbone [394]. However, if the shear stress/strain is so large that more and more unstable inclusions are activated to connect with each other, creating a critically unstable area/region, the elastic backbone will be penetrated and give way to irreversible macroscopic strain. At room temperature, when the unstable region reaches a critical size, it will quickly extend in a localized manner, leading to instability and eventually catastrophe, i.e., STZs have percolated to form shear bands. The percolation of individual STZs has been directly observed in a recent experiment on colloidal glasses by Schall et al. [73], and the mechanism and process of shear band formation have been studied by several authors using computer simulations. For example, Shimizu et al. [72] used simulations to study the yielding of MGs. For

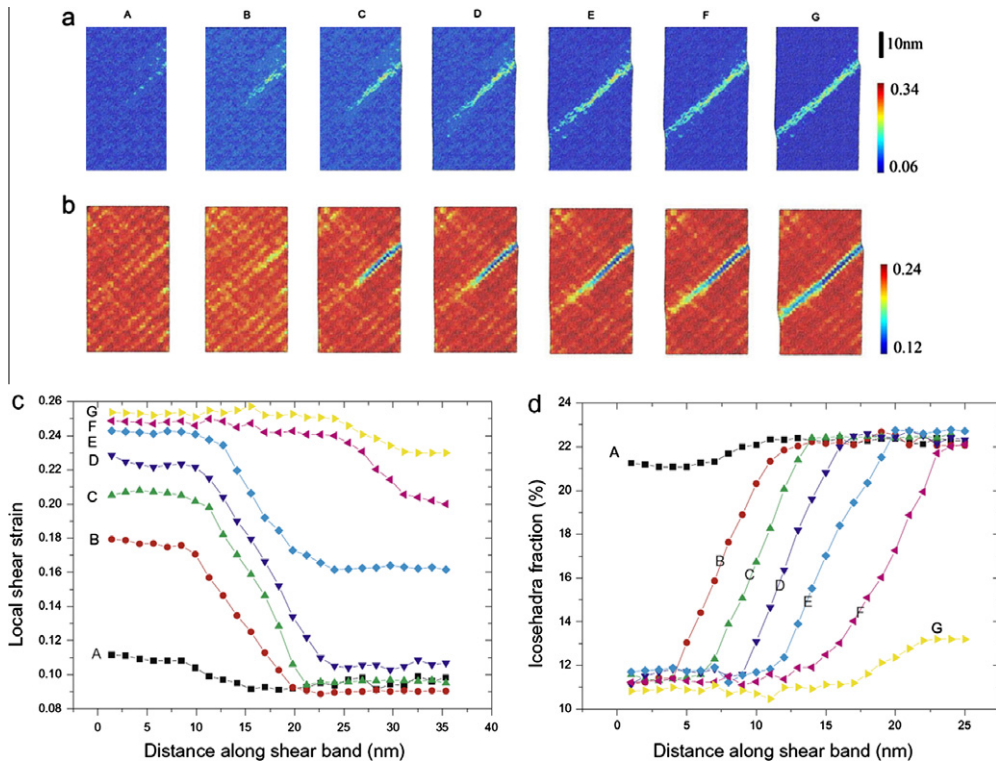


**Fig. 52.** Structural processes of shear band formation in a simulated Cu<sub>64</sub>Zr<sub>36</sub>. (a) Formation of shear band as depicted using atomic strain. (b) Formation of shear band as depicted by the density of icosahedra. The correlation between the shear band region in (a) and (b) is obvious. (c) and (d) Percolation of STZs, with destruction of icosahedra (reduced icosahedra population inside, to penetrate the elastic matrix (backbone) along the shear band/plane. (Reproduced from [403] with permission © 2009 by Elsevier.)

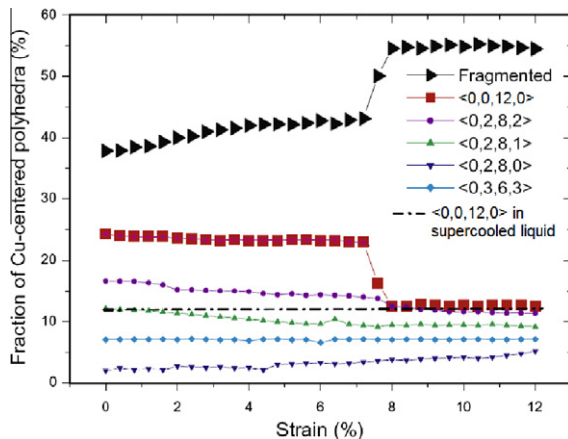


**Fig. 53.** Evolution of all Cu-centered polyhedra inside the shear band, showing the destruction of (0,0,12,0) icosahedra into fragmented (unstable) polyhedra. (Reproduced from [403] with permission © 2009 by Elsevier.)

an MG sample containing imperfections (e.g., a surface notch), STZs were found to be preferentially nucleated around these stress concentrators under the local high stresses, creating rejuvenated and softened regions. The critical size of these unstable regions for mature shear band to develop was then estimated. It was proposed that the percolated STZs at a size of ~100 nm along the maximum shear direction could be enough to trigger the avalanche and run-away instability. The results also imply that if the sample dimension is reduced to below the critical length-scale of 100 nm, development of mature shear band may be suppressed, and more plasticity may be observed.

The length-scale effect has been a recent focus of MG research. Experimentally, samples as small as a few hundred nanometers have been tested in compression [66–68] and tension [65,69], and they all show controllable plastic deformation different from their bulk behavior. However, this observation alone does not necessarily mean a completely different deformation mode or the absence of shear banding. Indeed, some experiments always observed shear bands even when the sample is as small as 250 nm [67,68]. What has been observed is that the shear bands formed are of a different type, they are cold, slide relatively slowly and do not have catastrophic consequences, especially when the sample size is very small (e.g., submicron-scale) [399–401]. Such non-catastrophic shear bands led to observable contributions from the spread-out shear transformations all over the sample, leaving the impression of “homogeneous” deformation. Recent tensile experiments have shown necking in ~100 nm samples [65,69]. Plastic deformation by necking in tension has also been observed in computer simulations, which may be favored by the small MD sample size, as well as the high fraction of “liquid-like” (see Section 4.2.4 below) regions in the sample as a result of the superfast MD quenching rate [270,402]. Indeed, in larger samples obtained with slower MD cooling, shear band emerges instead [403]. Li and Li simulated the deformation of samples with different sizes, and found that the critical size to develop shear band in their case is a few tens of nanometers [404]. Recent simulations by Shi reveal that relaxation of the free surfaces may also influence the deformation mode in nano-scale samples, and shear band formation prevails until the sample size reaches the length-scale (~10 nm) of the shear band itself, in MD samples with relaxed surfaces [405]. It should be noted, however, that due to the dramatically different cooling rate (material state) and strain rate (deformation kinetics), it is not clear if the MD simulated critical length-scale can be directly used to explain experimental observations.

While the ongoing debate on the length-scale and time-scale effects on shear band formation remains unsettled, the MD simulations by Shi and Falk [389,390] and by Cao et al. [403] have successfully captured the underlying structural process of yielding and shear banding, see Fig. 52 below for the simulation of Cu–Zr performed by Cao et al. [403]. The results unambiguously demonstrate the percolation of STZs, the destruction of icosahedral SRO in the advancing shear band, as well as their correlations, in a Cu<sub>64</sub>Zr<sub>36</sub> MG. The broken icosahedra in the shear band are transformed into the more unstable, fragmented clusters, as shown in Fig. 53.

As we have mentioned in the previous sub-section, percolation of rigidity is the microscopic process behind the establishment of shear modulus during quenching and upon glass transition. Yielding of the MG, on the other hand, is the reverse process of overcoming the percolated rigidity, termed as “stress-induced glass transition” by Guan et al. [62]. In either scenario, the development or deconstruction of structural order, in terms of the locally preferred atomic clusters and their spatial connection (e.g., ⟨0,0,12,0⟩ icosahedra in some Cu–Zr MGs), is the underlying structural origin, as demonstrated repeatedly in this review.

#### 4.2.4. Strain localization and intrinsic plasticity: degree of mechanical heterogeneity

The basic unit of plastic deformation in MGs is the STZ. In addition to the work mentioned earlier, the activation process of STZs in MGs has been recently simulated by Zink et al. [406], Mayr [407], and Delogu [408–410]. The STZs preferentially nucleate in the low stiffness, low stability inclusions, and in terms of structure, they are the less ordered and less energetically favored. It is thus intuitive to characterize these fertile sites for STZs as having liquid-like features. The liquid-like region and its effect on plasticity in amorphous Si has been studied by Demkowicz and Argon [411,412], and extended to understand flow in MGs [413]. Falk and co-workers [340,386] also found that more liquid-like structure favors homogeneous flow, and more solid-like structure would undergo larger softening upon yielding, which can be further connected with their higher degree of strain localization. It was then

proposed that the development and percolation of SRO significantly influence the deformation mode and shear banding.

Recent simulations [270,361] of BMG-forming Cu-Zr(-Al) using realistic EAM potentials [163] confirm that the relative fraction, spatial distribution, and property contrast between the STZ fertile sites and the as-quenched elastic backbone are directly related to the intrinsic plasticity of the MGs. For example, simulated deformation of Cu<sub>64</sub>Zr<sub>36</sub> and Cu<sub>40</sub>Zr<sub>60</sub> MGs showed very different degrees of strain localization (Fig. 54). In Fig. 54c, typical stress-strain curves for the MD-simulated Cu-Zr samples are compared. These curves in simulation are characterized by an overshoot stress followed by a steady state flow stress [72]. The overshoot stress represents the intrinsic strength of the as-quenched glass, while the flow stress represents the strength of the rejuvenated flow state. The stress drop, therefore, reflects the strength contrast between the activated STZs and the elastic backbone in the MG, i.e., the degree of mechanical heterogeneity [270]. Such stress-strain curves are not observed in experiments mainly because the simulated conditions are ideal to reveal the microscopic and intrinsic properties of the material itself, whereas the extrinsic factors in an experiment (such as imperfections in the MG sample or loading setup) usually preclude such observations [414]. It is perceivable that a larger strength contrast (higher degree of mechanical heterogeneity) implies that the strain would be more likely to concentrate in the already-sheared region (activated shear band) rather than spreading into un-rejuvenated regions. This stress drop/contrast thus reflects the tendency of strain localization during plastic deformation. The stress drop also scales with the elastic energy release upon yielding [270], which is dumped into the STZs and leads to elevated configurational potential energy and temperature, feeding the local region for additional softening. Therefore, the lower degree of mechanical heterogeneity and lower strength contrast would encourage more spread-out shear transformations throughout the sample, rendering the MG more resistant to severe strain localization and instability and more likely to sustain plastic strain. Compared to Cu<sub>40</sub>Zr<sub>60</sub>, Cu<sub>64</sub>Zr<sub>36</sub> exhibits much larger strength contrast between the elastic backbone and the rejuvenated STZs (i.e., larger stress drop in the stress-strain curve). The plastic deformation is thus heavily localized and self-propelling, leading to strains largely concentrated in one dominant shear band with obvious shear offset (Fig. 54).

The structural origin for these distinctly different behaviors is presumably the different population and connectivity of the more rigid icosahedral clusters, or conversely, those of the fertile sites for STZs. Note that for shear banding and global yielding, the icosahedral network must be destroyed (to some extent) along the shear plane (by the overshoot stress in simulation), to allow strain compatibility among neighboring regions and create a rejuvenated pathway for flow (under the flow stress). The destruction of more icosahedra in Cu<sub>64</sub>Zr<sub>36</sub> is thus responsible for the larger stress drop (higher

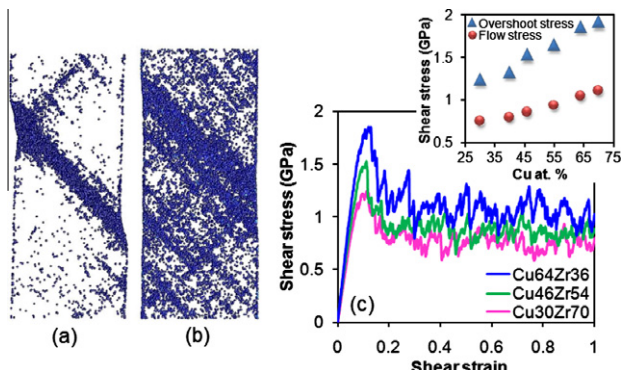


**Fig. 54.** Different degree of strain localization in simulated (a) Cu<sub>64</sub>Zr<sub>36</sub> and (b) Cu<sub>40</sub>Zr<sub>60</sub> MGs. While (a) shows an obvious shear offset associated with a dominant shear band, (b) exhibits spread-out shear transformations (blue dots). (c) The stress-strain curves and the stress drop (inset; difference between the overshoot peak stress and flow/steady stress) upon yielding of several Cu-Zr MGs, indicating different tendency of strain localization [270,361]. The difference in the structural order between these two MGs, i.e., the relative fractions of liquid-like and solid-like regions, has been illustrated in Fig. 28. Movies showing the deformation processes in (a) and (b) can be found at <https://sites.google.com/a/gmu.edu/eam-potential-database/Home/CuZr>.

strength contrast). Conversely, the fewer and less percolated icosahedra in Cu<sub>40</sub>Zr<sub>60</sub> should be the main reason for its smaller stress drop, more homogeneous plastic deformation and better intrinsic plasticity. Based on similar observations, Park et al. [415] proposed an experimentally measurable parameter, the normalized relaxation heat, as the indicator of the intrinsic plasticity. The relaxation heat quantifies the potential energy stored in the rejuvenated sample after elastostatic loading, and it essentially scales with the stress drop (strength contrast) discussed above.

#### 4.2.5. Effects of processing history: the structural differences

In the introductory section, we have shown that the mechanical properties, including the shear modulus, strength, and plasticity (toughness), are sensitively dependent on the processing history. In what follows we will discuss the structural origin of this dependence, using the microscopic structure–mechanical property correlation established above.

First of all, the processing history dependence of mechanical properties can be justified using the PES description. With slower cooling rate or annealing/aging, the amorphous configuration will be trapped at, or will roll down to, a lower configurational potential energy level, which is characterized by deeper megabasins with steeper slope. Therefore, both the shear modulus and yield stress of the glass would be higher. In contrast, at faster cooling rate or with structural rejuvenation (such as annealing at a temperature higher than  $T_g$ , followed by instant quenching), the configuration will be elevated to a higher configurational potential energy level, where the megabasins are shallower (see Fig. 42). The underlying origin, again, is the changing structural ordering with processing history.

The effects of processing history on the structure and mechanical properties have been studied by Falk and co-workers in 2-D and 3-D model glasses [340,385–390]. Specifically, by quenching the sample from different initial temperature, or at different cooling rates, different degree of structural ordering and percolation of the ordered clusters can be produced. These samples also exhibit different mechanical properties. For samples with higher degree of SRO and percolation, the strength and shear modulus are higher, with more pronounced softening upon yielding, after which the strain tends to be more localized in the shear band. The strain localization is also influenced by the strain rate, and an interesting finding is that the critical percolation of the SRO ( $k$ -core percolation) corresponds to a transition point of the strain rate sensitivity. That is, for slower cooling rate and percolated SRO, slower strain rate favors strain localization; while for higher cooling rate and insufficient percolation, slower strain rate favors homogeneous flow. In this case, not only the degree of the SRO, but more importantly, their percolation, has been emphasized to play a controlling role.

The cooling rate dependences of the structure and mechanical properties in Cu–Zr BMGs have also been studied [361]. It is found that the fraction of icosahedra in the as-quenched Cu–Zr MG sample increases considerably with decreasing cooling rate. In the meantime, the configurational potential energy of the system decreases, see Fig. 55. This is consistent with the PES description above.

On the one hand, with slower cooling rate, the increasing number of icosahedral clusters form a more extended and stronger elastic backbone, leading to the higher stiffness (shear modulus) and yield strength. On the other hand, the lower fraction of fertile sites in the slowly quenched samples and the larger stress drop upon rejuvenation make the plastic strain more easily localized, as demonstrated in Fig. 56. The above observations and conclusions in Cu–Zr are in good agreement with prior simulations conducted by Falk and co-workers [340,385,386,388,390]. These results also corroborate the strong configurational dependence of shear modulus observed in both experiments and simulations [396,416–418].

The improved SRO around each and every atom at slower cooling rate naturally leads to enhanced medium-range structural correlation, although a general description of the MRO is still lacking. In Ni–P, slower cooling rate could result in more efficient packing of the quasi-equivalent P-centered clusters; while in Cu–Zr, better spatial connectivity of the icosahedral clusters could be the observation. Lee and co-workers [419] have recently studied the effect of medium-range organization of icosahedra on the mechanical behaviors of Cu–Zr MGs, in terms of the degree of connectivity of the icosahedra. It is found that in addition to the absolute population of the icosahedra, the connectivity itself (i.e., the way icosahedra are linked and the rigidity of the connected icosahedra) also has significant influence on both local and global mechanical properties. The finding that interpenetrating connection of

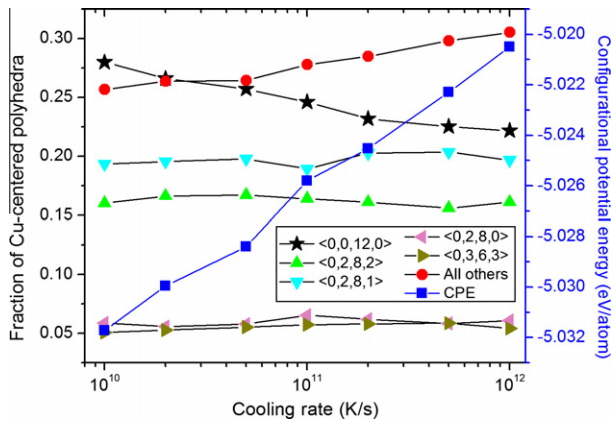


**Fig. 55.** Cooling rate dependence of the fraction of Cu-centered Voronoi polyhedral clusters, as well as the configurational potential energy (CPE) of the MGs at room temperature. Note the obvious and opposite trends of  $\langle 0,0,12,0 \rangle$  icosahedra and fragmented polyhedral (i.e., all other “liquid-like” clusters) [361].

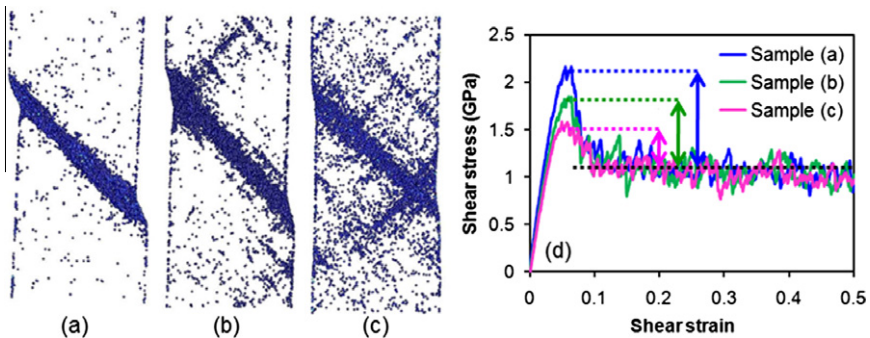


**Fig. 56.** Different degree of strain localization in simulated Cu<sub>64</sub>Zr<sub>36</sub> MGs obtained at three different cooling rates: (a)  $10^{10}$  K/s, (b)  $10^{11}$  K/s, (c)  $10^{12}$  K/s. (d) The stress–strain curves and the stress drop upon yielding of these three samples, indicating different tendency of strain localization [361].

icosahedra forms a network that resists the flow in Cu–Zr MGs corroborates previous studies and speculations [135,270,340].

In experiments, annealing or aging is a method often used for processing of the as-quenched MGs. The structural relaxation induced is essentially equivalent to that incurred during a slower cooling in sample preparation. In all cases, structural relaxation is expected to result in enhanced structural ordering, and annihilation of fertile sites (e.g., extrinsic disclinations, or interstitialcy-like defects [35,37]). Egami and co-workers have studied the structural relaxation in terms of chemical and topological structural fluctuation and ordering [315,420–423]. The annealing or aging process also has PES explanations, as discussed by Hachenberg et al. [343], Kahl et al. [424], Casalini and Roland [344], and Mayr [51]. All the above structural pictures lead to a consistent assessment: as a result of structural relaxation, the shear modulus and strength increase, while the intrinsic plasticity and toughness decrease [64,425–427].

A reverse process of the structural relaxation is the structural rejuvenation, which can be achieved by elastostatic deformation to induce homogeneous structural disordering, as recently proposed by Lee and co-workers [428–431]. This method has been demonstrated to be useful in improving the plasticity of the sample, presumably by inducing more and more homogeneously distributed structural “defects” (i.e., more disordered and liquid-like regions), and thus reducing the internal strength

contrast and tendency of strain localization. Similar structural disordering was also observed in MGs after high pressure torsion induced severe plastic deformation [432].

#### 4.2.6. Effects of chemical bonding: metallic versus covalent-like

On top of the atomic configuration, the nature of chemical bonding has additional impact on the mechanical properties. Although MGs in general are characterized by non-directional metallic bonding, certain degree of covalent-like bonding is not unusual. Examples of such covalent-like bonds include Al-LTM bond in Al-rich MGs and Cu-Zr-Al, LTM-NM bond in LTM-NM type MGs, and perhaps Be-TM bond in Be-bearing ETM-LTM type MGs. Intuitively, whereas the directional covalent bonds are more rigid and shear resistant, the non-directional metallic bonds are more flexible and deformable. This is probably why typical MGs, although macroscopically brittle, have intrinsic plasticity at the atomic level and high fracture toughness/energy (i.e., crack propagation in MGs is characterized by large energy dissipation in the form of plastic deformation at the crack tips) [64]. In contrast, covalent glasses such as fused silica are believed to be intrinsically brittle with very low fracture energy comparable to the surface energy, indicating nearly ideal brittleness [433]. Naturally, one would expect that the presence of some covalent-like bonding (or a higher degree of the covalent-like electron localization) in MGs will degrade plasticity, when compared to the more metallic counterparts with similar constituent elements and compositions but containing fewer or no covalent-like bonds. This is indeed observed by Gu et al. [434] in Fe-based BMGs with different NMs (C, B, P) and by He et al. [435] in Zr-based BMGs with different LTMs (Cu, Co, Ni) and simple metals (Be, Al). In both cases, the Poisson's ratio, often considered an effective indicator of the plasticity, is also reduced due to the presence or enhancement of the covalent-like bonding.

### 4.3. Indicators of structural state

The description of a structure–property correlation for a specific MG, as we discussed above, needs to involve one (or more) specific structure motifs, but different MGs have different characteristic local structures. As such, to establish more general correlations, one may prefer to invoke indirect parameters (such as a thermodynamic parameter) that reflect the structure but can be incorporated into (quantitative) constitutive models. Several indicators have been proposed and employed, as summarized and compared below.

#### 4.3.1. Free volume

The concept of free volume was originally proposed by Cohen and Turnbull to model the transport processes in liquid of hard spheres [436–438], for which it can be derived that the diffusivity  $D$  scales with  $\exp(-\gamma v^*/v_f)$ , where  $\gamma$  is a constant of the order of unity,  $v^*$  is the minimum excess volume needed for an atom or molecule to jump in,  $v_f$  is the free volume defined as  $\bar{v} - v_0$  ( $\bar{v}$  is the average volume per atom/molecule, and  $v_0$  is the actual atomic or molecular volume). Such an exponential scaling can describe the van der Waals liquids very well, and the fitted  $\gamma v^*$  is indeed comparable to the atomic or molecular volume. For metallic liquids, it was noticed that the temperature-dependence of diffusivity is slightly weaker than the exponential trend, but the deviation is within experimental uncertainty for most cases. However, the fitted  $\gamma v^*$  is much smaller than the atomic volume, and is usually close to the size of the ion core corresponding to the highest valence state of the metal. Moreover, the pressure dependence of the diffusivity in metallic liquids is much smaller than that in van der Waals liquids, and cannot be explained by free volume alone. These indicate that in metallic liquids, although the free volume model can still fit the experimental data, the description becomes phenomenological. In other words, unlike in van der Waals liquids where the free volume is the true underlying mechanism, the physical basis of using free volume to characterize amorphous metals may be inadequate, as pointed out again by Egami recently [153].

Despite possible limitations, the free volume concept was further employed and developed by Spaepen [77] to model the diffusion and plastic flow in MGs under different levels of external stress. The dynamic competition between creation and annihilation of free volume was shown to be the controlling factor that determines the deformation behavior. If the stress is higher than a critical value,

which is a function of temperature, free volume annihilation will not catch up with the rate of free volume creation, so that strain softening and localization are expected.

Free volume is a very simple and convenient indicator of the internal glass state. The complex local structure properties and variations are all represented by a scalar parameter – the free volume content. Indeed, flow of MGs requires dilatation [77], and disordering in the glass structure is usually accompanied by some changes in the excess volume. Despite the simplifying assumptions, many key features of the MG behaviors have been successfully reproduced by constitutive models based on the free volume description, as demonstrated by Falk and Langer [75], Demetriou and Johnson [74,439], Anand and Su [82], Spaepen [440], and many others. This is partly why the free volume parameter has been a very popular structural indicator embraced by many researchers in the MG community.

However, as we have mentioned, it is questionable if the original concept of free volume can be extended directly and literally to MGs. The modified and generalized free volume for MGs, as it was used in the above models, is more like an effective parameter representing the general liquid/glass state. It may be simple and useful for modeling purposes, but its physical meaning is not unambiguously defined. In this sense, if the goal is to physically explain an observation or a microscopic process in MGs, rather than mathematical modeling of the overall behavior, the concept of free volume may not be the final resort. Qualitative arguments ascribing everything to free volume may be misleading.

#### 4.3.2. Atomic-level stresses

The limitations of the free volume idea in MGs have been extensively discussed by Egami and co-workers [153,316,423,432]. The origin of its inapplicability is attributed to the relative compressibility of metal atoms [153]. As a result, the structural defects in MGs with low stability may not be simply due to excess volume. Egami et al. thus proposed that two types of defects should be quantified in order to describe the MG behaviors, and the topological satisfaction of local structures can be evaluated using the atomic-level stresses [153,441–449], as defined in Refs. [443,450].

Different from crystals, in MGs local structural variations and fluctuations are intrinsic so that a significant fraction of atoms are “unhappy” and relatively more unstable (i.e., in a higher-energy or unrelaxed state), see for example the ~25% of unfavorable polyhedra (“all others”) in the simulated MG in Fig. 43. Such unsatisfied atoms either have a squeezed local environment characterized by positive atomic pressure, or a dilated local environment characterized by negative atomic pressure. Together with the atomic-level shear stresses, these stress components all contribute to the atomic strain energy that quantifies the degree of dissatisfaction of the atom. Since both positive and negative stress/pressure elevate the strain energy, there are two types of structural defects with opposite signs [441]. The existence of these defects and their response under external loading has been studied using computer simulations [52,441,451]. Compared to the original free volume concept, the positive and negative stress defects seem to be more appropriate for MGs, as supported by several experimental observations. First, the density of most metallic liquids only decreases slightly (less than 6% [153]) from the solid upon melting (the solid states often have dense-packed structures such as fcc and hcp), thus the “excess” volume in the liquid is actually very small. Second, the enthalpy release during annealing and structural relaxation is much larger than expected from the total volume shrinkage (free volume annihilation) of the sample [423,452] (many researchers have inaccurately attributed the calorimetry signals entirely to the free volume changes). Third, upon relaxation the MGs have a sharpened first peak in the PDF, with the amount of both shorter and longer bonds reduced [314–316]. All these suggest that there are positive and negative structural defects (i.e., the free volume and “anti-free volume” [444]) which may be annihilated or created in pairs, without significantly changing the total volume (or with the net total volume change being only a second order effect). This feature is especially pronounced in metals because metallic elements and metallic bonds are more flexible and squeezable [153].

The atomic stress/pressure is closely related to the local structure details such as the bond length, CN, and symmetry. However, it is not limited to a particular type of structural motif, but reflects the topological stability in general. In this sense, it is a system-independent representative of the structural order. Using the concept of atomic-level stresses, Egami et al. have proposed a general theory for glass formation and glass behavior, based on the topological fluctuation and stability. For example,

their recent model has successfully predicted  $T_g$  of various MGs, by considering the critical fluctuation of atomic stress/strain in the glass transition range [449]. The critical strain fluctuation fitted with experiment leads to approximately one quarter of liquid-like topologically unstable sites (defined as atoms with >11% volume strain, which may trigger CN changes), close to the percolation limit in the DRP model [449]. That is, the glass transition can be perceived as a critical percolation of the liquid-like regions. The atomic-level stresses are also closely related to the elastic and plastic deformation of MGs in terms of the bond exchange and bond orientational anisotropy, as demonstrated in prior simulations [45,52,453] and experiments [454–456]. Quantitative models describing the deformation behaviors, however, are still to be developed [153,448].

#### 4.3.3. Configurational potential energy

The changing configurational potential energy is the thermodynamic origin of the evolving liquid state. For MGs, the configurational potential energy is the energy level at which the corresponding configuration is frozen. Therefore, the lower the configurational potential energy, the more extensive structural relaxation the metallic liquid has experienced before freezing, and the higher degree of structural ordering is developed in the MG.

Cooperative shear models based on the configurational potential energy have been developed to study the rheology of metallic liquids and deformation of MGs, by Johnson and co-workers [59,80,81]. The modeling work has been successful in describing the Newtonian behavior, non-Newtonian behavior, and strain localization [80,81], as well as the shear modulus and yield strength of the metallic liquids and MGs [59]. The isoconfigurational shear modulus  $G$  is the key parameter for the cooperative shear model. In the PES description, the shear modulus scales with the energy barrier ( $W$ ) of the local megabasin, and thus has a one-to-one correspondence with the viscosity. The  $G$  also scales linearly with configurational potential energy, and the latter can be tuned by either thermal or mechanical approaches [81,416–418]. The model and the supporting evidence thus establish an unambiguous and quantitative link between the liquid/glass state (e.g., viscosity) and the configurational potential energy. Since the configurational potential energy directly reflects the degree of structural ordering (chemical and topological), it can be considered a thermodynamic indicator of the structural state of metallic liquid/glass.

#### 4.3.4. Effective disorder temperature

In the quasi-equilibrium supercooled liquid, the degree of structural order of the liquid inherent structure is characterized by the temperature. The lower the temperature is (i.e., the deeper the supercooling), the higher the degree of ordering. As the supercooled liquid is frozen, it becomes non-equilibrium, and the actual temperature no longer reflects the degree of structural order. Therefore, the effective disorder temperature was proposed as a fictive temperature to represent the non-equilibrium structural state [457,458]. Note that the effective disorder temperature is not a true temperature, as it essentially evaluates the configurational potential energy and degree of structural order of the MG, rather than the kinetic energy. Indeed, it has been demonstrated (by Shi et al. [79]) that there is a linear correlation between such a “fictive temperature” concept and the configurational potential energy. The fictive temperature can also be compared with the fluctuation level of atomic stress/strain in the approach by Egami et al. [449]. Langer and co-workers (e.g., [76,78,459–461]) have employed the effective disorder temperature to establish constitutive model for STZ and deformation of MGs.

#### 4.3.5. Interrelations and differences

The correlations and differences among the various structural indicators will be briefly summarized here. Although emphasizing different perspectives, these effective structural parameters should give a consistent description of the material state, and they should therefore scale with one another, at least statistically. For example, local regions with high atomic-level stresses (i.e., high atomic strain energy) should also have higher configurational potential energy, higher effective disorder temperature, and they should contain more free volume or anti-free volume [153]. In addition, the above mentioned indicators are actually related to the extrinsic disclination density we defined in Section 3, and this density is a parameter based on true structural features (see the various SROs discussed throughout this review). In a Cu<sub>64</sub>Zr<sub>36</sub> MG, for example, we have found that high atomic-level stresses usually

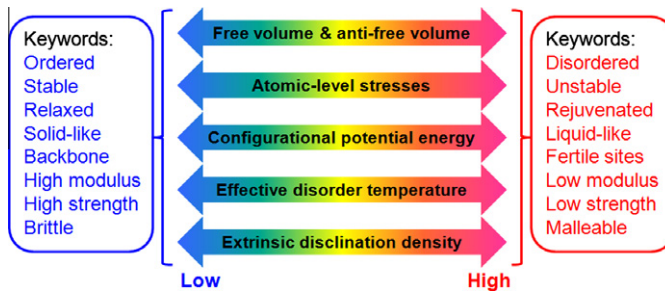


**Fig. 57.** The structural indicators of MGs mentioned in this review and their general relationship. The various keywords used to qualitatively describe the structural states correspond to the high and low ends in the spectrum of each of these indicators.

**Table 11**  
Comparison of various structural indicators for MGs.

Structural indicator	Parameter characterization	Constitutive model for deformation	Scaling relation with viscosity	Structural information conveyed
Free volume <sup>a</sup>	Relative value measurable	Available (e.g., [77])	Exponential	Density
Atomic-level stresses	Currently simulation only	Not yet available	Unknown	Bond length, CN, symmetry
Configurational potential energy	Relative value measurable	Available (e.g., [81])	Exponential	None
Effective disorder temperature	Not directly measurable	Available (e.g., [78])	Exponential	None
Extrinsic disclination density	Currently simulation only	Not yet available	Unknown	Local symmetry

<sup>a</sup> Note that the original definition of free volume needs modifications (e.g., to include anti-free volume) or generalization in order to be applicable for MGs.

correspond to clusters with high density of extrinsic disclinations and/or CNs far from (much lower or higher than) the average value [462]. In Fig. 57, we illustrate the correlations between these parameters, as well as the structural state they correspond to.

Despite the correlations, these structural indicators also have differences in various aspects, which are compared in Table 11. The comparison shows that the atomic-level stresses may be an excellent bridge connecting the structure and properties, for it conveys more structural information yet is still general and system-independent. Moreover, it can be used to calculate atomic strain energy, which is a thermodynamic parameter that may be readily incorporated into a constitutive model. Egami and co-workers have been developing a microscopic theory of MGs based on the atomic-level stresses [153], but more advances are desired, among which a deformation theory (similar to the ones based on free volume, configurational potential energy, or effective disorder temperature) may be a priority.

## 5. Structural perspective of the property–property correlations

The various properties of MGs often exhibit striking correlations, more so than the case of crystalline metals [11]. These apparent property–property relations are a reflection of the common structure origin of the properties. Using the various structure–property correlations discussed above as bridges, these correlations can be rationalized, and the underlying physics understood, as explained in the following.

### 5.1. Thermodynamics/kinetics-GFA correlation

Connecting GFA with thermodynamic and kinetic parameters, such as the  $T_g$ ,  $T_l$ ,  $T_m$ ,  $T_x$ , and fragility ( $m$ ), has been an intriguing subject. A number of indicators have been proposed to evaluate or predict

the GFA of an alloy, most of which involve two or more of the above parameters. Among them, the traditional one is the reduced glass transition temperature,  $T_{rg} = T_g/T_l$  [26], which has been widely used and found to be successful [463]. A more recently proposed one along this line is the index  $\gamma = T_x/(T_g + T_l)$  [464–466]. As discussed in Section 1, there are two directly relevant parameters that influence the GFA, i.e., the  $\Delta G$  (free energy difference between the glass and the crystal the glass transforms into) and the viscosity, including their evolution with supercooling. These two aspects influence the TTT diagram of the alloy, which gives the critical cooling rate for glass formation. Therefore, an effective indicator of GFA must contain as much information as possible on both aspects. An effort in this direction was made recently by Senkov [467], who derived a new indicator based on the analysis of the TTT diagram. The position of the nose-tip, where crystallization is the fastest, was considered the key factor that limits the critical cooling rate, and it can be written as a function of  $m$  and  $T_{rg}$ , each emphasizing one aspect. The proposed indicator,  $F_1$ , has the formula

$$F_1 = 2 \left[ \frac{m}{m_{\min}} \left( \frac{1}{T_{rg}} - 1 \right) + 2 \right]^{-1} \sim -\log_{10}(R_c) \quad (21)$$

where  $m_{\min} \approx 17$  is the minimum fragility corresponding to the strongest glasses (a straight line connecting the viscosity at high temperature limit,  $\sim 10^{-5}$  Pa s, and the critical viscosity for glass transition,  $10^{12}$  Pa s, in Angell's plot, Fig. 2), and  $R_c$  is the critical cooling rate for glass formation. This indicator thus quantifies the known trend that a lower fragility  $m$  together with a higher  $T_{rg}$  favors GFA.

Then what is the role of the structure in this process? As we have discussed, the structural ordering during supercooling is the underlying mechanism of the changing liquid state, i.e., the gradual rise of excess specific heat, decrease of the configurational potential energy and entropy, as well as the non-Arrhenius increase of viscosity. Therefore, how stable and ordered the starting equilibrium liquid is, and how and how fast the structural order increases when the liquid is supercooled, are closely related to  $T_l$ ,  $T_g$ , and the fragility. Specifically, if the equilibrium liquid at  $T_l$  already has strong ordering, and the inherent structure (the configurational state) does not evolve drastically with supercooling, the supercooled liquid would exhibit strong behavior. Typical examples are the covalent glasses such as silica. In contrast, if the liquid has poor inherent structural ordering at  $T_l$ , but the order evolves dramatically with supercooling, fragile behavior would be observed, which may be the case for most MGs including Cu-Zr (Fig. 44). For MGs with similar  $T_{rg}$ , the stronger liquid gains better GFA by establishing structural order to stabilize the supercooled liquid at higher reduced temperature  $T/T_g$  (or  $T/T_l$ ). Cu-Zr-Al versus Cu-Zr is such an example [366], as discussed earlier in Fig. 47. For liquids with similar fragility, a higher  $T_{rg}$  indicates a narrower supercooled temperature region, which would reduce the chance for crystallization because the supercooled liquid is frozen earlier under the same cooling rate. This is demonstrated by Cu-Zr MGs at different compositions [269]. The above description regarding the correlation between structural ordering and GFA of supercooled liquid is in line with the scenario presented by Tanaka [468], and also consistent with Senkov's GFA indicator  $F_1$ . Note that the GFA is correlated with both  $m$  and  $T_{rg}$ , and knowing either parameter alone would not be sufficient to make predictions on the GFA. For instance, it is not appropriate to assume that stronger liquids (or higher  $T_{rg}$ ) would always mean better GFA. Additional discussions on the structure-GFA correlation can be found in Section 4.1., where the thermodynamic and kinetic properties of the supercooled liquids are linked to the atomic-level structure and its evolution with temperature.

## 5.2. $T_g$ -strength correlation

As shown in Fig. 6, the correlation between  $T_g$  and strength in MGs is quite strong and universal. The qualitative correlation between the two has been known for a long time, and a quantitative scaling relation is given in the cooperative shear model by Johnson and Samwer [59], who derived a universal  $(T/T_g)^{2/3}$  dependence of the yield strain. A similar functional form of the correlation has been shown by Cheng et al. [269] and applied to explain the measured strength of a group of Cu-Zr BMGs. The structural origin underlying the  $T_g$ -strength correlation in Cu-Zr was also discussed [269], in terms of the percolation of rigid icosahedra during glass formation, and the breakdown of icosahedra backbone

upon yielding. Specifically, the same rigid clusters (icosahedra in Cu–Zr) play a critical role in both glass transition and yielding [269,270], because the characteristic energy barrier to activate the cluster for structural relaxation is common for both thermal and mechanical processes. Therefore, the more populous the rigid clusters and the better they are connected in the MG, the higher temperature (thermal energy) is required for melting (percolation of “liquidized” regions), and the higher the stress (mechanical energy) is needed for yielding (percolation of activated STZs). A comparison between the thermal process and the mechanical process, as well as the correspondence between the physical parameters, is illustrated in Fig. 58. Note that the equivalence of the two is rooted in the same energy barrier that needs to be surmounted for flow in either melting or yielding, as demonstrated by a recent MD simulation conducted by Guan et al. [62]. Moreover, it is further revealed that the energy barrier for  $\beta$ -relaxation (subbasin height, the unit event leading to  $\alpha$ -relaxation) is very close to the energy barrier for shear transformation in an isolated/individual STZ (the unit event of shear banding and yielding) [469].

The intuitive idea of the equivalence of thermal and mechanical activation in causing flow in MGs has in fact been used repeatedly to account for the  $T_g$ –strength correlation, as done by Yang et al. [60] and Liu et al. [61]. A linear scaling of  $\sigma_y \sim (T_g - T)/V_m$  was derived and fitted with experimental data, where  $\sigma_y$  is the yield strength,  $V_m$  is the molar volume, and  $T$  is the ambient temperature. As such, while the  $T_g$ –strength trend is universal, the exact form of the correlation, i.e., whether it follows a simple linear [60,61] or a more complex relationship [59,269], would depend on many details, such as the microscopic criteria for glass transition and yielding, the exact scaling relationship between the critical temperature/stress and the effective energy barrier, and the profile and statistical features of the megabasin. Different assumptions in modeling would therefore lead to different formulations, although the overall trend predicted is similar and consistent with experimental data.

### 5.3. Poisson's ratio-plasticity correlation

The correlation between elastic and plastic properties in MGs was first proposed by Chen et al. [470], and was later systematically studied and summarized by Lewandowski et al. [64,471], Gu et al. [472], Wang [473], and Liu et al. [474]. The Poisson's ratio  $v$ , or equivalently the shear modulus to bulk modulus ratio  $G/B$  (the two are connected via  $v = (3 - 2\frac{G}{B})/(6 + 2\frac{G}{B})$ ), has been found to be an effective indicator of the intrinsic plasticity and the fracture toughness/energy of MGs. From the energetic perspective, the energy associated shear scales with  $G$ , while that associated with the propagation of crack scales with  $B$  [64,475]. The competition of the two determines the intrinsic plasticity, and is evaluated by the  $G/B$  ratio or  $v$ . In fact, glasses can be considered frozen liquids, and the “fluidity” is indicated by  $v$  – the ability of the material to conserve volume during uniaxial elastic deformation. Naturally, if the MG has higher  $v$ , it can be considered more “liquid-like”, and thus should be easier to flow.

From the glass structure perspective, since there are intrinsic fluctuations in the ordering and stability of local structures, the distribution of the favored clusters (ordered, high packing efficiency, rigid, stable, and solid-like) and unfavorable clusters (disordered, low packing efficiency, floppy,

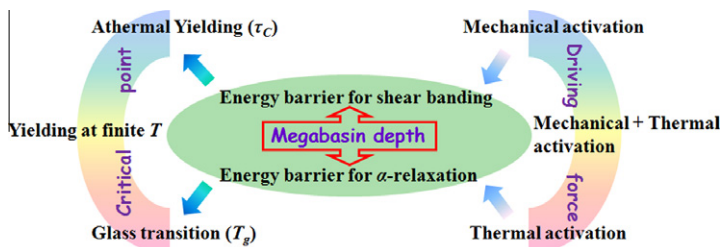


**Fig. 58.** Correlation between glass transition and yielding: equivalence between thermal and mechanical activations in overcoming the energy barrier for flow.

unstable, and liquid-like), as well as their property contrast, should influence the tendency of strain localization and intrinsic plasticity [361]. In a particular MG, the solid-like regions and liquid-like regions have similar  $B$  (as  $B$  is primarily determined by the average electron charge density of the constituent elements), but very different  $G$  (which is not simply an average value of the elements, but rather sensitive to the configuration and structural order [396,416,418]). When comparing different MGs, the normalized and dimensionless value,  $G/B$  (or  $\nu$ ), is thus indicative of not only the average elemental properties, but more importantly, the degree of structural ordering (e.g., the relative fractions and property contrast of the solid-like and liquid-like regions).

In quantitative evaluations, a crude estimate can be given by an interpolation, using the weighted average  $G/B$  of the constituent elements calculated from the tabulated moduli of the constituent elements, as did by Wang [473] and by Zhang and Greer [33]. The real MG can have a  $G/B$  ratio that deviates significantly from this interpolation, because the same elements can produce very different glass

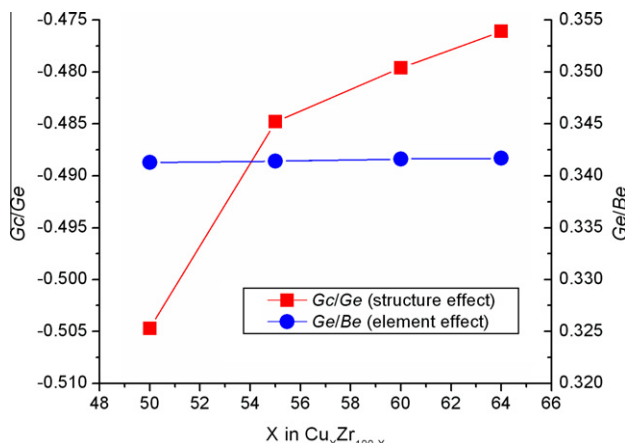


**Fig. 59.** Composition dependence of structural contribution and elemental contribution to the  $G/B$  ratio in MD-simulated Cu-Zr MGs [361]. The elemental effect is almost constant, and the structural effect dominates. Cu-rich MGs are more solid-like in structure, with higher  $G/B$  ratio and lower Poisson's ratio.

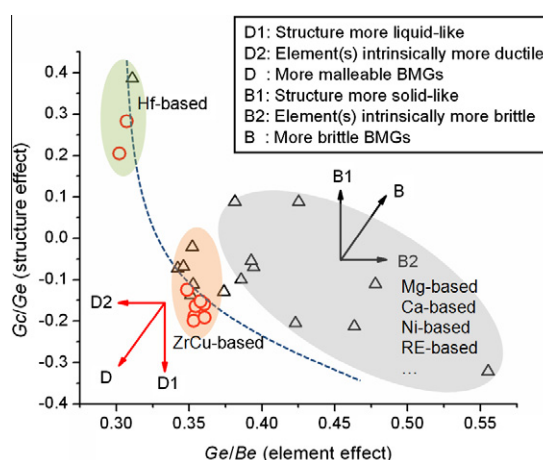


**Fig. 60.** A map for locating malleable BMGs. Red circles (black triangles) represent malleable (brittle) BMGs. The lower-left side is the direction to go for BMGs with better plasticity. The dashed line is a tentative boundary separating brittle and malleable BMGs included in this map. Shaded areas (gray, orange, and green) label different MG groups [361].

structures (including at a given composition). The  $G/B$  (or  $v$ ) property of an MG (and hence its intrinsic plasticity) is thus an overall result of the elemental properties and the glass structure. The deviation from the rule of mixtures can in fact be used as an indicator of the internal structure or the glass configuration, including both topological and chemical order. This approach has been illustrated using Cu-Zr examples, and extended to a comparison of many different BMGs [361]. Specifically, the  $G/B$  ratio can be decomposed into contributions from average properties of the constituent elements ( $G_e/B_e$ , elemental effect) and the configuration of these elements in the MG ( $G_c/G_e$ , structural effect), in the form of  $\frac{G}{B} \approx \frac{G_e}{B_e} \left(1 + \frac{G_c}{G_e}\right)$ , see Ref. [361] for details. For Cu-Zr at different compositions, the former ( $G_e/B_e$ ) is almost unchanged and the differences lie in the latter (Fig. 59): Cu-richer MGs are more solid-like in terms of structure, as demonstrated by their higher  $G_c/G_e$  (structural effect) and thus the higher over-all  $G/B$ . Such a trend is not monotonic but reversed at very Cu-rich composition (above 70 at.% Cu in simulation), where  $T_g$  [269],  $G_c/G_e$  and  $G/B$  all decrease to indicate a more liquid-like structure. When involving more different BMGs in the comparison, the elemental effect ( $G_e/B_e$ ) may also be pronounced, and we can locate potentially malleable BMGs in a 2D map with  $G_e/B_e$  and  $G_c/G_e$  as coordinate axes (Fig. 60).

## 6. Summary and outlook

As materials with both scientific interest and potential applications, the MGs (and BMGs) are at the cutting edge of metals research. Understanding the internal structure of these glasses in relation with their properties is of fundamental importance. Progress made in this area over the past 50 years has resolved a number of key issues and provided leads to many interesting aspects of the science of glasses, as discussed in the current review. To conclude, here we briefly summarize some general principles that can be extracted from the findings so far.

1. The atomic-level mechanism underlying the structural organization of various metallic liquids and glasses appears to be the polytetrahedral packing that results in dense and efficient arrangements of the atoms. Polytetrahedral packing is severely frustrated in monatomic systems, but the packing frustration can be relieved by using atoms with different sizes. Therefore, topologically the MG structure requires appropriate alloy compositions to achieve polytetrahedral packing with minimum frustration. Meanwhile, such a configuration must also be chemically favorable and stable, requiring the neighboring atoms to have relatively strong chemical affinity, or negative heat of mixing between the main participating species. These two general principles control MG structures with different packing motifs.
2. Different categories of MGs have different characteristic local motifs, due to the different atomic size ratio and chemical make-up. The basic motifs are best characterized in terms of quasi-equivalent clusters with certain topological, chemical, or functional features (e.g., P-centered clusters in Ni<sub>80</sub>P<sub>20</sub>, or Cu-centered clusters in Cu<sub>64</sub>Zr<sub>36</sub>). The MG structure can then be viewed as efficient packing of these clusters in a dense and random manner, via various sharing schemes. While icosahedral order, and in particular the importance of full icosahedra, has been emphasized in many recent structural studies in some key MG-forming alloys (such as BMGs based on Cu-Zr), the degree of this order is actually composition dependent, and obviously system dependent, depending on the atomic size ratio and chemistry. Z clusters of non-icosahedral types (such as TTP) dominate in many important MGs, including Al-rich glasses and LTM-NM systems. The range of local structural motifs of various typical MGs has been surveyed and described in this review.
3. The structure inside an MG has intrinsic variations and fluctuations. Unlike in a crystal, the local structure in MG is not identical everywhere, but changes from site to site. As a result, there will be relatively better ordered (more stable) regions and relatively more disordered (unstable) regions. The ordered region is characterized by more regular and efficient polytetrahedral packing (i.e., the Z clusters), with minimum distortion and extrinsic disclinations. Structural relaxation (e.g., slower cooling rate, annealing, or aging) leads to larger fraction and better connection of the Z clusters, accompanied by the relief of distortion and annihilation of structural defects (e.g., extrinsic disclinations), while structural rejuvenation (e.g., elastostatic deformation) reverses the relaxation process by disordering Z clusters and creating more unstable clusters.

4. The above structural heterogeneity is the origin of dynamical heterogeneity in supercooled liquids, and mechanical heterogeneity in MGs. The better ordered (or solid-like) regions usually correspond to slower relaxation dynamics, higher local stiffness, and higher activation barrier for structural rearrangement. In contrast, more disordered (liquid-like) regions relax faster, as they have lower local stiffness and stability. Such a microscopic correlation between structure, dynamics and mechanical properties, as well as their coupled evolution during glass formation, can be used to understand many macroscopic observations, e.g., the GFA, fragility, modulus, yield strength, plasticity, and the associated composition and/or processing history dependence. As a particular example, the property contrast between the solid-like and liquid-like regions affect the propensity for strain localization, and their distribution is thus related to the intrinsic plasticity of the MG, and reflected by the Poisson's ratio.
5. Icosahedral ordering with fivefold bonds has been found to be ubiquitous in monatomic as well as multicomponent systems, and in both liquids and MGs. The  $\langle 0, 0, 12, 0 \rangle$  full icosahedra, in particular, form in large numbers to dominate the structure for some MGs/liquids over certain composition ranges, and are potent stabilizers of the amorphous structure. The low potential energy and atomic-level stresses of these coordination polyhedra render them particularly resistant to changes, hence slowing down the dynamics, increasing the heat capacity, raising the resistance to local environment transitions and shear transformations, and elevating the barrier for crystallization. As such, full icosahedra are featured prominently in our discussion of glass structures and their role as "solid-like" structures in controlling properties. For other non-icosahedral MGs and liquids, there are other types of Z clusters that play similar role, but to a less extent. The other important group of local structures sits on the other end of the spectrum: for all glasses there will be a range of local structures (coordination polyhedra) that are "unhappy" or "liquid-like". They are prone to changes and their high propensity for relaxation and plastic flow has been illustrated in the preceding sections.

While the discoveries so far are enlightening, many unresolved problems persist in the field of the structure and structure–property relationship in MGs. Some of the remaining puzzles are of very fundamental nature and there is a pressing need for their resolution. For example:

1. Atomic-level structures of complex BMGs, particularly those containing more than three elements, have not been well understood. These are the BMGs with the best GFA and mechanical properties. Very often, minor additions (e.g., less than one atomic percent) of alloying elements, or even a substitution of similar elements (such as Ni for Cu), result in pronounced changes in GFA and deformation response. A structural understanding of these phenomena has not been forthcoming. The difficulty in unraveling the structure of multicomponent MGs is primarily due to the lack of powerful tools that can break the degeneracy to reveal the complicated and entangled topological and chemical order in such systems. The presence of subcritical nuclei and nanoscale phase separation in realistic BMG samples, which also considerably influences the properties, poses additional challenges on the structural characterization.
2. Although the SRO has been successfully studied in many different MGs, the MRO in most MGs remains vague, hampering our understanding of MG behavior on a number of fronts. It is a non-trivial task to characterize the MRO. First of all, one needs proper structural parameters to describe the ordering over longer length-scale. In solute-lean MGs where the structural unit is the quasi-equivalent solute-centered clusters, one may simply apply the SRO parameters on the solute "sub-lattice" to characterize the MRO in terms of cluster packing. There the medium-range correlation of the solute atoms is very pronounced and well characterized [152,221]. For concentrated MGs, however, a different approach is needed. Second, due to the weaker and indirect correlations for atoms at longer distance, MRO may not be as pronounced as SRO, which is demonstrated by the much wider second peak and diminishing high-order peaks in the PDF. Therefore, different MRO types may not exhibit very sharp features that are characteristic and distinctive. A continuous and smeared spectrum is always expected, such that it has been difficult to tell apart the proposed schemes (icosahedral-like, fcc-like, or fractal like). Third, in laboratory-made BMGs, it has been shown that medium-range structures in the form of nano-crystallites are possible. The crystallites

may be the nuclei of the competing crystalline phase (such as the primary crystallization product), which can be different from the MRO defined for fully amorphous, monolithic MGs. Fourth, computer simulations, while (barely) sufficient to capture the SRO, may fall short in catching the features over medium range due to the spatial and temporal limitations on today's computers.

3. It is important to underscore the significance of MRO in understanding the MG properties. The MRO could be the main difference between the glass and crystal in some alloys and systems, where the relatively strong chemical affinity and bond directionality renders the SRO in the glass almost identical to that in the crystal. Also, the MRO typically covers a few hundreds of atoms, which is comparable to the STZ size (or the length-scale of  $\beta$ -relaxation). Therefore, how the short-range clusters organized into MRO may have considerable impact on the local shear transformation behavior and the subsequent localization and shear banding. Moreover, with the same SRO, there can be different types and degrees of MRO, which could be as important as SRO in affecting how the MG responds to external stimuli. The MRO may further extend to become backbone-like 3-D percolation. Then how to characterize such a backbone, how to define the critical percolation, and how the behavior of this backbone is related to the transition points (e.g., glass transition and yielding) are questions that need to be addressed.
4. At present, what has been and is being uncovered is the general trend of the structure–property correlations, as well as the intrinsic links and underlying mechanisms. It remains a major task to make use of the structural information in designing MG compositions and properties, and attempts in this direction have begun only recently [283,435]. Presumably, one can use the insights gained for more general constitutive modeling. For example, the distribution of solid-like and liquid-like regions and their property contrast are expected to be suitable internal variables for methods such as finite element analysis. In addition, the spatial distribution, degree of connectivity, and rigidity of these regions are also tunable parameters. One can then study how the above structural features affect the properties, such as the evolution from scattered STZs to shear band, and the kinetic process of the plastic instability leading to catastrophe. This will provide valuable insight into what structural features are desired for a particular property. The goal of composition tuning and material processing is then to achieve these structural features in experiments.
5. The structure–property correlations discussed in this review remain mostly qualitative and at best semi-quantitative. The observations, even though often backed by some quantitative analysis of microscopic processes, have not yet led to a quantitative theory to make verifiable predictions of material behavior. In this sense, the research to establish structure–property relationships for MGs is still in an early stage, especially when compared with their crystalline counterparts. Ample opportunities remain, with many open questions awaiting future research.

## Acknowledgements

The authors are indebted to Dr. H.W. Sheng for the numerous contributions he has made to this subject, and in particular to the development of EAM potentials. We thank Drs. W.K. Luo and A.J. Cao for their input. We are also grateful to Drs. A.L. Greer, D.B. Miracle, Y. Li, D. Ma, A.D. Stoica, and X.L. Wang for their valuable comments on the manuscript, and Drs. M.L. Falk, T. Egami, J.C. Lee, J. Xu, T.C. Hufnagel, F. Spaepen, K.F. Kelton, A.R. Yavari, M.W. Chen, and C. Dong for stimulating discussions. Experiments in this work were conducted at Brookhaven National Laboratory and the Advance Photon Source at Argonne National laboratory, assisted by Drs. F.M. Alamgir, J.M. Bai, H.Z. Liu, P.D. Lee, S.D. Shastri, Y. Meng, and J. Wen. This work was supported at JHU by US Department of Energy – Basic Energy Sciences, Division of Materials Science and Engineering, under Contract No. DE-FG02-09ER46056, and by the US National Science Foundation, Grant No. DMR-0904188.

## References

- [1] Klement W, Willens RH, Duwez P. Non-crystalline structure in solidified gold-silicon alloys. *Nature* 1960;187(4740):869–70.
- [2] Chaudhari P, Turnbull D. Structure and properties of metallic glasses. *Science* 1978;199(4324):11–21.

- [3] Chen HS. Glassy metals. *Rep Prog Phys* 1980;43(4):353.
- [4] Greer AL. Metallic glasses. *Science* 1995;267(5206):1947–53.
- [5] Johnson WL. Bulk glass-forming metallic alloys: science and technology. *MRS Bull* 1999;24(10):42–56.
- [6] Inoue A. Stabilization of metallic supercooled liquid and bulk amorphous alloys. *Acta Mater* 2000;48(1):279–306.
- [7] Inoue A, Takeuchi A. Recent progress in bulk glassy alloys. *Mater Trans* 2002;43(8):1892–906.
- [8] Johnson WL. Bulk amorphous metal – an emerging engineering material. *JOM – J Miner Met Mater Soc* 2002;54(3):40–3.
- [9] Loffler JF. Bulk metallic glasses. *Intermetallics* 2003;11(6):529–40.
- [10] Wang WH, Dong C, Shek CH. Bulk metallic glasses. *Mater Sci Eng R – Rep* 2004;44(2–3):45–89.
- [11] Greer AL, Ma E. Bulk metallic glasses: at the cutting edge of metals research. *MRS Bull* 2007;32(8):611–5.
- [12] Greer AL. Metallic glasses on the threshold. *Mater Today* 2009;12(1–2):14–22.
- [13] Li Y et al. Formation of bulk metallic glasses and their composites. *MRS Bull* 2007;32(8):624–8.
- [14] Takeuchi A, Inoue A. Classification of bulk metallic glasses by atomic size difference, heat of mixing and period of constituent elements and its application to characterization of the main alloying element. *Mater Trans* 2005;46(12):2817–29.
- [15] Inoue A. High-strength bulk amorphous-alloys with low critical cooling rates. *Mater Trans* 1995;36(7):866–75.
- [16] Gotze W, Sjogren L. Relaxation processes in supercooled liquids. *Rep Prog Phys* 1992;55(3):241–376.
- [17] Angell CA. Formation of glasses from liquids and biopolymers. *Science* 1995;267(5206):1924–35.
- [18] Ediger MD, Angell CA, Nagel SR. Supercooled liquids and glasses. *J Phys Chem* 1996;100(31):13200–12.
- [19] Debenedetti PG, Stillinger FH. Supercooled liquids and the glass transition. *Nature* 2001;410(6825):259–67.
- [20] Johnson WL. Fundamental aspects of bulk metallic glass formation in multicomponent alloys. In: Schulz R, editor. *Metastable, mechanically alloyed and nanocrystalline materials. Pts 1 and 2*; 1996. p. 35–49.
- [21] Busch R. The thermophysical properties of bulk metallic glass-forming liquids. *JOM – J Miner Met Mater Soc* 2000;52(7):39–42.
- [22] Busch R, Schroers J, Wang WH. Thermodynamics and kinetics of bulk metallic glass. *MRS Bull* 2007;32(8):620–3.
- [23] Angell CA. Spectroscopy simulation and scattering, and the medium range order problem in glass. *J Non-Cryst Solids* 1985;73(1–3):1–17.
- [24] Adam G, Gibbs JH. On temperature dependence of cooperative relaxation properties in glass-forming liquids. *J Chem Phys* 1965;43(1):139.
- [25] Busch R, Kim YJ, Johnson WL. Thermodynamics and kinetics of the undercooled liquid and the glass-transition of the  $Zr_{41.2}Ti_{13.8}Cu_{12.5}Ni^{10.0}Be_{22.5}$  alloy. *J Appl Phys* 1995;77(8):4039–43.
- [26] Turnbull D. Under what conditions can a glass be formed. *Contemp Phys* 1969;10(5):473.
- [27] Gilman JJ. Mechanical-behavior of metallic glasses. *J Appl Phys* 1975;46(4):1625–33.
- [28] Ashby MF, Greer AL. Metallic glasses as structural materials. *Scripta Mater* 2006;54(3):321–6.
- [29] Schuh CA, Hufnagel TC, Ramamurty U. Overview no. 144 – mechanical behavior of amorphous alloys. *Acta Mater* 2007;55(12):4067–109.
- [30] Yavari AR, Lewandowski JJ, Eckert J. Mechanical properties of bulk metallic glasses. *MRS Bull* 2007;32(8):635–8.
- [31] Chen MW. Mechanical behavior of metallic glasses: microscopic understanding of strength and ductility. *Ann Rev Mater Res* 2008;38:445–69.
- [32] Wang WH. Elastic moduli and behaviors of metallic glasses. *J Non-Cryst Solids* 2005;351(16–17):1481–5.
- [33] Zhang Y, Greer AL. Correlations for predicting plasticity or brittleness of metallic glasses. *J Alloy Compd* 2007;434:2–5.
- [34] Wang JQ et al. Correlations between elastic moduli and molar volume in metallic glasses. *Appl Phys Lett* 2009;94(12):121904.
- [35] Granato AV. The specific heat of simple liquids. *J Non-Cryst Solids* 2002;307:376–86.
- [36] Safarik DJ, Schwarz RB. Elastic constants of amorphous and single-crystal  $Pd_{40}Cu_{40}P_{20}$ . *Acta Mater* 2007;55(17):5736–46.
- [37] Khonik SV et al. Evidence of distributed interstitial-like relaxation of the shear modulus due to structural relaxation of metallic glasses. *Phys Rev Lett* 2008;100(6):065501.
- [38] Gilman JJ. Electronic basis of the strength of materials. Cambridge: Cambridge University Press; 2003.
- [39] Weaire D et al. Use of pair potentials to calculate properties of amorphous metals. *Acta Metall* 1971;19(8):779.
- [40] Argon AS. Mechanisms of inelastic deformation in metallic glasses. *J Phys Chem Solids* 1982;43(10):945–61.
- [41] Mizubayashi H et al. Dynamical anelastic response of amorphous alloys suggesting collective motions of many atoms. *Acta Mater* 1998;46(4):1257–64.
- [42] Poulsen HF et al. Measuring strain distributions in amorphous materials. *Nat Mater* 2005;4(1):33–6.
- [43] Hufnagel TC, Ott RT, Almer J. Structural aspects of elastic deformation of a metallic glass. *Phys Rev B* 2006;73(6):064204.
- [44] Dmowski W et al. Elastic heterogeneity in metallic glasses. *Phys Rev Lett* 2010;105(20):205502.
- [45] Suzuki Y, Egami T. Shear deformation of glassy metals – breakdown of cauchy relationship and anelasticity. *J Non-Cryst Solids* 1985;75(1–3):361–6.
- [46] Knuyt G, Deschépelle L, Stals LM. Calculation of elastic-constants for an amorphous metal and the influence of relaxation. *J Phys F – Met Phys* 1986;16(12):1989–206.
- [47] Tanguy A et al. Continuum limit of amorphous elastic bodies: a finite-size study of low-frequency harmonic vibrations. *Phys Rev B* 2002;66(17):174205.
- [48] Tanguy A, Leonforte F, Barrat JL. Plastic response of a 2D Lennard-Jones amorphous solid: detailed analysis of the local rearrangements at very slow strain rate. *Eur Phys J E* 2006;20(3):355–64.
- [49] Barrat JL, de Pablo JJ. Modeling deformation and flow of disordered materials. *MRS Bull* 2007;32(11):941–4.
- [50] Tsamados M et al. Local elasticity map and plasticity in a model Lennard-Jones glass. *Phys Rev E* 2009;80(2):026112.
- [51] Mayr SG. Relaxation kinetics and mechanical stability of metallic glasses and supercooled melts. *Phys Rev B* 2009;79(6):060201.
- [52] Srolovitz D, Vitek V, Egami T. An atomistic study of deformation of amorphous metals. *Acta Metall* 1983;31(2):335–52.
- [53] Yoshimoto K et al. Mechanical heterogeneities in model polymer glasses at small length scales. *Phys Rev Lett* 2004;93(17):175501.

- [54] Barmatz M, Chen HS. Youngs modulus and internal-friction in metallic glass alloys from 1.5 to 300 K. *Phys Rev B* 1974;9(10):4073–83.
- [55] Bothe K, Neuhauser H. Relaxation of metallic-glass structure measured by elastic-modulus and internal-friction. *J Non-Cryst Solids* 1983;56(1–3):279–84.
- [56] Morito N, Egami T. Internal-friction and reversible structural relaxation in the metallic-glass  $\text{Fe}_{32}\text{Ni}_{36}\text{Cr}_{14}\text{P}_{12}\text{B}_6$ . *Acta Metall* 1984;32(4):603–13.
- [57] Morito N, Egami T. Correlation of the shear modulus and internal-friction in the reversible structural relaxation of a glassy metal. *J Non-Cryst Solids* 1984;61–62(January):973–8.
- [58] Golding B, Hsu FSL, Bagley BG. Soft transverse phonons in a metallic glass. *Phys Rev Lett* 1972;29(1):68.
- [59] Johnson WL, Samwer K. A universal criterion for plastic yielding of metallic glasses with a  $(T/T_g)^{(2/3)}$  temperature dependence. *Phys Rev Lett* 2005;95(19):195501.
- [60] Yang B, Liu CT, Nieh TG. Unified equation for the strength of bulk metallic glasses. *Appl Phys Lett* 2006;88(22):221911.
- [61] Liu YH et al. Thermodynamic origins of shear band formation and the universal scaling law of metallic glass strength. *Phys Rev Lett* 2009;103(6):065504.
- [62] Guan PF, Chen MW, Egami T. Stress-temperature scaling for steady-state flow in metallic glasses. *Phys Rev Lett* 2010;104(20):205701.
- [63] Park KW et al. Atomic packing density and its influence on the properties of Cu-Zr amorphous alloys. *Scripta Mater* 2007;57(9):805–8.
- [64] Lewandowski JJ, Wang WH, Greer AL. Intrinsic plasticity or brittleness of metallic glasses. *Philos Mag Lett* 2005;85(2):77–87.
- [65] Guo H et al. Tensile ductility and necking of metallic glass. *Nat Mater* 2007;6(10):735–9.
- [66] Shan ZW et al. Plastic flow and failure resistance of metallic glass: insight from in situ compression of nanopillars. *Phys Rev B* 2008;77(15):155419.
- [67] Schuster BE et al. Bulk and microscale compressive properties of a Pd-based metallic glass. *Scripta Mater* 2007;57(6):517–20.
- [68] Schuster BE et al. Size-independent strength and deformation mode in compression of a Pd-based metallic glass. *Acta Mater* 2008;56(18):5091–100.
- [69] Jang DC, Greer JR. Transition from a strong-yet-brittle to a stronger-and-ductile state by size reduction of metallic glasses. *Nat Mater* 2010;9(3):215–9.
- [70] Argon AS. Plastic-deformation in metallic glasses. *Acta Metall* 1979;27(1):47–58.
- [71] Pan D et al. Experimental characterization of shear transformation zones for plastic flow of bulk metallic glasses. *Proc Natl Acad Sci USA* 2008;105(39):14769–72.
- [72] Shimizu F, Ogata S, Li J. Yield point of metallic glass. *Acta Mater* 2006;54(16):4293–8.
- [73] Schall P, Weitz DA, Spaepen F. Structural rearrangements that govern flow in colloidal glasses. *Science* 2007;318(5858):1895–9.
- [74] Johnson WL, Lu J, Demetriou MD. Deformation and flow in bulk metallic glasses and deeply undercooled glass forming liquids – a self consistent dynamic free volume model. *Intermetallics* 2002;10(11–12):1039–46.
- [75] Falk ML, Langer JS. Dynamics of viscoplastic deformation in amorphous solids. *Phys Rev E* 1998;57(6):7192–205.
- [76] Langer JS. Shear-transformation-zone theory of deformation in metallic glasses. *Scripta Mater* 2006;54(3):375–9.
- [77] Spaepen F. Microscopic mechanism for steady-state inhomogeneous flow in metallic glasses. *Acta Metall* 1977;25(4):407–15.
- [78] Langer JS. Dynamics of shear-transformation zones in amorphous plasticity: formulation in terms of an effective disorder temperature. *Phys Rev E* 2004;70(4):041502.
- [79] Shi YF et al. Evaluation of the disorder temperature and free-volume formalisms via simulations of shear banding in amorphous solids. *Phys Rev Lett* 2007;98(18):185505.
- [80] Demetriou MD et al. Cooperative shear model for the rheology of glass-forming metallic liquids. *Phys Rev Lett* 2006;97(6):065502.
- [81] Johnson WL et al. Rheology and ultrasonic properties of metallic glass-forming liquids: a potential energy landscape perspective. *MRS Bull* 2007;32(8):644–50.
- [82] Anand L, Su C. A theory for amorphous viscoplastic materials undergoing finite deformations, with application to metallic glasses. *J Mech Phys Solids* 2005;53(6):1362–96.
- [83] Egami T, Billinge SJL. Underneath the Bragg peaks: Structural analysis of complex materials. In: Cahn RW, editor. *Pergamon materials series*, vol. 7. Oxford: Elsevier; 2003.
- [84] Warren BE. X-ray diffraction. New York: Dover Publications Inc.; 1990.
- [85] Cowley JM. X-ray measurement of order in single crystals of  $(\text{Cu}_3\text{Au})$ . *J Appl Phys* 1950;21(1):24–9.
- [86] Cargill GS, Spaepen F. Description of chemical ordering in amorphous-alloys. *J Non-Cryst Solids* 1981;43(1):91–7.
- [87] Steinhardt PJ, Nelson DR, Ronchetti M. Icosahedral bond orientational order in supercooled liquids. *Phys Rev Lett* 1981;47(18):1297–300.
- [88] Steinhardt PJ, Nelson DR, Ronchetti M. Bond-orientational order in liquids and glasses. *Phys Rev B* 1983;28(2):784–805.
- [89] Clarke AS, Jónsson H. Structural changes accompanying densification of random hard-sphere packings. *Phys Rev E* 1993;47(6):3975–84.
- [90] Honeycutt JD, Andersen HC. Molecular-dynamics study of melting and freezing of small Lennard-Jones clusters. *J Phys Chem* 1987;91(19):4950–63.
- [91] Voronoi G. New parametric applications concerning the theory of quadratic forms – second announcement. *J Reine Angew Math* 1908;134(1/4):198–287.
- [92] Richards FM. Interpretation of protein structures – total volume, group volume distributions and packing density. *J Mol Biol* 1974;82(1):1–14.
- [93] Sheng HW et al. Atomic packing in multicomponent aluminum-based metallic glasses. *Acta Mater* 2008;56(20):6264–72.
- [94] Hufnagel TC, Gu XF, Munkholm A. Anomalous small-angle X-ray scattering studies of phase separation in bulk amorphous  $\text{Zr}_{52.5}\text{Ti}_5\text{Cu}_{17.5}\text{Ni}_{14.6}\text{Al}_{10}$ . *Mater Trans* 2001;42(4):562–4.

- [95] Wochner P et al. X-ray cross correlation analysis uncovers hidden local symmetries in disordered matter. *Proc Natl Acad Sci USA* 2009;106(28):11511–4.
- [96] Raines KS et al. Three-dimensional structure determination from a single view. *Nature* 2010;463(7278):214–7.
- [97] Teo BK. EXAFS: basic principles and data analysis. Berlin: Springer-Verlag; 1986.
- [98] Rehr JJ, Albers RC. Theoretical approaches to X-ray absorption fine structure. *Rev Mod Phys* 2000;72(3):621–54.
- [99] Ankudinov AL et al. Real-space multiple-scattering calculation and interpretation of X-ray-absorption near-edge structure. *Phys Rev B* 1998;58(12):7565–76.
- [100] Luo WK et al. Icosahedral short-range order in amorphous alloys. *Phys Rev Lett* 2004;92(14):145502.
- [101] Treacy MMJ et al. Fluctuation microscopy: a probe of medium range order. *Rep Prog Phys* 2005;68(12):2899–944.
- [102] Voyles PM, Gibson JM, Treacy MMJ. Fluctuation microscopy: a probe of atomic correlations in disordered materials. *J Electron Microscop* 2000;49(2):259–66.
- [103] Gibson JM, Treacy MMJ. Diminished medium-range order observed in annealed amorphous germanium. *Phys Rev Lett* 1997;78(6):1074–7.
- [104] Voyles PM et al. Absence of an abrupt phase change from polycrystalline to amorphous in silicon with deposition temperature. *Phys Rev Lett* 2001;86(24):5514–7.
- [105] Wen J et al. Distinguishing medium-range order in metallic glasses using fluctuation electron microscopy: a theoretical study using atomic models. *J Appl Phys* 2009;105(4):043519.
- [106] Hwang J et al. Reverse Monte Carlo structural model for a zirconium-based metallic glass incorporating fluctuation microscopy medium-range order data. *J Mater Res* 2009;24(10):3121–9.
- [107] Stratton WG et al. Aluminum nanoscale order in amorphous Al<sub>92</sub>Sm<sub>8</sub> measured by fluctuation electron microscopy. *Appl Phys Lett* 2005;86(14):141910.
- [108] Li J, Gu X, Hufnagel TC. Using fluctuation microscopy to characterize structural order in metallic glasses. *Microsc Microanal* 2003;9(6):509–15.
- [109] Williams DB, Carter CB. Transmission electron microscopy: a textbook for materials science. Springer; 2004.
- [110] Chang HJ et al. Observation of artifact-free amorphous structure in Cu-Zr-based alloy using transmission electron microscopy. *Mater Sci Eng A – Struct Mater Prop Microstruct Process* 2005;406(1–2):119–24.
- [111] Chen LY et al. Homogeneity of the Zr<sub>64.13</sub>Cu<sub>15.75</sub>Ni<sub>10.12</sub>Al<sub>10</sub> bulk metallic glass. *J Mater Res* 2009;24(10):3116–20.
- [112] Liu YH, Wang WH. Comment on “Homogeneity of Zr<sub>64.13</sub>Cu<sub>15.75</sub>Ni<sub>10.12</sub>Al<sub>10</sub> bulk metallic glass,” by L-Y. Chen, Y-W. Zeng, Q-P. Cao, B-J. Park, Y-M. Chen, K. Hono, U. Vainio, Z-L. Zhang, U. Kaiser, X-D. Wang, and J-Z. Jiang *J. Mater. Res.* 24, 3116 (2009). *J Mater Res* 2010;25(3):598–601.
- [113] Chen LY et al. Ion sputter erosion in metallic glass-A response to “Comment on: Homogeneity of Zr<sub>64.13</sub>Cu<sub>15.75</sub>Ni<sub>10.12</sub>Al<sub>10</sub> bulk metallic glass” by L-Y. Chen, Y-W. Zeng, Q-P. Cao, B-J. Park, Y-M. Chen, K. Hono, U. Vainio, Z-L. Zhang, U. Kaiser, X-D. Wang, and J-Z. Jiang *J. Mater. Res.* 24, 3116 (2009). *J Mater Res* 2010;25(3):602–4.
- [114] Sun BB et al. Artifacts induced in metallic glasses during TEM sample preparation. *Scripta Mater* 2005;53(7):805–9.
- [115] Li J, Wang ZL, Hufnagel TC. Characterization of nanometer-scale defects in metallic glasses by quantitative high-resolution transmission electron microscopy. *Phys Rev B* 2002;65(14):144201.
- [116] Hirata A et al. Local structural fluctuation in Pd–Ni–P bulk metallic glasses examined using nanobeam electron diffraction. *J Alloy Compd* 2009;483(1–2):64–9.
- [117] Chen MW et al. Extraordinary plasticity of ductile bulk metallic glasses. *Phys Rev Lett* 2006;96(24):245502.
- [118] Li GQ et al. Local structure variations in Al<sub>89</sub>La<sub>3</sub>Ni<sub>2</sub> metallic glass. *Acta Mater* 2009;57(3):804–11.
- [119] Hirata A et al. Direct observation of local atomic order in a metallic glass. *Nat Mater* 2011;10(1):28–33.
- [120] Ma E, Zhang Z. Reflections from the glass maze. *Nat Mater* 2011;10(1): 10–1.
- [121] Sligher CP. Principles of magnetic resonance. 3rd ed. New York: Springer-Verlag; 1990.
- [122] Panissod P et al. Local symmetry around the glass-former sites in amorphous metallic alloys through electric quadrupole effects. *Phys Rev Lett* 1980;44(22):1465–8.
- [123] Tang XP et al. Slow atomic motion in Zr–Ti–Cu–Ni–Be metallic glasses studied by NMR. *Phys Rev Lett* 1998;81(24):5358–61.
- [124] Tang XP et al. Devitrification of the Zr<sub>41.2</sub>Ti<sub>13.8</sub>Cu<sub>12.5</sub>Ni<sub>10.0</sub>Be<sub>22.5</sub> bulk metallic glass studied by XRD, SANS, and NMR. *J Non-Cryst Solids* 2003;317(1–2):118–22.
- [125] Breitzke H et al. NMR investigations of medium-range order and quasicrystal formation in Zr<sub>59</sub>Cu<sub>20</sub>Al<sub>10</sub>Ni<sub>3</sub>Ti<sub>3</sub> metallic glass. *Phys Rev B* 2004;70(1):014201.
- [126] Imafuku M et al. Change in environmental structure around Al in Zr<sub>60</sub>Ni<sub>25</sub>Al<sub>15</sub> metallic glass upon crystallization studied by nuclear magnetic resonance. *J Non-Cryst Solids* 2005;351(46–48):3587–92.
- [127] Xi XK et al. Correlation of atomic cluster symmetry and glass-forming ability of metallic glass. *Phys Rev Lett* 2007;99(9):095501.
- [128] Xi XK et al. Structural changes induced by microalloying in Cu<sub>46</sub>Zr<sub>47-x</sub>Al<sub>x</sub>Gd<sub>x</sub> metallic glasses. *Scripta Mater* 2009;61(10):967–9.
- [129] McGreevy RL. Reverse Monte Carlo modelling. *J Phys – Condens Matter* 2001;13(46):R877–913.
- [130] Pusztai L, Toth G. On the uniqueness of the reverse Monte-Carlo simulation. 1. Simple liquids, partial radial-distribution functions. *J Chem Phys* 1991;94(4):3042–9.
- [131] Jedlovszky P et al. Investigation of the uniqueness of the reverse Monte Carlo method: studies on liquid water. *J Chem Phys* 1996;105(1):245–54.
- [132] Mendelev MI, Kramer MJ. Reliability of methods of computer simulation of structure of amorphous alloys. *J Appl Phys* 2010;107(7):073505.
- [133] Luo WK, Ma E. EXAFS measurements and reverse Monte Carlo modeling of atomic structure in amorphous Ni<sub>80</sub>P<sub>20</sub> alloys. *J Non-Cryst Solids* 2008;354(10–11):945–55.
- [134] Mattern N et al. Short-range order of Cu–Zr metallic glasses. *J Alloy Compd* 2009;485(1–2):163–9.
- [135] Li M et al. Structural heterogeneity and medium-range order in Zr<sub>x</sub>Cu<sub>100-x</sub> metallic glasses. *Phys Rev B* 2009;80(18):184201.

- [136] Biswas P, Tafen D, Drabold DA. Experimentally constrained molecular relaxation: the case of glassy GeSe<sub>2</sub>. *Phys Rev B* 2005;71(5):054204.
- [137] Biswas P et al. Materials modeling by design: applications to amorphous solids. *J Phys – Condens Matter* 2009;21(8):084207.
- [138] Allen MP, Tildesley DJ. Computer simulation of liquids. Oxford: Oxford University Press; 1989.
- [139] Leach AR. Molecular modeling: principles and applications. 2nd ed. Prentice Hall; 2001.
- [140] Frenkel D, Smit B. Understanding molecular simulation: from algorithms to applications. 2nd ed. Academic Press; 2002.
- [141] Nose S. A unified formulation of the constant temperature molecular-dynamics methods. *J Chem Phys* 1984;81(1):511–9.
- [142] Hoover WG. Canonical dynamics – equilibrium phase-space distributions. *Phys Rev A* 1985;31(3):1695–7.
- [143] Hohenberg P, Kohn W. Inhomogeneous electron gas. *Phys Rev B* 1964;136(3B):B864.
- [144] Kohn W, Sham LJ. Self-consistent equations including exchange and correlation effects. *Phys Rev* 1965;140(4A):1133.
- [145] Martin RM. Electronic structure: basic theory and practical methods. Cambridge: Cambridge University Press; 2008.
- [146] Kaxiras E. Atomistic and electronic structure of solids. Cambridge: Cambridge University Press; 2003.
- [147] Payne MC et al. Iterative minimization techniques for ab initio total-energy calculations – molecular-dynamics and conjugate gradients. *Rev Mod Phys* 1992;64(4):1045–97.
- [148] Kresse G, Furthmüller J. Efficient iterative schemes for ab initio total-energy calculations using a plane-wave basis set. *Phys Rev B* 1996;54(16):11169–86.
- [149] Kresse G, Joubert D. From ultrasoft pseudopotentials to the projector augmented-wave method. *Phys Rev B* 1999;59(3):1758–75.
- [150] Car R, Parrinello M. Unified approach for molecular-dynamics and density-functional theory. *Phys Rev Lett* 1985;55(22):2471–4.
- [151] Kazimirov VY et al. Local organization and atomic clustering in multicomponent amorphous steels. *Phys Rev B* 2008;78(5):054112.
- [152] Sheng HW et al. Atomic packing and short-to-medium-range order in metallic glasses. *Nature* 2006;439(7075):419–25.
- [153] Egami T. Understanding the properties and structure of metallic glasses at the atomic level. *JOM – J Miner Met Mater Soc* 2010;62(2):70–5.
- [154] Daw MS, Baskes MI. Semiempirical, quantum-mechanical calculation of hydrogen embrittlement in metals. *Phys Rev Lett* 1983;50(17):1285–8.
- [155] Daw MS, Baskes MI. Embedded-atom method – derivation and application to impurities, surfaces, and other defects in metals. *Phys Rev B* 1984;29(12):6443–53.
- [156] Daw MS, Foiles SM, Baskes MI. The embedded-atom method – a review of theory and applications. *Mater Sci Rep* 1993;9(7–8):251–310.
- [157] Foiles SM, Baskes MI, Daw MS. Embedded-atom-method functions for the fcc metals Cu, Ag, Au, Ni, Pd, Pt, and their alloys. *Phys Rev B* 1986;33(12):7983–91.
- [158] Foiles SM. Application of the embedded-atom method to liquid transition-metals. *Phys Rev B* 1985;32(6):3409–15.
- [159] Mishin Y et al. Interatomic potentials for monoatomic metals from experimental data and ab initio calculations. *Phys Rev B* 1999;59(5):3393–407.
- [160] Mishin Y et al. Structural stability and lattice defects in copper: Ab initio, tight-binding, and embedded-atom calculations. *Phys Rev B* 2001;63(22):224106.
- [161] Baskes MI. Modified embedded-atom potentials for cubic materials and impurities. *Phys Rev B* 1992;46(5):2727–42.
- [162] Mishin Y, Lozovoi AY. Angular-dependent interatomic potential for tantalum. *Acta Mater* 2006;54(19):5013–26.
- [163] Cheng YQ, Ma E, Sheng HW. Atomic level structure in multicomponent bulk metallic glass. *Phys Rev Lett* 2009;102(24):245501.
- [164] Bernal JD. Geometry of the structure of monatomic liquids. *Nature* 1960;185(4706):68–70.
- [165] Bernal JD. Bakerian lecture 1962 – structure of liquids. *Proc Roy Soc Lond Ser A – Math Phys Sci* 1964;280(138):299–&.
- [166] Scott GD. Packing of equal spheres. *Nature* 1960;188(4754):908–9.
- [167] Finney JL. Random packings and structure of simple liquids. 1. Geometry of random close packing. *Proc Roy Soc Lond Ser A – Math Phys Sci* 1970;319(1539):479.
- [168] Finney JL. Random packings and structure of simple liquids. 2. Molecular geometry of simple liquids. *Proc Roy Soc Lond Ser A – Math Phys Sci* 1970;319(1539):495.
- [169] Boerdijk AH. Some remarks concerning close-packing of equal spheres. *Philips Res Rep* 1952;7(4):303–13.
- [170] Barnett RN, Cleveland CL, Landman U. Structure and dynamics of a metallic-glass – molecular-dynamics simulations. *Phys Rev Lett* 1985;55(19):2035–8.
- [171] Sadoc JF, Dixmier J, Guinier A. Theoretical calculation of dense random packings of equal and non-equal sized hard spheres applications to amorphous metallic alloys. *J Non-Cryst Solids* 1973;12(1):46–60.
- [172] Nelson DR, Spaepen F. Polytetrahedral order in condensed matter. *Solid State Phys – Adv Res Appl* 1989;42:1–90.
- [173] Nelson DR. Order, frustration, and defects in liquids and glasses. *Phys Rev B* 1983;28(10):5515–35.
- [174] Frank FC. Supercooling of liquids. *Proc Roy Soc Lond Ser A – Math Phys Sci* 1952;215(1120):43–6.
- [175] Coxeter HSM. Introduction to geometry. New York: Wiley; 1969.
- [176] Sadoc JF. Use of regular polytopes for the mathematical-description of the order in amorphous structures. *J Non-Cryst Solids* 1981;44(1):1–16.
- [177] Nelson DR. Liquids and glasses in spaces of incommensurate curvature. *Phys Rev Lett* 1983;50(13):982–5.
- [178] Morse PM. Diatomic molecules according to the wave mechanics. II. Vibrational levels. *Phys Rev* 1929;34(1):57.
- [179] Dzugutov M. Glass-formation in a simple monatomic liquid with icosahedral inherent local order. *Phys Rev A* 1992;46(6):R2984–7.
- [180] Hoare M. Stability and local order in simple amorphous packings. *Ann NY Acad Sci* 1976;279(October 15):186–207.
- [181] Doye JPK, Wales DJ. The structure and stability of atomic liquids: from clusters to bulk. *Science* 1996;271(5248):484–7.
- [182] Doye JPK et al. The favored cluster structures of model glass formers. *J Chem Phys* 2003;118(6):2792–9.
- [183] Turnbull D. Kinetics of solidification of supercooled liquid mercury droplets. *J Chem Phys* 1952;20(3):411–24.

- [184] Reichert H et al. Observation of five-fold local symmetry in liquid lead. *Nature* 2000;408(6814):839–41.
- [185] Holland-Moritz D et al. Electromagnetic levitation apparatus for diffraction investigations on the short-range order of undercooled metallic melts. *Meas Sci Technol* 2005;16(2):372–80.
- [186] Schenk T et al. Icosahedral short-range order in deeply undercooled metallic melts. *Phys Rev Lett* 2002;89(7):075507.
- [187] Holland-Moritz D et al. Short-range order in undercooled Co melts. *J Non-Cryst Solids* 2002;312:47–51.
- [188] Lee GW et al. Difference in icosahedral short-range order in early and late transition metal liquids. *Phys Rev Lett* 2004;93(3):037802.
- [189] Holland-Moritz D et al. Short-range order of stable and undercooled liquid titanium. *Mater Sci Eng A – Struct Mater Prop Microstruct Process* 2007;449:42–5.
- [190] Kim TH, Kelton KF. Structural study of supercooled liquid transition metals. *J Chem Phys* 2007;126(5):054513.
- [191] Di Cicco A et al. Is there icosahedral ordering in liquid and undercooled metals? *Phys Rev Lett* 2003;91(13):135505.
- [192] Jakse N, Pasturel A. Ab initio molecular dynamics simulations of local structure of supercooled Ni. *J Chem Phys* 2004;120(13):6124–7.
- [193] Ganesh P, Widom M. Signature of nearly icosahedral structures in liquid and supercooled liquid copper. *Phys Rev B* 2006;74(13):134205.
- [194] Ganesh P, Widom M. Ab initio simulations of geometrical frustration in supercooled liquid Fe and Fe-based metallic glass. *Phys Rev B* 2008;77(1):014205.
- [195] Jakse N, Pasturel A. Local order of liquid and supercooled zirconium by ab initio molecular dynamics. *Phys Rev Lett* 2003;91(19):195501.
- [196] Jakse N, Le Bacq O, Pasturel A. Prediction of the local structure of liquid and supercooled tantalum. *Phys Rev B* 2004;70(17):174203.
- [197] Lee B, Lee GW. Local structure of liquid Ti: Ab initio molecular dynamics study. *J Chem Phys* 2008;129(2):024711.
- [198] Reuse FA, Khanna SN, Bernal S. Electronic-structure and magnetic-behavior of Ni-13 clusters. *Phys Rev B* 1995;52(16):11650–3.
- [199] Wang SY et al. First-principles study of the stability of the icosahedral Ti-13, Ti-13(-1), and Ti-13(+1) clusters. *Phys Rev B* 2002;65(16):165424.
- [200] Lee BC, Lee GW. Comparative study of Ti and Ni clusters from first principles. *J Chem Phys* 2007;127(16):164316.
- [201] Inoue A, Nishiyama N, Kimura H. Preparation and thermal stability of bulk amorphous  $Pd_{40}Cu_{30}Ni_{10}P_{20}$  alloy cylinder of 72 mm in diameter. *Mater Trans* 1997;38(2):179–83.
- [202] Schroers J, Johnson WL. Ductile bulk metallic glass. *Phys Rev Lett* 2004;93(25):255506.
- [203] Inoue A, Takeuchi A, Shen BL. Formation and functional properties of Fe-based bulk glassy alloys. *Mater Trans* 2001;42(6):970–8.
- [204] Cargill GS. Structural investigation of noncrystalline nickel-phosphorus alloys. *J Appl Phys* 1970;41(1):12.
- [205] Cargill GS. Dense random packing of hard spheres as a structural model for noncrystalline metallic solids. *J Appl Phys* 1970;41(5):2248.
- [206] Polk DE. Structural model for amorphous metallic alloys. *Scripta Metall* 1970;4(2):117.
- [207] Polk DE. Structure of glassy metallic alloys. *Acta Metall* 1972;20(4):485.
- [208] von Heimendahl LV. Metallic glasses as relaxed bernal structures. *J Phys F – Met Phys* 1975;5(9):L141–5.
- [209] Finney JL. Modeling structures of amorphous metals and alloys. *Nature* 1977;266(5600):309–14.
- [210] Vincze I, Boudreux DS, Tegze M. Short-range order in Fe-B metallic glass alloys. *Phys Rev B* 1979;19(10):4896–900.
- [211] Hayes TM et al. Short-range order in metallic glasses. *Phys Rev Lett* 1978;40(19):1282–5.
- [212] Allen JW, Wright AC, Connell GAN. Hybridization, short-range order, and entropy in metallic glass-formation. *J Non-Cryst Solids* 1980;42(1–3):509–24.
- [213] Gaskell PH. New structural model for transition metal–metalloid glasses. *Nature* 1978;276(5687):484–5.
- [214] Gaskell PH. New structural model for amorphous transition-metal silicides, borides, phosphides and carbides. *J Non-Cryst Solids* 1979;32(1–3):207–24.
- [215] Dubois JM, Gaskell PH, Lecaer G. A model for the structure of metallic glasses based on chemical twinning. *Proc Roy Soc Lond Ser A – Math Phys Sci* 1985;402(1823):323–57.
- [216] Waseda Y, Chen HS. Structural study of metallic glasses containing boron (Fe-B, Co-B, and Ni-B). *Phys Status Solidi A – Appl Res* 1978;49(1):387–92.
- [217] Boudreux DS, Frost HJ. Short-range order in theoretical-models of binary metallic-glass alloys. *Phys Rev B* 1981;23(4):1506–16.
- [218] Lamparter P. Reverse Monte-Carlo simulation of amorphous  $Ni_{80}P_{20}$  and  $Ni_{81}B_{19}$ . *Phys Scripta* 1995;T57:72–8.
- [219] Evteev AV, Kosilov AT, Levchenko EV. Atomic mechanisms of formation and structure relaxation of  $Fe_{83}M_{17}$  (M: C, B, P) metallic glass. *Acta Mater* 2003;51(9):2665–74.
- [220] Luo WK, Sheng HW, Ma E. Pair correlation functions and structural building schemes in amorphous alloys. *Appl Phys Lett* 2006;89(13):131927.
- [221] Miracle DB. A structural model for metallic glasses. *Nat Mater* 2004;3(10):697–702.
- [222] Egami T et al. Structure of bulk amorphous Pd–Ni–P alloys determined by synchrotron radiation. *Metall Mater Trans A – Phys Metall Mater Sci* 1998;29(7):1805–9.
- [223] Alamgir FA et al. The structure of a metallic glass system using EXELFS and EXAFS as complementary probes. *Micron* 2003;34(8):433–9.
- [224] Hirata A et al. Local atomic structure of Pd–Ni–P bulk metallic glass examined by high-resolution electron microscopy and electron diffraction. *Intermetallics* 2006;14(8–9):903–7.
- [225] Tang XP et al. Structural influence on atomic hopping and electronic states of Pd-based bulk metallic glasses. *Appl Phys Lett* 2005;86(7):072104.
- [226] Shen TD, Harms U, Schwarz RB. Correlation between the volume change during crystallization and the thermal stability of supercooled liquids. *Appl Phys Lett* 2003;83(22):4512–4.
- [227] Park C et al. Structural study of Pd-based amorphous alloys with wide supercooled liquid region by anomalous X-ray scattering. *Mater Trans* 1999;40(6):491–7.

- [228] Hosokawa S et al. Inhomogeneity and glass-forming ability in the bulk metallic glass Pd<sub>42.5</sub>Ni<sub>7.5</sub>Cu<sub>30</sub>P<sub>20</sub> as seen via X-ray spectroscopies. *Phys Rev B* 2009;80(17):174204.
- [229] FdezGubieda ML et al. Evidence of strong short-range order in (Fe<sub>0.2</sub>Co<sub>0.8</sub>)(75)Si<sub>x</sub>B<sub>25-x</sub> amorphous alloys from EXAFS spectroscopy. *Phys Rev B* 1996;53(2):620–8.
- [230] May JE et al. Amorphous phase partitioning in FeCo-based metallic glass alloys. *J Non-Cryst Solids* 2004;348:250–7.
- [231] Sun BA et al. Aluminum-rich bulk metallic glasses. *Scripta Mater* 2008;59(10):1159–62.
- [232] Yang BJ et al. Al-rich bulk metallic glasses with plasticity and ultrahigh specific strength. *Scripta Mater* 2009;61(4):423–6.
- [233] Yang BJ et al. Developing aluminum-based bulk metallic glasses. *Philos Mag* 2010;90(23):3215–31.
- [234] Luo Q, Wang WH. Rare earth based bulk metallic glasses. *J Non-Cryst Solids* 2009;355(13):759–75.
- [235] Zhang B et al. Amorphous metallic plastic. *Phys Rev Lett* 2005;94(20):205502.
- [236] Hsieh HY et al. Atomic-structure of amorphous Al<sub>90</sub>Fe<sub>x</sub>Ce<sub>10-x</sub>. *J Mater Res* 1990;5(12):2807–12.
- [237] Hsieh HY et al. Short-range ordering in amorphous Al<sub>90</sub>Fe<sub>x</sub>Ce<sub>10-x</sub>. *J Non-Cryst Solids* 1991;135(2–3):248–54.
- [238] Mansour AN, Wong CP, Brizzolara RA. Atomic-structure of amorphous Al<sub>100-2x</sub>Co<sub>x</sub>Ce<sub>x</sub> ( $x = 8, 9$ , and 10) and Al<sub>80</sub>Fe<sub>10</sub>Ce<sub>10</sub> alloys – an XAFS study. *Phys Rev B* 1994;50(17):12401–12.
- [239] Mansour AN et al. Amorphous Al<sub>90</sub>Fe<sub>x</sub>Ce<sub>10-x</sub> alloys: X-ray absorption analysis of the Al, Fe and Ce local atomic and electronic structures. *Phys Rev B* 2002;65(13):134207.
- [240] Egami T. The atomic structure of aluminum-based metallic glasses and universal criterion for glass formation. *J Non-Cryst Solids* 1996;207:575–82.
- [241] Saksl K et al. Atomic structure of Al<sub>88</sub>Y<sub>7</sub>Fe<sub>5</sub> metallic glass. *J Appl Phys* 2005;97(11):113507.
- [242] Saksl K et al. Atomic structure of Al<sub>89</sub>La<sub>6</sub>Ni<sub>5</sub> metallic glass. *J Phys – Condens Matter* 2006;18(32):7579–92.
- [243] Bacewicz R, Antonowicz J. XAFS study of amorphous Al-RE alloys. *Scripta Mater* 2006;54(6):1187–91.
- [244] Zalewski W et al. Local atomic order in Al-based metallic glasses studied using XAFS method. *J Alloy Compd* 2009;468(1–2):40–6.
- [245] Jakse N, Lebacqz O, Pasturel A. Ab initio molecular-dynamics simulations of short-range order in liquid Al<sub>80</sub>Mn<sub>20</sub> and Al<sub>80</sub>Ni<sub>20</sub> alloys. *Phys Rev Lett* 2004;93(20):207801.
- [246] Almarza NG, Lomba E. of the interaction potential from the pair distribution function: an inverse Monte Carlo technique. *Phys Rev E* 2003;68(1):011202.
- [247] Dong C et al. Cluster-based composition rule for stable ternary quasicrystals in Al-(Cu, Pd, Ni)-TM systems. *Philos Mag* 2006;86(3–5):263–74.
- [248] Dong C et al. From clusters to phase diagrams: composition rules of quasicrystals and bulk metallic glasses. *J Phys D – Appl Phys* 2007;40(15):R273–91.
- [249] Ahn K et al. Topological and chemical ordering induced by Ni and Nd in Al<sub>87</sub>Ni<sub>7</sub>Nd<sub>6</sub> metallic glass. *Phys Rev B* 2004;70(22):224103.
- [250] Wang SY et al. Short- and medium-range order in a Zr<sub>73</sub>Pt<sub>27</sub> glass: experimental and simulation studies. *Phys Rev B* 2008;78(18):184204.
- [251] Yang L et al. Origin of the pre-peak in Zr<sub>70</sub>Cu<sub>29</sub>Pd<sub>1</sub> metallic glass. *J Phys – Condens Matter* 2007;19(47):476217.
- [252] Zhang L et al. Origin of the prepeak in the structure factors of liquid and amorphous Al-Fe-Ce alloys. *J Phys – Condens Matter* 1999;11(41):7959–69.
- [253] Kelton KF. Private communications.
- [254] Sheng HW et al. Polyamorphism in a metallic glass. *Nat Mater* 2007;6(3):192–7.
- [255] Zeng QS et al. Anomalous compression behavior in lanthanum/cerium-based metallic glass under high pressure. *Proc Natl Acad Sci USA* 2007;104(34):13565–8.
- [256] Zeng QS et al. Origin of pressure-induced polyamorphism in Ce<sub>75</sub>Al<sub>25</sub> metallic glass. *Phys Rev Lett* 2010;104(10):105702.
- [257] Sheng HW et al. Pressure tunes atomic packing in metallic glass. *Appl Phys Lett* 2006;88(17):171906.
- [258] Wang D et al. Bulk metallic glass formation in the binary Cu-Zr system. *Appl Phys Lett* 2004;84(20):4029–31.
- [259] Xu DH et al. Bulk metallic glass formation in binary Cu-rich alloy series – Cu<sub>100-x</sub>Zrx ( $x = 34, 36, 38.2, 40$  at.%) and mechanical properties of bulk Cu<sub>64</sub>Zr<sub>36</sub> glass. *Acta Mater* 2004;52(9):2621–4.
- [260] Tang MB et al. Binary Cu-Zr bulk metallic glasses. *Chinese Phys Lett* 2004;21(5):901–3.
- [261] Davis LA et al. Strengths and stiffnesses of metallic glasses. *Scripta Metall* 1976;10(10):937–40.
- [262] Altounian Z, Tu GH, Strom-Olsen JO. Crystallization characteristics of Cu-Zr metallic glasses from Cu<sub>70</sub>Zr<sub>30</sub> to Cu<sub>25</sub>Zr<sub>75</sub>. *J Appl Phys* 1982;53(7):4755–60.
- [263] Altounian Z, Strom-Olsen JO. Superconductivity and spin fluctuations in Cu-Zr, Ni-Zr, Co-Zr and Fe-Zr metallic glasses. *Phys Rev B* 1983;27(7):4149–56.
- [264] Calvayrac Y et al. On the stability and structure of Cu-Zr based glasses. *Philos Mag B – Phys Condens Matter Stat Mech Electron Opt Magn Prop* 1983;48(4):323–32.
- [265] Mattern N et al. Structural behavior of Cu<sub>x</sub>Zr<sub>100-x</sub> metallic glass ( $x = 35–70$ ). *J Non-Cryst Solids* 2008;354(10–11):1054–60.
- [266] Ma D, Stoica AD, Wang XL. Power-law scaling and fractal nature of medium-range order in metallic glasses. *Nat Mater* 2009;8(1):30–4.
- [267] Li Y et al. Matching glass-forming ability with the density of the amorphous phase. *Science* 2008;322(5909):1816–9.
- [268] Ma D et al. Efficient local atomic packing in metallic glasses and its correlation with glass-forming ability. *Phys Rev B* 2009;80(1):014202.
- [269] Cheng YQ, Sheng HW, Ma E. Relationship between structure, dynamics, and mechanical properties in metallic glass-forming alloys. *Phys Rev B* 2008;78(1):014207.
- [270] Cheng YQ et al. Local order influences initiation of plastic flow in metallic glass: effects of alloy composition and sample cooling history. *Acta Mater* 2008;56(18):5263–75.
- [271] Lagogianni AE et al. Structural characteristics of Cu<sub>x</sub>Zr<sub>100-x</sub> metallic glasses by Molecular Dynamics Simulations. *J Alloy Compd* 2009;483(1–2):658–61.
- [272] Almyras GA et al. On the microstructure of the Cu<sub>65</sub>Zr<sub>35</sub> and Cu<sub>35</sub>Zr<sub>65</sub> metallic glasses. *Scripta Mater* 2010;62(1):33–6.

- [273] Lee JC et al. Origin of the plasticity in bulk amorphous alloys. *J Mater Res* 2007;22(11):3087–97.
- [274] Wakeda M et al. Relationship between local geometrical factors and mechanical properties for Cu–Zr amorphous alloys. *Intermetallics* 2007;15(2):139–44.
- [275] Yang L et al. Design of Cu<sub>8</sub>Zr<sub>5</sub>-based bulk metallic glasses. *Appl Phys Lett* 2006;88(24).
- [276] Yang L et al. Atomic structure in Zr<sub>70</sub>Ni<sub>30</sub> metallic glass. *J Appl Phys* 2007;102(8):083512.
- [277] Holland-Moritz D et al. Structure and dynamics of liquid Ni<sub>36</sub>Zr<sub>64</sub> studied by neutron scattering. *Phys Rev B* 2009;79(6):064204.
- [278] Iparragirre EW, Sietsma J, Thijssen BJ. A reverse Monte-Carlo study of amorphous Ti<sub>67</sub>Ni<sub>33</sub>. *J Non-Cryst Solids* 1993;156:969–72.
- [279] Ruppertsberg H, Lee D, Wagner CNJ. Observation of chemical short-range order in an amorphous Ni<sub>40</sub>Ti<sub>60</sub> alloy. *J Phys F – Met Phys* 1980;10(8):1645–52.
- [280] Puszta L, Svab E. Structure study of Ni<sub>62</sub>Nb<sub>38</sub> metallic-glass using reverse Monte-Carlo simulation. *J Non-Cryst Solids* 1993;156:973–7.
- [281] Svab E et al. Partial correlations in Ni<sub>60</sub>Nb<sub>40</sub> metallic-glass. *J Non-Cryst Solids* 1981;46(2):125–34.
- [282] Sakata M, Cowlam N, Davies HA. Chemical short-range order in liquid and amorphous Cu<sub>66</sub>Ti<sub>34</sub> alloys. *J Phys F – Met Phys* 1981;11(7):L157–62.
- [283] Zhang L et al. Bulk metallic glasses with large plasticity: composition design from the structural perspective. *Acta Mater* 2009;57(4):1154–64.
- [284] Takagi T et al. Local structure of amorphous Zr<sub>70</sub>Pd<sub>30</sub> alloy studied by electron diffraction. *Appl Phys Lett* 2001;79(4):485–7.
- [285] Sordelet DJ et al. Structure of Zr<sub>x</sub>Pt<sub>100-x</sub> (73 <=x<=77) metallic Glasses. *Metall Mater Trans A – Phys Metall Mater Sci* 2008;39A(8):1908–16.
- [286] Manh DN et al. Electronic-structure and chemical short-range order in amorphous CuZr and NiZr alloys. *J Phys F – Met Phys* 1987;17(6):1309–21.
- [287] Fukunaga T et al. Voronoi analysis of the structure of Cu–Zr and Ni–Zr metallic glasses. *Intermetallics* 2006;14(8–9):893–7.
- [288] Georgarakis K et al. Atomic structure of Zr–Cu glassy alloys and detection of deviations from ideal solution behavior with Al addition by X-ray diffraction using synchrotron light in transmission. *Appl Phys Lett* 2009;94(19):191912.
- [289] Lekka CE, Evangelakis GA. Bonding characteristics and strengthening of CuZr fundamental clusters upon small Al additions from density functional theory calculations. *Scripta Mater* 2009;61(10):974–7.
- [290] Fujita T et al. Atomic-scale heterogeneity of a multicomponent bulk metallic glass with excellent glass forming ability. *Phys Rev Lett* 2009;103(7):075502.
- [291] Kang KH et al. Atomistic modeling of the Cu–Zr–Ag bulk metallic glass system. *Scripta Mater* 2009;61(8):801–4.
- [292] Peker A, Johnson WL. A highly processable metallic-glass – Zr<sub>41.2</sub>Ti<sub>13.8</sub>Cu<sub>12.5</sub>Ni<sub>10.0</sub>Be<sub>22.5</sub>. *Appl Phys Lett* 1993;63(17):2342–4.
- [293] Ma D et al. Nearest-neighbor coordination and chemical ordering in multicomponent bulk metallic glasses. *Appl Phys Lett* 2007;90(21):211908.
- [294] Hufnagel TC, Brennan S. Short- and medium-range order in (Zr<sub>70</sub>Cu<sub>20</sub>Ni<sub>10</sub>)(90-x)TaxAl<sub>10</sub> bulk amorphous alloys. *Phys Rev B* 2003;67(1):014203.
- [295] de Boer FR et al. Cohesion in metals: transition metal alloys. North-Holland: Amsterdam; 1988.
- [296] Zberg B, Uggowitzer PJ, Löffler JE. MgZnCa glasses without clinically observable hydrogen evolution for biodegradable implants. *Nat Mater* 2009;8(11):887–91.
- [297] Bailey NP, Schiotz J, Jacobsen KW. Simulation of Cu–Mg metallic glass: thermodynamics and structure. *Phys Rev B* 2004;69(14):144205.
- [298] Jovari P et al. Atomic structure of glassy Mg<sub>60</sub>Cu<sub>30</sub>Y<sub>10</sub> investigated with EXAFS, X-ray and neutron diffraction, and reverse Monte Carlo simulations. *Phys Rev B* 2007;76(5):054208.
- [299] Hui X et al. Short-to-medium-range order in Mg<sub>65</sub>Cu<sub>25</sub>Y<sub>10</sub> metallic glass. *Phys Lett A* 2008;372(17):3078–84.
- [300] Qi DW, Wang S. Icosahedral order and defects in metallic liquids and glasses. *Phys Rev B* 1991;44(2):884–7.
- [301] Senkov ON et al. Local atomic structure of Ca–Mg–Zn metallic glasses. *Phys Rev B* 2010;82(10):104206.
- [302] Steinhardt PJ. Solid-state physics – how does your quasicrystal grow? *Nature* 2008;452(7183):43–4.
- [303] Shechtman D et al. Metallic phase with long-range orientational order and no translational symmetry. *Phys Rev Lett* 1984;53(20):1951–3.
- [304] Kelton KF et al. First X-ray scattering studies on electrostatically levitated metallic liquids: demonstrated influence of local icosahedral order on the nucleation barrier. *Phys Rev Lett* 2003;90(19):195504.
- [305] Shen YT et al. Icosahedral order, frustration, and the glass transition: evidence from time-dependent nucleation and supercooled liquid structure studies. *Phys Rev Lett* 2009;102(5):057801.
- [306] Saïda J et al. Precipitation of icosahedral phase from a supercooled liquid region in Zr<sub>65</sub>Cu<sub>7.5</sub>Al<sub>7.5</sub>Ni<sub>10</sub>Ag<sub>10</sub> metallic glass. *Appl Phys Lett* 1999;75(22):3497–9.
- [307] Li CF et al. Precipitation of icosahedral quasicrystalline phase in Hf<sub>65</sub>Al<sub>7.5</sub>Ni<sub>10</sub>Cu<sub>12.5</sub>Pd<sub>5</sub> metallic glass. *Appl Phys Lett* 2000;77(4):528–30.
- [308] Frank FC, Kasper JS. Complex alloy structures regarded as sphere packings. 1. Definitions and basic principles. *Acta Crystallogr* 1958;11(3):184–90.
- [309] Frank FC, Kasper JS. Complex alloy structures regarded as sphere packing. 2. Analysis and classification of representative structures. *Acta Crystallogr* 1959;12(7):483–99.
- [310] Doye JPK. The structure, thermodynamics and dynamics of atomic clusters. University of Cambridge; 1996.
- [311] Borodin VA. Local atomic arrangements in polytetrahedral materials. *Philos Mag A – Phys Condens Matter Struct Defect Mech Prop* 1999;79(8):1887–907.
- [312] Borodin VA. Local atomic arrangements in polytetrahedral materials – II. Coordination polyhedra with 14 and 15 atoms. *Philos Mag A – Phys Condens Matter Struct Defect Mech Prop* 2001;81(10):2427–46.
- [313] Doye JPK, Meyer L. Mapping the magic numbers in binary Lennard-Jones clusters. *Phys Rev Lett* 2005;95(6):063401.

- [314] Srolovitz D, Egami T, Vitek V. Radial-distribution function and structural relaxation in amorphous solids. *Phys Rev B* 1981;24(12):6936–44.
- [315] Waseda Y, Egami T. Effect of low-temperature annealing and deformation on the structure of metallic glasses by X-ray diffraction. *J Mater Sci* 1979;14(5):1249–53.
- [316] Dwowski W et al. Structural changes in bulk metallic glass after annealing below the glass-transition temperature. *Mater Sci Eng A – Struct Mater Prop Microstruct Process* 2007;471(1–2):125–9.
- [317] Kolobov AV et al. Understanding the phase-change mechanism of rewritable optical media. *Nat Mater* 2004;3(10):703–8.
- [318] Liu XJ et al. Metallic liquids and glasses: atomic order and global packing. *Phys Rev Lett* 2010;105(15):155501.
- [319] Aronsson B. The crystal structure of Ni3P(Fe3P-type). *Acta Chem Scand* 1955;9(1):137–40.
- [320] Bergerhoff G, Brown ID. Crystallographic databases. In: Allen FH et al. (Hrsg.) Chester. international union of crystallography; 1987 [Inorganic Crystal Structure Database (ICSD)]. <<http://www.fiz-karlsruhe.de/icsd.html>>.
- [321] Egami T, Waseda Y. Atomic size effect on the formability of metallic glasses. *J Non-Cryst Solids* 1984;64(1–2):113–34.
- [322] Miracle DB. The efficient cluster packing model – an atomic structural model for metallic glasses. *Acta Mater* 2006;54(16):4317–36.
- [323] Senkov ON, Miracle DB. Effect of the atomic size distribution on glass forming ability of amorphous metallic alloys. *Mater Res Bull* 2001;36(12):2183–98.
- [324] Miracle DB, Sanders WS, Senkov ON. The influence of efficient atomic packing on the constitution of metallic glasses. *Philos Mag* 2003;83(20):2409–28.
- [325] Miracle DB, Lord EA, Ranganathan S. Candidate atomic cluster configurations in metallic glass structures. *Mater Trans* 2006;47(7):1737–42.
- [326] Miracle DB, Greer AL, Kelton KF. Icosahedral and dense random cluster packing in metallic glass structures. *J Non-Cryst Solids* 2008;354(34):4049–55.
- [327] Miracle DB et al. Structural aspects of metallic glasses. *MRS Bull* 2007;32(8):629–34.
- [328] Torquato S, Truskett TM, Debenedetti PG. Is random close packing of spheres well defined? *Phys Rev Lett* 2000;84(10):2064–7.
- [329] Sheng HW, Ma E. Atomic packing of the inherent structure of simple liquids. *Phys Rev E* 2004;69(6):062202.
- [330] Anikeenko AV, Medvedev NN. Polytetrahedral nature of the dense disordered packings of hard spheres. *Phys Rev Lett* 2007;98(23):235504.
- [331] Anikeenko AV, Medvedev NN, Aste T. Structural and entropic insights into the nature of the random-close-packing limit. *Phys Rev E* 2008;77(3):031101.
- [332] Kamien RD, Liu AJ. Why is random close packing reproducible? *Phys Rev Lett* 2007;99(15):155501.
- [333] Miracle DB et al. An assessment of binary metallic glasses: correlations between structure, glass forming ability and stability. *Int Mater Rev* 2010;55(4):218–56.
- [334] Lu BC et al. A model of atom dense packing for metallic glasses with high-solute concentration. *Appl Phys Lett* 2009;94(24):241913.
- [335] Xia JH et al. Ternary bulk metallic glasses formed by minor alloying of Cu<sub>8</sub>Zr<sub>5</sub> icosahedron. *Appl Phys Lett* 2006;88(10).
- [336] Mattern N et al. Structural behavior of Pd<sub>40</sub>Cu<sub>30</sub>Ni<sub>10</sub>P<sub>20</sub> bulk metallic glass below and above the glass transition. *Appl Phys Lett* 2003;82(16):2589–91.
- [337] Mancini L et al. Hierarchical porosity in real quasicrystals. *Philos Mag Lett* 1998;78(2):159–67.
- [338] Coddens G. Comment on ‘Hierarchical porosity in real quasicrystals’. *Philos Mag Lett* 1999;79(12):925–7.
- [339] Mancini L et al. Reply to the comment by G. Coddens on ‘Hierarchical porosity in real quasicrystals’. *Philos Mag Lett* 1999;79(12):929–30.
- [340] Shi YF, Falk ML. Strain localization and percolation of stable structure in amorphous solids. *Phys Rev Lett* 2005;95(9):095502.
- [341] Stillinger FH. A topographic view of supercooled liquids and glass-formation. *Science* 1995;267(5206):1935–9.
- [342] Zhao ZF et al. Measurements of slow beta-relaxations in metallic glasses and supercooled liquids. *Phys Rev B* 2007;75(17):174201.
- [343] Hachenberg J et al. Merging of the alpha and beta relaxations and aging via the Johari–Goldstein modes in rapidly quenched metallic glasses. *Appl Phys Lett* 2008;92(13):131911.
- [344] Casalini R, Roland CM. Aging of the secondary relaxation to probe structural relaxation in the glassy state. *Phys Rev Lett* 2009;102(3):035701.
- [345] Sastry S, Debenedetti PG, Stillinger FH. Signatures of distinct dynamical regimes in the energy landscape of a glass-forming liquid. *Nature* 1998;393(6685):554–7.
- [346] Sastry S et al. Potential energy landscape signatures of slow dynamics in glass forming liquids. *Phys A – Stat Mech Appl* 1999;270(1–2):301–8.
- [347] Kob W et al. Dynamical heterogeneities in a supercooled Lennard-Jones liquid. *Phys Rev Lett* 1997;79(15):2827–30.
- [348] Donati C et al. Spatial correlations of mobility and immobility in a glass-forming Lennard-Jones liquid. *Phys Rev E* 1999;60(3):3107–19.
- [349] Sillescu H. Heterogeneity at the glass transition: a review. *J Non-Cryst Solids* 1999;243(2–3):81–108.
- [350] Glotzer SC. Spatially heterogeneous dynamics in liquids: insights from simulation. *J Non-Cryst Solids* 2000;274(1–3):342–55.
- [351] Widmer-Cooper A, Harrowell P, Fynnewever H. How reproducible are dynamic heterogeneities in a supercooled liquid? *Phys Rev Lett* 2004;93(13):135701.
- [352] Widmer-Cooper A, Harrowell P. On the relationship between structure and dynamics in a supercooled liquid. *J Phys – Condens Matter* 2005;17(49):S4025–34.
- [353] Matharao GS, Razul MSG, Poole PH. Structural and dynamical heterogeneity in a glass-forming liquid. *Phys Rev E* 2006;74(5):050502.
- [354] La Nave E, Sastry S, Sciotino F. Relation between local diffusivity and local inherent structures in the Kob-Andersen Lennard-Jones model. *Phys Rev E* 2006;74(5):050501.
- [355] Dzugutov M. Anomalous slowing down in the metastable liquid of hard spheres. *Phys Rev E* 2002;65(3):032501.

- [356] Zetterling FHM, Dzugutov M, Simdyankin SI. Formation of large-scale icosahedral clusters in a simple liquid approaching the glass transition. *J Non-Cryst Solids* 2001;293:39–44.
- [357] Dzugutov M, Simdyankin SI, Zetterling FHM. Decoupling of diffusion from structural relaxation and spatial heterogeneity in a supercooled simple liquid. *Phys Rev Lett* 2002;89(19):195701.
- [358] Li MZ et al. Molecular dynamics investigation of dynamical heterogeneity and local structure in the supercooled liquid and glass states of Al. *Phys Rev B* 2008;77(18):184202.
- [359] Jain TS, de Pablo JJ. Role of local structure on motions in the potential energy landscape for a model supercooled polymer. *J Chem Phys* 2005;122(17):147515.
- [360] Cheng YQ, Ma E. Indicators of internal structural states for metallic glasses: local order, free volume, and configurational potential energy. *Appl Phys Lett* 2008;93(5):051910.
- [361] Cheng YQ, Cao AJ, Ma E. Correlation between the elastic modulus and the intrinsic plastic behavior of metallic glasses: the roles of atomic configuration and alloy composition. *Acta Mater* 2009;57(11):3253–67.
- [362] Jakse N, Pasturel A. Local order and dynamic properties of liquid and undercooled Cu<sub>x</sub>Zr<sub>1-x</sub> alloys by ab initio molecular dynamics. *Phys Rev B* 2008;78(21):214204.
- [363] Mendelev MI et al. Molecular dynamics simulation of diffusion in supercooled Cu-Zr alloys. *Philos Mag* 2009;89(2):109–26.
- [364] Peng HL et al. Effect of local structures and atomic packing on glass forming ability in Cu<sub>x</sub>Zr<sub>100-x</sub> metallic glasses. *Appl Phys Lett* 2010;96(2):021901.
- [365] Hao SG et al. Microscopic origin of slow dynamics at the good glass forming composition range in Zr<sub>1-x</sub>Cu<sub>x</sub> metallic liquids. *J Appl Phys* 2010;107(5):053511.
- [366] Cheng YQ, Ma E, Sheng HW. Alloying strongly influences the structure, dynamics, and glass forming ability of metallic supercooled liquids. *Appl Phys Lett* 2008;93(11):111913.
- [367] Keys AS, Glotzer SC. How do quasicrystals grow? *Phys Rev Lett* 2007;99(23):235503.
- [368] Lee CW et al. Link between liquid structure and the nucleation barrier for icosahedral quasicrystal, polytetrahedral, and simple crystalline phases in Ti-Zr-Ni alloys: Verification of Frank's hypothesis. *Phys Rev B* 2005;72(17):174107.
- [369] Kelton KF et al. The influence of order on the nucleation barrier. *MRS Bull* 2004;29(12):940–4.
- [370] Schulli TU et al. Substrate-enhanced supercooling in AuSi eutectic droplets. *Nature* 2010;464(7292):1174–7.
- [371] Pedersen UR et al. Geometry of slow structural fluctuations in a supercooled binary alloy. *Phys Rev Lett* 2010;104(10):105701.
- [372] Royall CP et al. Direct observation of a local structural mechanism for dynamic arrest. *Nat Mater* 2008;7(7):556–61.
- [373] Tanaka H et al. Critical-like behaviour of glass-forming liquids. *Nat Mater* 2010;9(4):324–31.
- [374] Fujita T et al. Coupling between chemical and dynamic heterogeneities in a multicomponent bulk metallic glass. *Phys Rev B* 2010;81(14):140204.
- [375] Kansal AR, Torquato S, Stillinger FH. Computer generation of dense polydisperse sphere packings. *J Chem Phys* 2002;117(18):8212–8.
- [376] Miracle DB, Harrowell P. Noncrystalline compact packings of hard spheres of two sizes: bipyramids and the geometry of common neighbors. *J Chem Phys* 2009;130(11):114505.
- [377] Polk DE, Calka A, Giessen BC. Preparation and thermal and mechanical-properties of new titanium rich metallic glasses. *Acta Metall* 1978;26(7):1097–103.
- [378] Lu ZP, Liu CT. Roles of minor alloying additions in formation of bulk metallic glasses: a review. *J Mater Sci* 2004;39(12):3965–74.
- [379] Wang WH. Roles of minor additions in formation and properties of bulk metallic glasses. *Prog Mater Sci* 2007;52(4):540–96.
- [380] Ichitsubo T et al. Nanoscale elastic inhomogeneity of a Pd-based metallic glass: sound velocity from ultrasonic and inelastic X-ray scattering experiments. *Phys Rev B* 2007;76(14):140201.
- [381] Demetrios MD, Johnson WL, Samwer K. Coarse-grained description of localized inelastic deformation in amorphous metals. *Appl Phys Lett* 2009;94(19):191905.
- [382] Bulatov VV, Argon AS. A stochastic-model for continuum elastoplastic behavior. 1. Numerical approach and strain localization. *Model Simul Mater Sci Eng* 1994;2(2):167–84.
- [383] Deng D, Argon AS, Yip S. Simulation of plastic-deformation in a 2-dimensional atomic glass by molecular-dynamics. 4. *Philos Trans Roy Soc Lond Ser A – Math Phys Eng Sci* 1989;329(1608):613–40.
- [384] Rodney D, Schuh C. Distribution of thermally activated plastic events in a flowing glass. *Phys Rev Lett* 2009;102(23):235503.
- [385] Albano F et al. Relating metallic glass mechanical properties to liquid structure. *Mater Sci Eng A – Struct Mater Prop Microstruct Process* 2004;375:671–4.
- [386] Albano F, Falk ML. Shear softening and structure in a simulated three-dimensional binary glass. *J Chem Phys* 2005;122(15):154508.
- [387] Shi YF, Falk ML. Structural transformation and localization during simulated nanoindentation of a noncrystalline metal film. *Appl Phys Lett* 2005;86(1):011914.
- [388] Shi YF, Falk ML. Atomic-scale simulations of strain localization in three-dimensional model amorphous solids. *Phys Rev B* 2006;73(21):214201.
- [389] Shi Y, Falk ML. Does metallic glass have a backbone? The role of percolating short range order in strength and failure. *Scripta Mater* 2006;54(3):381–6.
- [390] Shi YF, Falk ML. Stress-induced structural transformation and shear banding during simulated nanoindentation of a metallic glass. *Acta Mater* 2007;55(13):4317–24.
- [391] Lekka CE et al. Tensile deformation accommodation in microscopic metallic glasses via subnanocluster reconstructions. *Appl Phys Lett* 2007;91(21):214103.
- [392] Wakeda M, Shibusaki Y. Icosahedral clustering with medium-range order and local elastic properties of amorphous metals. *Acta Mater* 2010;58(11):3963–9.
- [393] Thorpe MF. Continuous deformations in random networks. *J Non-Cryst Solids* 1983;57(3):355–70.

- [394] Harmon JS et al. Anelastic to plastic transition in metallic glass-forming liquids. *Phys Rev Lett* 2007;99(13):135502.
- [395] Conrad JC et al. Contribution of slow clusters to the bulk elasticity near the colloidal glass transition. *Phys Rev Lett* 2006;97(26):265701.
- [396] Cheng YQ, Ma E. Configurational dependence of elastic modulus of metallic glass. *Phys Rev B* 2009;80(6):064104.
- [397] Vasiliev AN et al. Relationship between low-temperature boson heat capacity peak and high-temperature shear modulus relaxation in a metallic glass. *Phys Rev B* 2009;80(17):172102.
- [398] Shintani H, Tanaka H. Universal link between the boson peak and transverse phonons in glass. *Nat Mater* 2008;7(11):870–7.
- [399] Wright WJ, Schwarz RB, Nix WD. Localized heating during serrated plastic flow in bulk metallic glasses. *Mater Sci Eng A – Struct Mater Prop Microstruct Process* 2001;319:229–32.
- [400] Song SX et al. Flow serration in a Zr-based bulk metallic glass in compression at low strain rates. *Intermetallics* 2008;16(6):813–8.
- [401] Cheng YQ et al. Cold versus hot shear banding in bulk metallic glass. *Phys Rev B* 2009;80(13):134115.
- [402] Li QK, Li M. Effects of surface imperfections on deformation and failure of amorphous metals. *Appl Phys Lett* 2005;87(3):031910.
- [403] Cao AJ, Cheng YQ, Ma E. Structural processes that initiate shear localization in metallic glass. *Acta Mater* 2009;57(17):5146–55.
- [404] Li QK, Li M. Assessing the critical sizes for shear band formation in metallic glasses from molecular dynamics simulation. *Appl Phys Lett* 2007;91(23):231905.
- [405] Shi YF. Size-independent shear band formation in amorphous nanowires made from simulated casting. *Appl Phys Lett* 2010;96(12):121909.
- [406] Zink M et al. Plastic deformation of metallic glasses: size of shear transformation zones from molecular dynamics simulations. *Phys Rev B* 2006;73(17):172203.
- [407] Mayr SG. Activation energy of shear transformation zones: a key for understanding rheology of glasses and liquids. *Phys Rev Lett* 2006;97(19):195501.
- [408] Delogu F. Identification and characterization of potential shear transformation zones in metallic glasses. *Phys Rev Lett* 2008;100(25):255901.
- [409] Delogu F. Atomic mobility and strain localization in amorphous metals. *Phys Rev Lett* 2008;100(7):075901.
- [410] Delogu F. Molecular dynamics of shear transformation zones in metallic glasses. *Intermetallics* 2008;16(5):658–61.
- [411] Demkowicz MJ, Argon AS. Liquidlike atomic environments act as plasticity carriers in amorphous silicon. *Phys Rev B* 2005;72(24):245205.
- [412] Demkowicz MJ, Argon AS. High-density liquidlike component facilitates plastic flow in a model amorphous silicon system. *Phys Rev Lett* 2004;93(2):025505.
- [413] Argon AS, Demkowicz MJ. What can plasticity of amorphous silicon tell us about plasticity of metallic glasses? *Metall Mater Trans A – Phys Metall Mater Sci* 2008;39A(8):1762–78.
- [414] Cheng YQ, Ma E. Intrinsic shear strength of metallic glass. *Acta Mater* 2011;59(4):1800–7.
- [415] Park KW et al. Shear localization and the plasticity of bulk amorphous alloys. *Scripta Mater* 2010;63(2):231–4.
- [416] Lind ML, Duan G, Johnson WL. Isoconfigurational elastic constants and liquid fragility of a bulk metallic glass forming alloy. *Phys Rev Lett* 2006;97(1):015501.
- [417] Harmon JS et al. Deformation of glass forming metallic liquids: configurational changes and their relation to elastic softening. *Appl Phys Lett* 2007;90(13):131912.
- [418] Duan G et al. Strong configurational dependence of elastic properties for a binary model metallic glass. *Appl Phys Lett* 2006;89(15):151901.
- [419] Lee M et al. Networked interpenetrating connections of icosahedra: effects on shear transformations in metallic glass. *Acta Mater* 2010;59(1):159–70.
- [420] Egami T. Structural relaxation in metallic glasses. *Ann NY Acad Sci* 1981;371(October):238–51.
- [421] Egami T. Structural relaxation in amorphous alloys – compositional short-range ordering. *Mater Res Bull* 1978;13(6):557–62.
- [422] Egami T. Structural relaxation in amorphous Fe<sub>40</sub>Ni<sub>40</sub>P<sub>14</sub>B<sub>6</sub> studied by energy dispersive-X-ray diffraction. *J Mater Sci* 1978;13(12):2587–99.
- [423] Kohda M et al. Kinetics of volume and enthalpy relaxation in Pt<sub>60</sub>Ni<sub>15</sub>P<sub>25</sub> bulk metallic glass. *Phys Rev B* 2010;81(9):092203.
- [424] Kahl A et al. Dynamical and quasistatic structural relaxation paths in Pd<sub>40</sub>Ni<sub>40</sub>P<sub>20</sub> glass. *Appl Phys Lett* 2009;95(20):201903.
- [425] Ramamurty U et al. Embrittlement of a bulk metallic glass due to low-temperature annealing. *Scripta Mater* 2002;47(2):107–11.
- [426] Murah P, Ramamurty U. Embrittlement of a bulk metallic glass due to sub-T<sub>g</sub> annealing. *Acta Mater* 2005;53(5):1467–78.
- [427] Kumar G et al. Embrittlement of Zr-based bulk metallic glasses. *Acta Mater* 2009;57(12):3572–83.
- [428] Park KW et al. Elastostatically induced structural disordering in amorphous alloys. *Acta Mater* 2008;56(19):5440–50.
- [429] Park KW et al. Homogeneous deformation of bulk amorphous alloys during elastostatic compression and its packing density dependence. *Scripta Mater* 2008;59(7):710–3.
- [430] Lee SC et al. Structural disordering process of an amorphous alloy driven by the elastostatic compression at room temperature. *Appl Phys Lett* 2008;92(15):151906.
- [431] Lee CM et al. Structural disordering of amorphous alloys: a molecular dynamics analysis. *Scripta Mater* 2009;61(9):911–4.
- [432] Dmowski W et al. Structural rejuvenation in a bulk metallic glass induced by severe plastic deformation. *Acta Mater* 2010;58(2):429–38.
- [433] Wiederhorn SM. Fracture surface energy of glass. *J Am Ceram Soc* 1969;52(2):99–105.

- [434] Gu XJ et al. Ductility improvement of amorphous steels: roles of shear modulus and electronic structure. *Acta Mater* 2008;56(1):88–94.
- [435] He Q et al. Locating bulk metallic glasses with high fracture toughness: chemical effects and composition optimization. *Acta Mater* 2011;59(1):202–15.
- [436] Cohen MH, Turnbull D. Molecular transport in liquids and glasses. *J Chem Phys* 1959;31(5):1164–9.
- [437] Turnbull D, Cohen MH. Free-volume model of amorphous phase – glass transition. *J Chem Phys* 1961;34(1):120.
- [438] Turnbull D, Cohen MH. On free-volume model of liquid–glass transition. *J Chem Phys* 1970;52(6):3038.
- [439] Demetriou MD, Johnson WL. Modeling the transient flow of undercooled glass-forming liquids. *J Appl Phys* 2004;95(5):2857–65.
- [440] Spaepen F. Homogeneous flow of metallic glasses: a free volume perspective. *Scripta Mater* 2006;54(3):363–7.
- [441] Egami T, Maeda K, Vitek V. Structural defects in amorphous solids – a computer-simulation study. *Philos Mag A – Phys Condens Matter Struct Defect Mech Prop* 1980;41(6):883–901.
- [442] Srolovitz D et al. Local-structure and topology of a model amorphous metal. *J Phys F – Met Phys* 1981;11(11):2209–19.
- [443] Egami T, Srolovitz D. Local structural fluctuations in amorphous and liquid-metals – a simple theory of the glass-transition. *J Phys F – Met Phys* 1982;12(10):2141–63.
- [444] Egami T, Vitek V. Local structural fluctuations and defects in metallic glasses. *J Non-Cryst Solids* 1984;61–62(JAN):499–510.
- [445] Vitek V, Egami T. Atomic level stresses in solids and liquids. *Phys Status Solidi B – Basic Res* 1987;144(1):145–56.
- [446] Egami T. Universal criterion for metallic glass formation. *Mater Sci Eng A – Struct Mater Prop Microstruct Process* 1997;226:261–7.
- [447] Chen HS, Kata H, Inoue A. Obsevations of stress-induced structural disorder and fictive stress in bulk metallic glasses. In: T. Egami et al., editors. Supercooled liquids, glass transition and bulk metallic glasses; 2003. p. 219–30.
- [448] Egami T. Formation and deformation of metallic glasses: atomistic theory. *Intermetallics* 2006;14(8–9):882–7.
- [449] Egami T et al. Glass transition in metallic glasses: a microscopic model of topological fluctuations in the bonding network. *Phys Rev B* 2007;76(2):024203.
- [450] Levashov VA et al. Equipartition theorem and the dynamics of liquids. *Phys Rev B* 2008;78(6):064205.
- [451] Srolovitz D et al. Structural defects in amorphous solids statistical-analysis of a computer-model. *Philos Mag A – Phys Condens Matter Struct Defect Mech Prop* 1981;44(4):847–66.
- [452] Slipenyuk A, Eckert J. Correlation between enthalpy change and free volume reduction during structural relaxation of  $Zr_{55}Cu_{30}Al_{10}Ni_2$  metallic glass. *Scripta Mater* 2004;50(1):39–44.
- [453] Tomida T, Egami T. Molecular-dynamics study of structural anisotropy and anelasticity in metallic glasses. *Phys Rev B* 1993;48(5):3048–57.
- [454] Suzuki Y, Haimovich J, Egami T. Bond-orientational anisotropy in metallic glasses observed by X-ray-diffraction. *Phys Rev B* 1987;35(5):2162–8.
- [455] Egami T et al. Deformation-induced bond-orientational order in metallic glasses. *J Non-Cryst Solids* 1995;193:591–4.
- [456] Dworski W, Egami T. Observation of structural anisotropy in metallic glasses induced by mechanical deformation. *J Mater Res* 2007;22(2):412–8.
- [457] Cugianioldo LF, Kurchan J, Peliti L. Energy flow, partial equilibration, and effective temperatures in systems with slow dynamics. *Phys Rev E* 1997;55(4):3898.
- [458] Berthier L, Barrat J-L. Shearing a glassy material: numerical tests of nonequilibrium mode-coupling approaches and experimental proposals. *Phys Rev Lett* 2002;89(9):095702.
- [459] Manning ML, Langer JS, Carlson JM. Strain localization in a shear transformation zone model for amorphous solids. *Phys Rev E* 2007;76(5):056106.
- [460] Manning ML et al. Rate-dependent shear bands in a shear-transformation-zone model of amorphous solids. *Phys Rev E* 2009;79(1):016110.
- [461] Bouchbinder E, Langer JS. Nonequilibrium thermodynamics of driven amorphous materials. II. Effective-temperature theory. *Phys Rev E* 2009;80(3):031132.
- [462] Cheng YQ, Ma E. Unpublished results.
- [463] Lu ZP et al. The correlation between reduced glass transition temperature and glass forming ability of bulk metallic glasses. *Scripta Mater* 2000;42(7):667–73.
- [464] Lu ZP, Liu CT. A new glass-forming ability criterion for bulk metallic glasses. *Acta Mater* 2002;50(13):3501–12.
- [465] Lu ZP, Liu CT. Glass formation criterion for various glass-forming systems. *Phys Rev Lett* 2003;91(11):115505.
- [466] Lu ZP, Bei H, Liu CT. Recent progress in quantifying glass-forming ability of bulk metallic glasses. *Intermetallics* 2007;15(5–6):618–24.
- [467] Senkov ON. Correlation between fragility and glass-forming ability of metallic alloys. *Phys Rev B* 2007;76(10):104202.
- [468] Tanaka H. Relationship among glass-forming ability, fragility and short-range bond ordering of liquids. *J Non-Cryst Solids* 2005;351(8–9):678–90.
- [469] Yu HB et al. Relating activation of shear transformation zones to beta-relaxations in metallic glasses. *Phys Rev B* 2010;81(22):220201. R.
- [470] Chen HS, Krause JT, Coleman E. Elastic-constants, hardness and their implications to flow properties of metallic glasses. *J Non-Cryst Solids* 1975;18(2):157–71.
- [471] Lewandowski JJ, Shazly M, Nouri AS. Intrinsic and extrinsic toughening of metallic glasses. *Scripta Mater* 2006;54(3):337–41.
- [472] Gu XJ et al. Critical Poisson's ratio for plasticity in Fe–Mo–C–B–Ln bulk amorphous steel. *Appl Phys Lett* 2006;88(21):211905.
- [473] Wang WH. Correlations between elastic moduli and properties in bulk metallic glasses. *J Appl Phys* 2006;99(9):093506.
- [474] Liu Y et al. Physical factors controlling the ductility of bulk metallic glasses. *Appl Phys Lett* 2008;93(15):151915.
- [475] Jiang MQ et al. Energy dissipation in fracture of bulk metallic glasses via inherent competition between local softening and quasi-cleavage. *Philos Mag* 2008;88(3):407–26.